



SCUOLA DOTTORALE IN INGEGNERIA
Dottorato di ricerca in Scienze dell'Ingegneria Civile

SCUOLA DOTTORALE / DOTTORATO DI RICERCA IN

XXVII CICLO

CICLO DEL CORSO DI DOTTORATO

Uniaxial Material Model for Reinforcing Bar Including
Buckling in RC Structures

Titolo della tesi

Zhihao Zhou

Nome e Cognome del dottorando

firma

Prof. Camillo Nuti

Docente Guida/Tutor: Prof.

firma

Prof. Aldo Fiori

Coordinatore: Prof.

firma

Collana delle tesi di Dottorato di Ricerca
In Scienze dell'Ingegneria Civile
Università degli Studi Roma Tre
Tesi n° 55

Abstract

The constitutive model of steel reinforcing bar incorporating inelastic buckling is crucial to accurate seismic performance evaluation of the existing reinforced concrete structures. According to experimental observations, in presence of inelastic buckling the absolute maximum stress of the rebar in compression could reduce to half of the value in absence of buckling.

In this thesis, based on fiber element model, the effect of the yield strength on the critical slenderness of the rebar is studied. Then the formulas, incorporating the effect of yield stress, are given to calculate the computational slenderness critical slenderness. Next the anisotropy of some stainless steel rebar is studied according to a series of monotonic and cyclic tests on bare stainless steel rebars. Two parameters are proposed to consider the effects of anisotropy of rebar.

Considering the above studies, the modified Monti-Nuti Model is proposed to improve the applicability. In order to eliminate overestimation of stress when the model is subjected to generalized loading, the criteria to update the parameters in the model for each half branch at the reversal are discussed and new strategies to update the model parameters in different unloading or reloading cases are proposed.

The Framework adopting Genetic Algorithm is designed to identify the parameters in the modified Monti-Nuti model. By minimizing the stress difference between the numerical curve and experimental curve at each strain step of the cyclic loading histories, the optimized parameters could be identified. Then the empirical formulae are proposed to calculate the values of the parameters in a simpler, more efficient and still robust way.

The modified Monti-Nuti model is implemented into OpenSees as a new material model named as “steel05”. Then validation of this material model with the experimental curves of carbon steel rebars and stainless steel rebars confirms the effectiveness and significance of this new model. Furthermore, the application of the new material in the structural analysis of circular reinforced concrete piers is made and the numerical curves are compared with the experimental curves to verify the effectiveness of the new material.

Finally, the effects of corrosion of the rebar, which is inevitable in aged reinforced concrete structures, are studied based on a series of experiments on the bare corroded reinforcing bars. It is found that the mean yield stresses of the corroded rebar could be different in tension and

in compression. The computational length of the rebar increases resulting from the deterioration of the confinement from the transverse loop. The corrosion extended model is proposed to consider the aforementioned characteristics resulting from corrosion.

Contents

LIST OF FIGURES	IX
LIST OF TABLES	XVI
LIST OF SYMBOLS	XVII
1. INTRODUCTION.....	1
1.1 BACKGROUNDS	1
1.1.1 Importance of Inelastic Buckling.....	2
1.1.2 Rebar Applied in the Concrete Structures	5
1.2 LITERATURE REVIEW	5
1.2.1 Cyclic Steel Model for Rebar.....	6
1.2.2 Steel Model Incorporating Inelastic Buckling	14
1.3 SIGNIFICANCE AND AIMS OF CURRENT RESEARCH	18
1.3.1 Significance	18
1.3.2 Aims of Current Research.....	19
1.4 ORGANIZATION OF THIS THESIS	19
2. ORIGINAL MONTI-NUTI MODEL	20
2.1 MONOTONIC SKELETON CURVE	20
2.2 HARDENING RULES FOR CYCLIC BEHAVIORS OF STEEL REBAR	23
2.2.1 In Absence of Buckling	23
2.2.2 In Presence of Buckling	27
2.3 CURVE TRANSITION PARAMETER R	31
2.3.1 In Absence of Buckling	32
2.3.2 In Presence of Buckling.....	32
2.4 HARDENING RATIO	33
2.4.1 In Absence of Buckling	34
2.4.2 In Presence of Buckling.....	34
2.5 ELASTIC MODULUS E.....	35
2.5.1 In Absence of Buckling	35
2.5.2 In Presence of Buckling.....	35
3. IMPROVEMENT OF THE ORIGINAL MODEL	37
3.1 EFFECT OF YIELD STRESS ON CRITICAL SLENDERNESS	44
3.1.1 Fiber Model Adopted in Microanalysis of Bare Bar	45
3.1.2 Verification of the Fiber Model.....	55
3.1.3 Combined Factor Affecting Critical Slenderness	58
3.2 ANISOTROPY OF STEEL REBAR	60

3.3 MODIFIED MONTI-NUTI MODEL	62
3.3.1 <i>Effect of the Yield Strength</i>	63
3.3.2 <i>Effect of the Anisotropy</i>	63
3.4 ADDITIONAL CRITERIA FOR UPDATE THE MODEL PARAMETERS	65
3.4.1 <i>Discussion of the Proposed Solutions to Address the Above Issues</i>	65
3.4.2 <i>Proposed Criteria to Update the Model Parameters under Generalized Loading</i>	70
4. PARAMETER IDENTIFICATION BY GENETIC ALGORITHM	83
4.1 INTRODUCTION OF PARAMETER IDENTIFICATION BY GENETIC ALGORITHM	83
4.1.1 <i>Parameter Identification</i>	83
4.1.2 <i>Genetic Algorithm</i>	85
4.2 DESIGN OF PARAMETER IDENTIFICATION OF MODIFIED MONTI-NUTI MODEL	85
4.2.1 <i>Parameters to Be Calibrated</i>	86
4.2.2 <i>Flowchart</i>	86
4.2.3 <i>Objective Function</i>	88
4.2.4 <i>Bounds of the Parameters</i>	88
4.3 EFFECTIVENESS OF THE OPTIMIZED PARAMETERS	89
4.3.1 <i>Stress-Strain Curve</i>	89
4.3.2 <i>Step-Stress Comparison</i>	92
4.3.3 <i>Robustness</i>	94
4.4 PROPOSED FORMULAS FOR THE PARAMETERS IN THE MODIFIED MONTI-NUTI MODEL	96
5. IMPLEMENTATION AND VALIDATION OF THE MODIFIED MONTI-NUTI MODEL	97
5.1 IMPLEMENT THE MATERIAL MODEL IN OPENSEES	97
5.2 VALIDATION OF THE MODIFIED MONTI-NUTI MODEL	98
5.2.1 <i>Experiments of Carbon Steel Rebar</i>	101
5.2.2 <i>Experiments of Stain Steel Rebar</i>	109
6. APPLICATION IN REINFORCED CONCRETE COLUMN	114
6.1 APPLICATION OF FIBER MODEL IN CANTILEVER COLUMN ANALYSIS	114
6.2 PSEUDO-DYNAMIC TEST OF REINFORCED CONCRETE BRIDGE PIER	115
6.2.1 <i>Regular Reinforced Concrete Bridge Pier</i>	115
6.3 COMPARISON BETWEEN THE NUMERICAL ANALYSIS AND EXPERIMENTAL RESULTS	118
6.3.1 <i>Main Parameters in the Fiber Model</i>	118
6.3.2 <i>Experimental Test of the Bridge Piers</i>	119
6.3.3 <i>Comparisons Between Numerical Curves and Experimental Curves</i>	122
7. EFFECT OF CORROSION ON MODEL FOR REBAR	124

7.1 MECHANISM OF CORROSION OF REBAR IN REINFORCED CONCRETE	125
7.2 EFFECT OF CORROSION	131
7.2.1 EFFECT OF CORROSION ON YIELD STRESS	132
7.2.2 Effect of Corrosion on Critical Slenderness	137
7.2.3 Effect of Corrosion on Computational Length of Rebar	139
7.3 CORROSION EXTENDED MODEL FOR REBAR	140
7.3.1 Notional Yield Stresses in Tension and Compression	141
7.3.2 Slenderness Ratio of Corroded Rebar	142
8. CONCLUSIONS AND FURTHER WORKS	147
8.1 CONCLUSIONS	147
8.2 FURTHER WORKS	149
ACKNOWLEDGEMENTS	151
REFERENCES	152

List of figures

Figure 1.1 Fiber Element Method	1
Figure 1.2 Bearing capacity of column	2
Figure 1.3 Theoretical model for the reinforced bar in the concrete columns (Gomes & Appleton, 1997).....	3
Figure 1.4 The effect of the inelastic buckling on the stress-strain curve..	4
Figure 1.5 Cyclic model proposed by Aktan et al. (1973)	7
Figure 1.6 Cyclic model for rebar proposed by Ma et al. (1976) based on Ramberg-Osgood model.....	8
Figure 1.7 Cyclic stress-strain curve with envelope proposed by Thompson and Park (1978) based on Ramberg-Osgood model.....	9
Figure 1.8 Cyclic stress-strain curve with envelope proposed by.....	10
Figure 1.9 Cyclic model proposed by Aktan and Ersoy (1980).....	10
Figure 1.10 Menegotto-Pinto Model.....	12
Figure 1.11 Modified Menegotto-Pinto model	13
Figure 1.12 Combination of Gomes and Appleton Model.....	14
Figure 1.13 Monotonic Skeleton curve proposed by Dhakal and Maekawa(2002b).....	16
Figure 1.14 Schematic Diagram of rebar in Concrete Column.....	17
Figure 1.15 Trilinear Model proposed by Zong (2010)	18
Figure 2.1 Monotonic tests of carbon steel rebar (Giorgio Monti & Nuti, 1992).....	20
Figure 2.2 Monotonic skeleton curve of Monti-Nuti model	22
Figure 2.3 Effect of strain hardening in absence of buckling	24
Figure 2.4 Effect of strain hardening in presence of buckling	28
Figure 2.5 Stress shift in compressive curve.....	31
Figure 2.6 Degradation of curve transition	32

Figure 2.7 The effect of b on the curve transition.....	33
Figure 2.8 Degradation of elastic modulus	35
Figure 3.1 Comparison between experimental curve and numerical curve generated by original Monti-Nuti model (S5, $L/D=5$)	38
Figure 3.2 Comparison between experimental curve and numerical curve generated by original Monti-Nuti model (S8, $L/D=8$)	38
Figure 3.3 Comparison between experimental curve and numerical curve generated by original Monti-Nuti model (S11, $L/D=11$)	39
Figure 3.4 Monotonic tests on stainless steel rebar (AISI304 or 1.4301)	40
Figure 3.5 Comparison between experimental curve and numerical curve generated by original Monti-Nuti model (Stainless steel rebar, XA1, $L/D=5$)	41
Figure 3.6 Comparison between experimental curve and numerical curve generated by original Monti-Nuti model (Stainless steel rebar, XA2, $L/D=5$)	41
Figure 3.7 Comparison between experimental curve and numerical curve generated by original Monti-Nuti model (Stainless steel rebar, XA3, $L/D=5$)	42
Figure 3.8 Comparison between experimental curve and numerical curve generated by original Monti-Nuti model (Stainless steel rebar, XC1, $L/D=11$)	43
Figure 3.9 Comparison between experimental curve and numerical curve generated by original Monti-Nuti model (Stainless steel rebar, XC2, $L/D=11$)	43
Figure 3.10 Comparison between experimental curve and numerical curve generated by original Monti-Nuti model (Stainless steel rebar, XC3, $L/D=11$)	44
Figure 3.11 Fiber technique in simulating the bare rebar	45
Figure 3.12 Comparisons between monotonic compressive curves of rebar generated by fiber model with or without initial imperfection.....	47

Figure 3.13 Comparisons between the monotonic curves of rebar with different slenderness (L/D) generated by fiber model with different initial imperfections.....	49
Figure 3.14 Comparisons between monotonic curves of rebar with different slendernesses generated by fiber model using different numbers of elements.....	50
Figure 3.15 Comparisons between monotonic curves of rebar with different slendernesses generated by fiber model using different numbers of Integration Points for each element.....	52
Figure 3.16 Comparisons between monotonic curves of rebar with different slendernesses generated by fiber model adopting different numbers of subdivisions along the circle and the radius for cross section meshing	54
Figure 3.17 Verification of the fiber model with monotonic compressive experimental curves with different slendernesses	55
Figure 3.18 Loading strain histories of cyclic test A1 and C1	56
Figure 3.19 Verification of the fiber model with the experimental cyclic stress-strain curves of rebar with different slendernesses	57
Figure 3.20 Effect of yield stress on the stress-strain curves of rebar with different slenderness and yield stress generated by fiber model ..	59
Figure 3.21 Monotonic stress-strain curves of rebar with different combined parameters generated by fiber model.....	59
Figure 3.22 Testing machine and the specimen: a) Test machine MTS 810; b) specimen in tension; c) specimen in compression	61
Figure 3.23 Update curvature parameter $R(\xi)$ in the case of partial unloading and reloading	66
Figure 3.24 Solution to eliminate the overestimation under partial unloading and reloading (Attolico et al., 2000).....	67
Figure 3.25 Solution to eliminate the overestimation under partial unloading and reloading	69
Figure 3.26 Fiber technique and applied in Finite Element Method (Dhakal & Maekawa, 2002c)	70

Figure 3.27 Different types of positions of reversal.....	72
Figure 3.28 Status of branch n+1: Plastic, UL/RL, AB/PB;	73
Figure 3.29 Status of branch n+1: Elastic, UL, AB/PB;	76
Figure 3.30 Status of branch n+1: Elastic, RL, AB;	77
Figure 3.31 Status of branch n+1: Elastic, RL, PB;	78
Figure 3.32 Status of branch n+1: Small, UL, AB/PB;.....	80
Figure 3.33 Status of branch n+1: Small, RL, AB;.....	81
Figure 3.34 Status of branch n+1: Small, RL, PB;.....	82
Figure 4.1 General flowchart of parameter identification.....	84
Figure 4.2 Parameter identification of modified Monti-Nuti model.....	87
Figure 4.3 Comparison between experimental curve and numerical curve generated by modified Monti-Nuti Model (carbon steel rebar, A1, L/D=5)	90
Figure 4.4 Comparison between experimental curve and numerical curve generated by modified Monti-Nuti Model (carbon steel rebar, C1, L/D=11)	90
Figure 4.5 Comparison between experimental curve and numerical curve generated by modified Monti-Nuti Model (stainless steel rebar, XA1, L/D=5)	91
Figure 4.6 Comparison between experimental curve and numerical curve generated by modified Monti-Nuti Model (stainless steel rebar, XC1, L/D=11)	91
Figure 4.7 Step-Stress comparison between experimental curves and numerical curve with optimized parameters (carbon steel rebar, L/D=5, A1)	92
Figure 4.8 Step-Stress comparison between experimental curves and numerical curve with optimized parameters (carbon steel rebar, L/D=11, C1)	93
Figure 4.9 Step-Stress comparison between experimental curves and numerical curve with optimized parameters (stainless steel rebar, L/D=5, XA1)	93

Figure 4.10 Step-Stress comparison between experimental curves and numerical curve with optimized parameters (stainless steel rebar, L/D=11, XC1)	94
Figure 4.11 Derivations of optimized parameters	96
Figure 5.1 Inheritance Diagram of steel model “Steel05”	98
Figure 5.2 Column setup in OpenSees for material test.....	99
Figure 5.3 Scripts used to test “Steel05” in OpenSees.....	100
Figure 5.4 Loading strain histories of carbon steel reinforcement.....	101
Figure 5.5 Comparison of numerical curves and experimental curves (L/D=5).....	104
Figure 5.6 Comparison of numerical curves and experimental curves (L/D=11).....	106
Figure 5.7 Loading strain histories of carbon steel reinforcement.....	107
Figure 5.8 Comparison of numerical curves and experimental curves (S5, L/D=5)	107
Figure 5.9 Comparison of numerical curves and experimental curves (S8, L/D=8)	108
Figure 5.10 Comparison of numerical curves and experimental curves (S11, L/D=11)	108
Figure 5.11 Loading strain histories of stainless steel reinforcement	110
Figure 5.12 Comparison of numerical curves and experimental curves (L/D=5).....	111
Figure 5.13 Comparison of numerical curves and experimental curves (L/D=11).....	113
Figure 6.1 Fiber element technique used in reinforced concrete pier analysis under cyclic loading.....	114
Figure 6.2 Regular bridge	116
Figure 6.3 Pier Specimen corresponding to the middle pier in the regular bridge.....	116
Figure 6.4 Damage of the specimen at the end of the cyclic tests	117

Figure 6.5 Lateral loading displacement histories at the top of the pier	120
Figure 6.6 Experimental lateral force and displacement curve of pier 1	121
Figure 6.7 Experimental lateral force and displacement curve of pier 5	121
Figure 6.8 Comparison of force-displacement curve (horizontal force at the bottom and lateral displacement at the top of pier) between the fiber model and the experimental curves.....	122
Figure 6.9 Comparison of force-displacement curve (horizontal force at the bottom and lateral displacement at the top of pier) between the fiber model and the experimental curve	123
Figure 7.1 Corrosion of rebar in the highway bridge: a) corrosion of the pier b)corrosion of the rebar and spalling of the cover concrete of the wall c) overview of the highway bridge (Tullmin, 2010).....	125
Figure 7.2 corrosion of rebar in concrete (Tullmin, 2010).....	127
Figure 7.3 Stage 1 of corrosion (Tullmin, 2010).....	128
Figure 7.4 Stage 2 of corrosion (Tullmin, 2010).....	128
Figure 7.5 Stage 3 of corrosion (Tullmin, 2010).....	129
Figure 7.6 Stage 4 of corrosion (Tullmin, 2010).....	129
Figure 7.7 Electrochemical reaction of rebar in concrete	130
Figure 7.8 Notional yield stress deterioration in tension and compression ($L/D=5$).....	134
Figure 7.9 Notional yield stress deterioration in tension and compression ($5<L/D\leq 10$)	134
Figure 7.10 Notional yield stress deterioration in tension and compression ($L/D>10$).....	135
Figure 7.11 Relationship between mean yield stress and mass loss rate $L/D=5$, data from Kashni et al. (2013a)	136
Figure 7.12 Relationship between mean yield stress and mass loss rate $L/D=10$, data from Kashni et al. (2013a)	136
Figure 7.13 Relationship between mean yield stress and mass loss rate $L/D=15$, data from Kashni et al. (2013a)	137

Figure 7.14 Ratio between the critical slenderness of corroded rebar and critical slenderness of original rebar $\lambda'_{cr}/\lambda_{cr}$	138
Figure 7.15 Buckling of compressed bar between two consecutive stirrups	139
Figure 7.16 Buckling exceeds two consecutive stirrups	140
Figure 7.17 Stress-strain relationship of corroded rebar with different slenderness.....	143
Figure 7.18 Relationship between λ'/λ (ratio computational slenderness of corroded rebar and original rebar) and mass loss rate.....	144

List of tables

Table 3.1 Properties of test rebar (Dhakai & Maekawa, 2002b).....	37
Table 3.2 Content of chemical composition in stainless steel AISI304...	40
Table 3.3 Selection of Parameters for Fiber Model	54
Table 3.4 Geometric and Mechanical properties of bare rebar	55
Table 3.5 Parameters values of “Steel02” adopted in the fiber model.....	56
Table 3.6 Combined parameter for different rebars	58
Table 3.7 Possible conditions of the previous branch	71
Table 3.8 Strategy for model update at reversal	72
Table 4.1 Lists of parameters to be calibrated	86
Table 4.2 Lower bound and Upper bound of the parameters	89
Table 4.3 Parameter Identification for stainless steel rebar (L/D=5).....	95
Table 4.4 Parameter Identification for stainless steel rebar (L/D=11).....	95
Table 5.1 Properties of tested carbon steel rebar	101
Table 5.2 Properties of test rebar (Dhakai and Maekawa 2002).....	106
Table 5.3 Properties of tested stainless steel rebar	109
Table 6.1 Geometries and configuration of the piers	117
Table 6.2 Mechanical properties of the materials tested in the laboratory	118
Table 6.3 Parameters of “Concrete07” in the fiber model	119
Table 6.4 Parameters of “Steel05” in the fiber model.....	119
Table 7.1 Parameters to calculate the notional yield stress deterioration	133
Table 7.2 Values of c to calculate the notional stress	145

List of symbols

Nell'elenco che segue sono riportati i principali simboli che compaiono nei capitoli della tesi.

λ	<i>Computational slenderness</i>
L	<i>Computational length</i>
D	<i>Diameter of the cross section of rebar</i>
E	Elastic modulus
E_0	Initial tangent modulus
σ	Stress
ε	Strain
i	<i>Radius of gyration</i>
$\lambda_r, (L/D)_{cr}$	Critical slenderness between inelastic buckling and elastic buckling
σ_r	Critical stress between inelastic buckling and elastic buckling
λ_p	Critical slenderness between plastic and inelastic buckling
σ_p	Critical stress between plastic and inelastic buckling
σ_i	Initial stress at the beginning of the half cycle
ε_i	Initial strain at the beginning of the half cycle
σ_0, σ_y	Yield stress

$\varepsilon_0, \varepsilon_y$	Yield strain
σ^*	Normalized stress in Menegotto-Pinto model
ε^*	Normalized strain in Menegotto-Pinto model
b	Hardening ratio used in Menegotto-Pinto model, equaling the ratio between the tangent modulus of the asymptote after yielding point and the initial tangent modulus at the original point or reversal point
σ_r^n	Stress corresponding to the reversal point
ε_r^n	Strain corresponding to the reversal point
σ_y^{n+1}	Stress corresponding to the yield point of the n+1 half cycle
ε_y^{n+1}	Strain corresponding to the yield point of the n+1 half cycle
ξ_n	Plastic excursion at the n th semi cycle normalized by the strain ε_y corresponding to the initial yield stress f_y
R	Curve transition parameter defined in Menegotto-Pinto model
R_0	Initial curve transition value defined in Menegotto-Pinto model
A_1, A_2	Parameters to calculate R , defined in Menegotto-Pinto model
σ_{st}	Stress shift due to isotropic strain hardening
ε_{\max}	Absolute maximum value at the reversal of previous half cycles

a_3, a_4	Experimentally determined parameters to calculate stress shift proposed by Filippou et al.
γ_s	Normalized superposition length, representing the distance between the tensile curve and the monotonic compressive curve after the yield point, defined in Monti-Nuti model
γ_s^*	Real superposition length
b_0^+	Initial hardening ratio in tension, defined in Monti-Nuti model
b_0^-	Initial hardening ratio in compression, defined in Monti-Nuti model
b^+	Hardening ratio in tension
b^-	Hardening ratio in compression
ξ_p^i	Plastic strain hardening at the i th half cycle
ξ_{\max}	Maximum plastic strain hardening of previous half cycles
Φ_p^n	Plastic work of n th half cycle
$\Delta\sigma_K^n$	Stress variation due to kinematic strain hardening at n th half cycle
$\Delta\sigma_I^n$	Stress variation due to isotropic strain hardening at n th half cycle
γ_p^n	Additional plastic excursion
$\Delta\sigma_{IM}^n$	Stress variation due to isotropic strain hardening and memory rule, defined in Monti-Nuti model, in absence of buckling
P	Weight coefficient which determines the contribution

	made by the kinematic rule and the isotropic rule
$\Delta\sigma_{KM,b}^n$	Stress variation due to kinematic strain hardening and memory rule in presence of buckling, defined in Monti-Nuti model
σ_{sh}	Stress shift defined in Monti-Nuti model
R_0^b	Initial value of curve transition parameter in presence of buckling, defined in Monti-Nuti model
A_1^b, A_2^b	Parameter to calculate R in presence of buckling, defined in Monti-Nuti model
R_1^b	Lower bound of R in presence of buckling, defined in Monti-Nuti model
σ_∞	The limitation value of the asymptote for softening branch
Σ_γ	The sum of additional plastic excursion of previous half cycles
$L/D\sqrt{f_y}$	Computational slenderness
$L/D\sqrt{F_y/450}$	Computational critical slenderness
α	Parameter anisotropy coefficient
β	Critical slenderness coefficient
f_Y	Yield stress of Feb44, equaling 450 MPa
f_{yt}	Yield strength of rebar in tension
f_{yc}	Yield stress of the rebar in compression
A_1^t, A_2^t	Parameters to calculate R in tensile half branch, defined in

	modified Monti-Nuti model
A_1^c, A_2^c	Parameters to calculate R in compressive half branch, defined in modified Monti-Nuti model
r_t, r_c	Parameters to calculate the initial value of R_0 , defined in modified Monti-Nuti model
Θ_n	The set of controlling parameters in the model for n th half branch
f	Fitness function
f_k	Value of the fitness function for each experimental curve
ΔY	The difference between the numerical curve and the experimental curve
Y	Sum of the square of the experimental stresses at each strain steps
$y_{E,j}, y_{N,j}$	Stress on the experimental curve and numerical curve corresponding to the same strain
w_k	Weight coefficient for each experimental curve
D'	Mean cross section of the corroded rebar
γ_c	Mass loss rate due to corrosion
ψ	Mass loss rate due to corrosion, in percentage
m_0	Original mass of the rebar
m	Mass of corroded rebar
f'_{yt}	Yield stress in tension corresponding to the corroded rebar based on the mean cross section area

a	Regression factor to calculate f'_{yt} , representing the effect of non-uniform pitting corrosion
f'_{yc}	Yield stress in compression corresponding to the corroded rebar based on the mean cross section area
β_c	Regression factor to calculate f'_{yc} , representing the effect of non-uniform pitting corrosion
d_c^t	Notional yield stress deterioration in tension due to corrosion
d_c^c	Notional yield stress deterioration in compression due to corrosion
λ'_{cr}	Critical slenderness of corroded rebar corresponding to mean yield stress f'_{yc}
λ'	Slenderness of the corroded rebar corresponding to mean yield stress f'_{yc}
L'	Computational length of the corroded rebar
β_c^t	Corrosion deterioration factor incorporating the effect of non-uniform pitting corrosion in tension
β_c^c	Corrosion deterioration factor incorporating the effect of non-uniform pitting corrosion in compression
g	Gap distance generated at the contact point between the stirrup and the longitudinal rebar due to corrosion
D_s	Diameter of the uncorroded stirrup
D'_s	Diameter of the corroded stirrup
μ	Coefficient to calculate the computational length increase

due to corrosion

λ''	Slenderness of the corroded rebar based on the cross section of the original uncorroded rebar
λ''_{cr}	Critical slenderness of the corroded rebar based on the cross section of the original uncorroded rebar
c	deterioration coefficient to calculate f_{yc} which is the notional yield stress in compression corresponding to the corroded rebar

1. INTRODUCTION

The material model for rebar including inelastic buckling is crucial for precise seismic performance evaluation of existing reinforced concrete structures. Through literature review, the state of art of steel material model for rebar in reinforced concrete structures is introduced. Subsequently the significance of this research is demonstrated, and finally the organization of this thesis is briefly explained.

1.1 BACKGROUNDS

There are many existing concrete structures designed before the effect of earthquake was fully studied. The stirrup spacing in existing structures exceeds the maximum limit specified in the current seismic code, thus the confinement of the transverse stirrups towards the longitudinal reinforcement is not sufficient, which will result in the lateral deformation of the longitudinal rebar named as buckling after the collapse of the concrete cover under severe seismic loading.

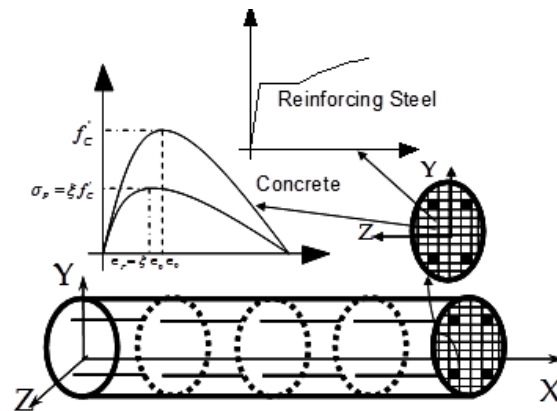


Figure 1.1 Fiber Element Method

In order to evaluate the seismic performance of these reinforced concrete structures, the finite element method adopting fiber element model is

widely applied to reduce the computational cost. As shown in Figure 1.1, the concrete column or beam is divided into segments along the axial length, and the cross section of the segment is further divided into fibers which represent concrete and rebar (Mullapudi, 2010). Supposing that the plane section remains plan, the strain in each fiber is calculated from the centroidal section strain and curvature. Subsequently the stresses and modulus of fibers are calculated from the fiber strain. The constitutive relation of the section is derived by integration of the response of the fibers. Furthermore, the response of the element is derived by integration of the response of the sections along the length of the element.

In the fiber element model, proper material models for concrete and steel reinforcing bar take very important roles. Subjected to seismic action, the structures suffer repeated loading and unloading and the elements of the structures could undergo elastic and plastic deformation. Hereby, the material model for steel reinforcement should consider the cyclic stress-strain behaviors including inelastic buckling.

1.1.1 Importance of Inelastic Buckling

Under compressive load, the bearing capacity of the steel column depends on the slenderness of the column. As shown in Figure 1.2, the bearing capacity of the pin-ended column under axial force could be divided into three ranges: the plastic strength, the inelastic strength and the elastic strength (Quimby, 2008).

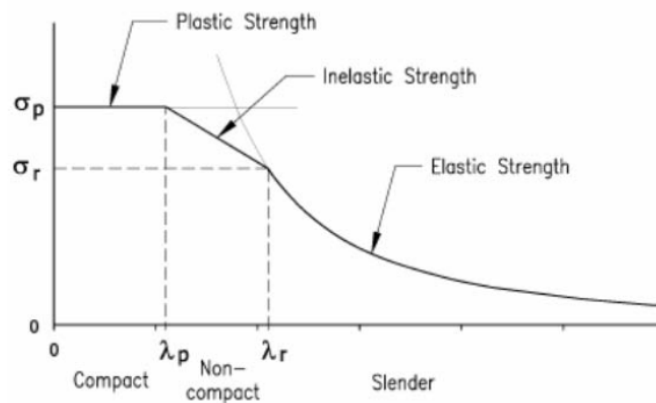


Figure 1.2 Bearing capacity of column

The computational slenderness λ is defined as the ratio between the computational length of the element L and the radius of gyration i . λ_r is the critical slenderness between inelastic buckling and elastic buckling, and σ_r is the corresponding stress, defined as $\sigma_r = \pi^2 E / (L/r)^2$ according to Euler's Equation; λ_p is the critical slenderness between plastic and inelastic buckling and σ_p is the corresponding buckling stress. Inelastic buckling of the rebar will emerge in the reinforced concrete structures under compressive loads.

In Figure 1.3, the theoretical model for the longitudinal rebar is illustrated based on the assumption that the buckling of the rebar emerges inside the consecutive stirrups.

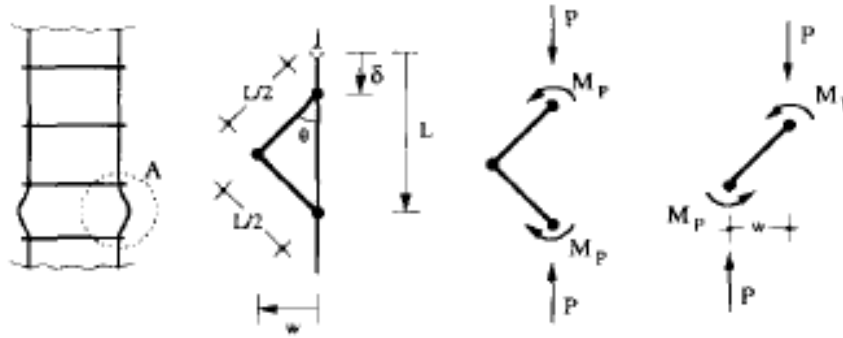
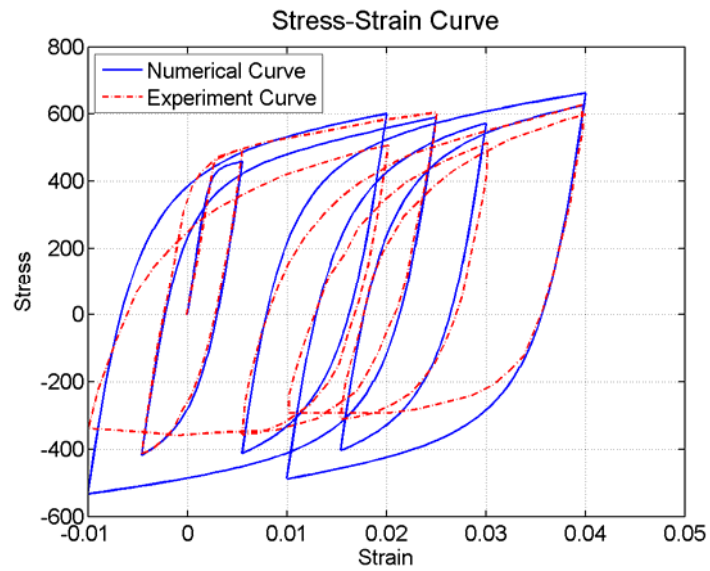
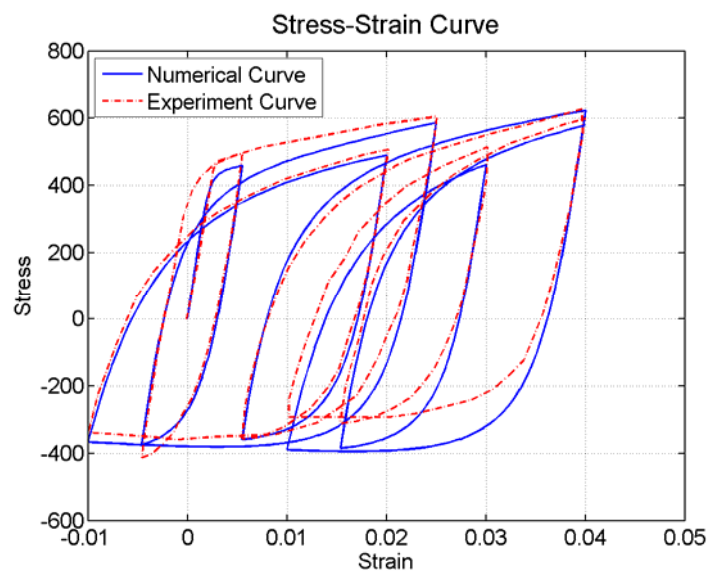


Figure 1.3 Theoretical model for the reinforced bar in the concrete columns (Gomes & Appleton, 1997)

The effect of the inelastic buckling on the cyclic behavior of the rebar could be observed in Figure 1.4. If the steel material model doesn't consider the inelastic buckling, the maximum response of the rebar in compression will be overestimated up to 50%. Hence the buckling effect has to be considered properly in the theoretical model for the rebar.



a) Cyclic model for rebar without inelastic buckling



b) Cyclic model for rebar with inelastic buckling

Figure 1.4 The effect of the inelastic buckling on the stress-strain curve

1.1.2 Rebar Applied in the Concrete Structures

Originally concrete structures are unreinforced. Concrete is a material that is very strong in compression but relatively weak in tension. To compensate this imbalance in concrete's behavior, rebar (short for reinforcing bar) is embedded in the concrete to increase the tensile bearing capacity.

Steel has an expansion coefficient nearly equal to the concrete; therefore, this feature could avoid the additional stress between the concrete and the rebar resulting from the temperature in the structure different from the original setting temperature. Hence steel rebar is widely used in the concrete structures, and the mostly widely applied steel rebar is the carbon steel rebar with rib which could bind with concrete effectively. However the cracking of the concrete is inevitable and this makes the carbon steel rebar susceptible to rust. As rust takes up greater volume than the steel from which it was formed, it causes severe pressure on the surrounding concrete, leading to cracking, spalling and ultimately failure of the structures (Tullmin, 2010). This is a particularly problem where the concrete is exposed in the salt water or in the marine applications. Corrosion-resistant rebar such as the stainless steel rebar could be used in this situation at a greater initial expense, but significantly lower expense over the service life of the project (Knudsen, Jensen, Klinghoffer, & Skovsgaard, 1998).

However, according to the experimental tests of the stainless steel rebar (Albanesi, Lavorato, & Nuti, 2006), the mechanical properties are different from the carbon steel rebar. The yield stress of the stainless steel rebar in tension is different from that in compression, named as anisotropy. For the carbon steel rebar, the yield stress is the same both in tension and in compression. The anisotropy of the stainless steel rebar should be considered in the numerical model for the stainless steel rebar.

1.2 LITERATURE REVIEW

A lot of numerical models for steel reinforcement have been proposed to describe the stress-strain relationship of the rebar. All the models could be divided into three classes (Filippou, Popov, & Bertero, 1983): the implicit algebraic model, the explicit algebraic model and the differential model,

and among which the algebraic models are widely used in the numerical analysis with the Finite Element Method (FEM).

1.2.1 Cyclic Steel Model for Rebar

As for the implicit algebraic model, the stress is the independent variable and the strain is the dependent variable.

Ramberg and Osgood (1943) proposed the well-known implicit monotonic model to simulate the stress-strain relationship of steel sheet, based on the experimental tests on aluminum alloy, stainless steel and carbon steel sheet.

The stress-strain relationship is defined in Eq. (1.1), where E is the elastic modulus, K and n are the parameters to describe the strain hardening.

$$\varepsilon = \frac{\sigma}{E} + \alpha \frac{\sigma}{E} \left(\frac{\sigma}{\sigma_0} \right)^{n-1} \quad (1.1)$$

Then Aktan et al. (1973) described the stress-strain relationship for each half-cycle between two stress-reversals using the Ramberg-Osgood function, illustrated in Figure 1.5, defined in Eq. (1.2).

$$\frac{\varepsilon - \varepsilon_i}{\varepsilon_0} = \frac{\sigma - \sigma_i}{\sigma_0} + \left(\frac{\sigma - \sigma_i}{\sigma_0} \right)^\alpha \quad (1.2)$$

Where ε and σ denote the strain and stress, and ε_i and σ_i are the initial values of the strain and stress at the beginning of the half cycle. ε_0 and σ_0 are the yield strain and yield stress, and α is the parameter of the Ramberg-Osgood function.

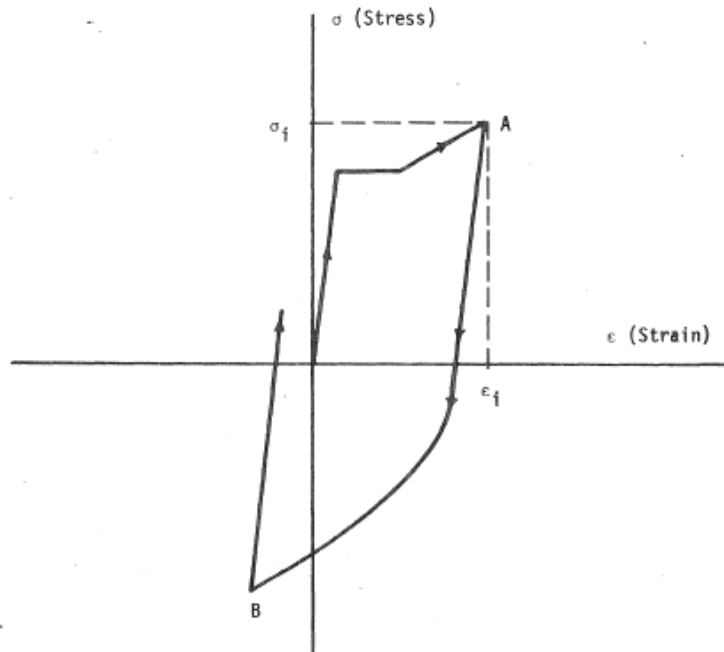
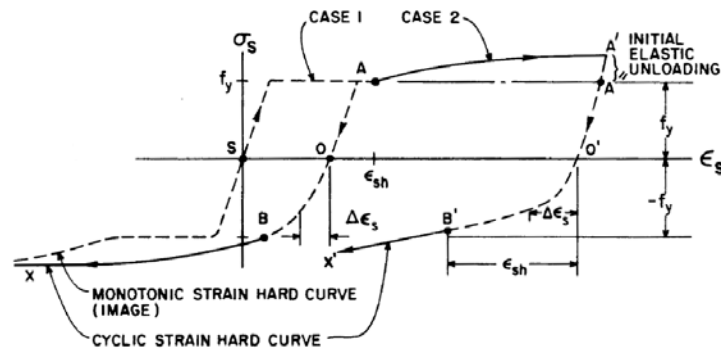
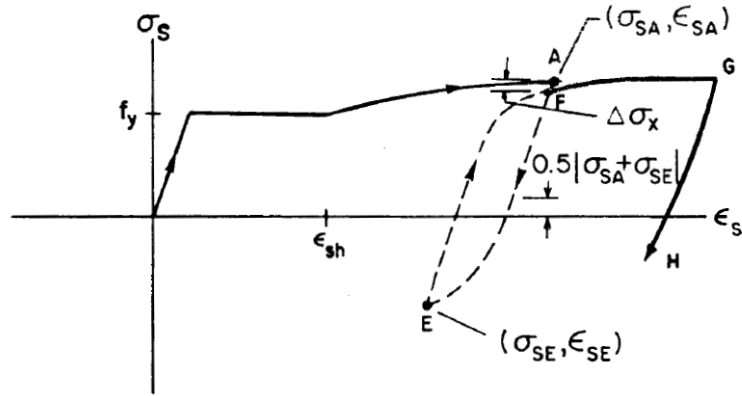


**Figure 1.5 Cyclic model proposed by Aktan et al. (1973)
based on Ramberg-Osgood Model**

Ma, Bertero, and Popov (1976) divided each half cycle into elastic, plastic and hardening periods, and proposed a series of rules to describe the cyclic unloading and reloading stress-strain relationship respectively, based on the Ramberg-Osgood model, as shown in Figure 1.6.



a) Unloading $\sigma - \epsilon$ stress-strain curve of the first reversal half cycle



b) Reloading $\sigma - \epsilon$ curve of the second reversal and subsequent half cycles

Figure 1.6 Cyclic model for rebar proposed by Ma et al. (1976) based on Ramberg-Osgood model

Thompson and Park (1978) proposed the cyclic model adopting the Ramberg-Osgood model with empirical constants to describe the cyclic stress-strain relationship. As shown in Figure 1.7, the stress-strain curve for monotonic loading, with suitably adjusted origin of co-ordinates, is used to describe the envelope which the steel stress cannot exceed.

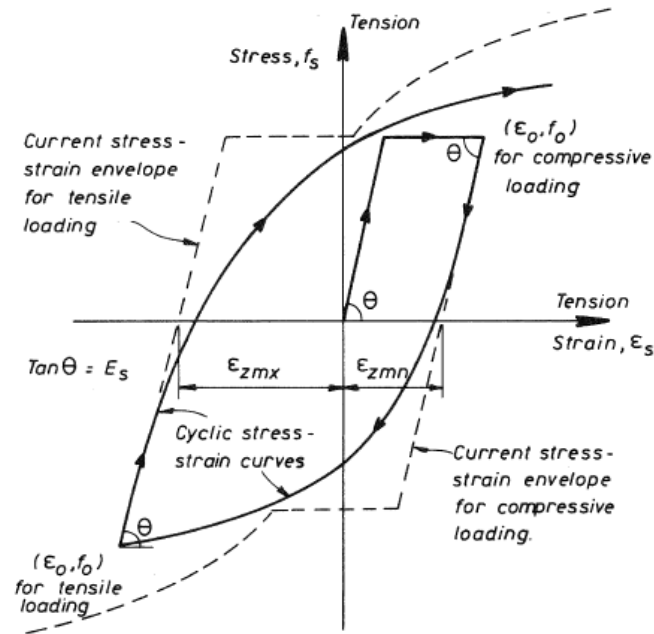


Figure 1.7 Cyclic stress-strain curve with envelope proposed by Thompson and Park (1978) based on Ramberg-Osgood model

On the contrary, in the explicit algebraic model, the strain is the independent variable, and the corresponding stress is the dependent variable.

One multiline model was proposed by Aktan et al. (1973) to simulate the cyclic behaviors including isotropic hardening. The initial stress-strain relationship is elastic-plastic with strain hardening slope. If any plastic strain is obtained for the half cycle before the reversal, the boundary of the hardening line will shift against the horizontal axial. Meanwhile, the slope of the hardening line is less than the slope of the previous hardening line, as illustrated in Figure 1.8.

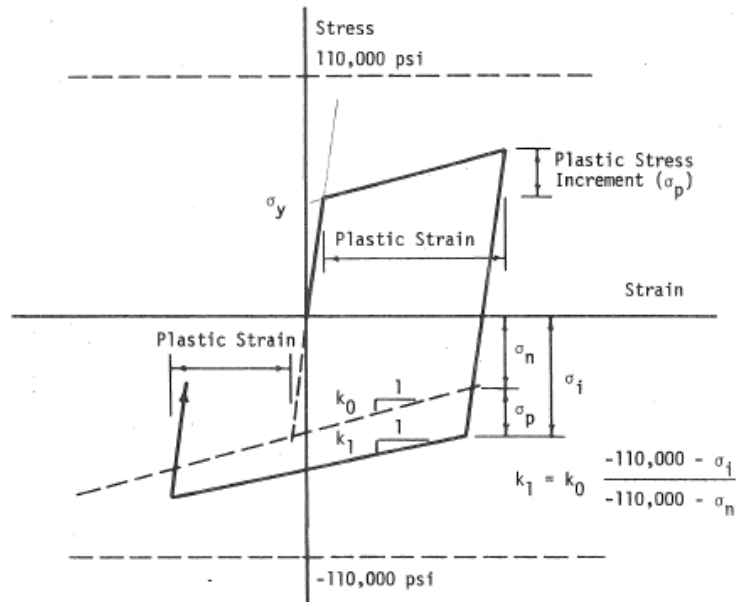


Figure 1.8 Cyclic stress-strain curve with envelope proposed by Aktan et al. (1973)

Then Aktan and Ersoy (1980) suggested another multilinear model to describe the cyclic behaviors of reinforcing bars considering the Bauschinger Effect, illustrated in Figure 1.9.

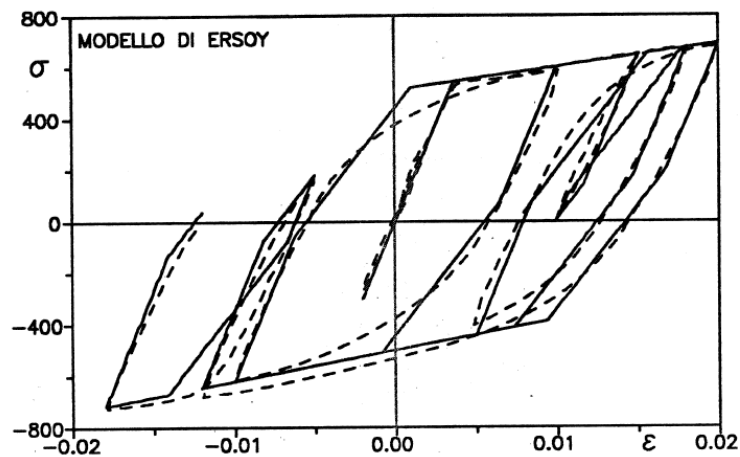


Figure 1.9 Cyclic model proposed by Aktan and Ersoy (1980)

Menegotto and Pinto (1973) built up a widely applied explicit model which was first proposed by Giuffre and Pinto (1970). The stress-strain relationship is defined by Eq. (1.3):

$$\sigma^* = b\varepsilon^* + \frac{(1-b)\varepsilon^*}{(1+\varepsilon^{*R})^{\frac{1}{R}}} \quad (1.3)$$

where b is the hardening ratio between the tangent modulus of the asymptote after yielding point and the initial tangent modulus at the original point or reversal point, defined in Eq. (1.4); the normalized stress σ^* and strain ε^* are defined in Eq. (1.5); the curved transition from the initial asymptote with initial tangent modulus E_0 to the hardening asymptote with slope equal to bE_0 is defined by R in Eq. (1.6).

$$b = \frac{E_s}{E_0} \quad (1.4)$$

$$\varepsilon^* = \frac{\varepsilon - \varepsilon_r^n}{\varepsilon_y^{n+1} - \varepsilon_r^n} \quad \text{and} \quad \sigma^* = \frac{\sigma - \sigma_r^n}{\sigma_y^{n+1} - \sigma_r^n} \quad (1.5)$$

ε_r^n and σ_r^n are the strain and stress corresponding to the reversal point which is the intersection between the n th half cycle and $n+1$ half cycle. ε_y^{n+1} and σ_y^{n+1} are the strain and stress corresponding to the yield point of the $n+1$ half cycle. The yield point is the intersection of the asymptotes which are the envelope of the $n+1$ half cycle. The asymptote at the reversal point is determined by the reversal point $(\varepsilon_r^n, \sigma_r^n)$ and the unloading slope ratio E_0 . Subsequently, the yield stress σ_y^{n+1} could be determined by the yield stresses σ_y^1 and σ_y^n , strains ε_y^n and ε_r^n and hardening ratio b . Then ε_y^{n+1} could be obtained by σ_r^n , σ_y^{n+1} and tangent modulus E_0 . Hereby the second asymptote could be determined by the yield point and the hardening ratio b .

$$R_{n+1} = R_0 - \frac{A_1 \xi_n}{A_2 + \xi_n} \quad (1.6)$$

In Eq. (1.6), ξ_n is the plastic excursion at the nth semi cycle normalized by the strain ε_y corresponding to the initial yield stress f_y , defined as: $\xi_n = (\varepsilon_r^n - \varepsilon_y^n) / \varepsilon_y$; R_0 is the initial curvature value, A_1 and A_2 are the constant parameters depending on the material properties. The greater the value of R , the steeper the transition curve.

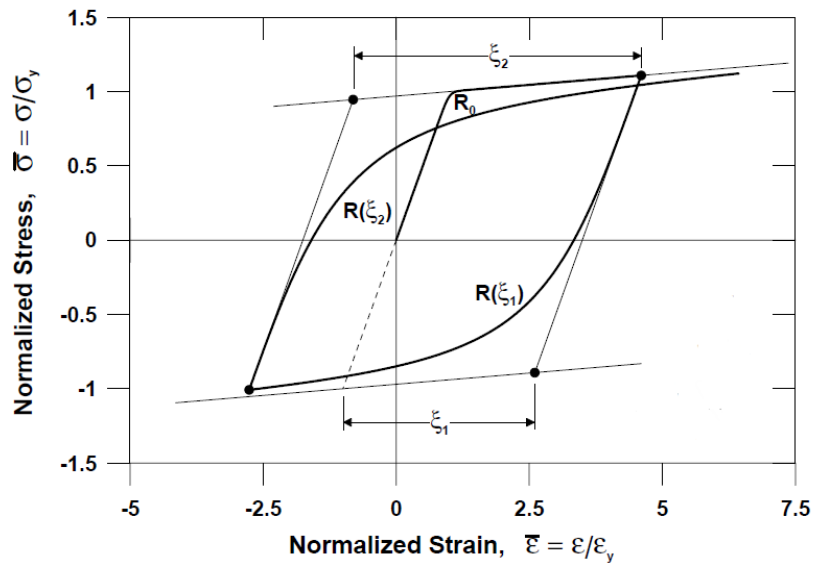
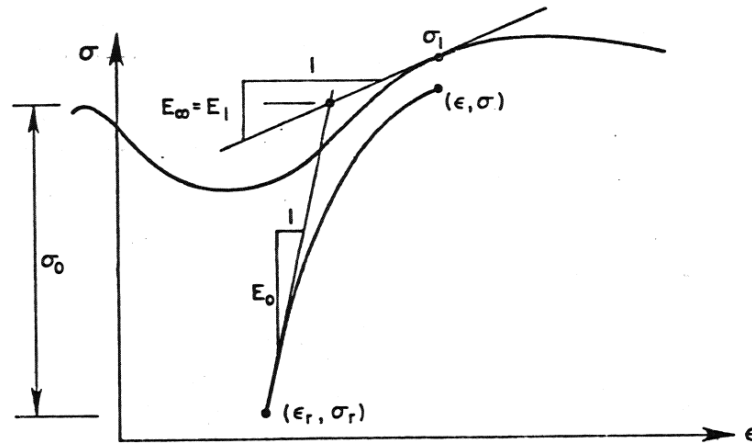


Figure 1.10 Menegotto-Pinto Model

The typical cyclic stress-strain curve depicted by the Menegotto-Pinto model is shown in Figure 1.10. For the first half cycle from the origin, the yield point is A, the curve transition parameter R equals R_0 . At the reversal B, the asymptote (2) is determined and thus the yield point of the unloading half cycle is obtained which is the intersection C of the asymptote (2) and (3). The curve transition parameter R_1 is calculated according to ξ_1 the plastic excursion of the last half cycle. Likewise, the yield point F and the curve transition parameter R_2 are determined at the reversal point D.

Stanton and McNiven (1979) compared the Ramberg-Osgood model and the Menegotto-Pinto model and pointed out that the Menegotto-Pinto demonstrated advantages over the Ramberg-Osgood model. The Menegotto-Pinto model could generate numerical curve with more

computational efficiency and smaller minimum error. The authors pointed out that the second envelope in the original Menegotto-Pinto model, which is a straightline and is definitely not the real dynamic envelope of the typical steel, should be replaced by monotonic skeleton curve. Furthermore, the authors studied the effect of the strain hardening on the cyclic stress-strain relationship of the rebar and proposed one function to calculate the stress shift at each reversal, in Figure 1.11.



**Figure 1.11 Modified Menegotto-Pinto model
by Stanton and McNiven (1979)**

Filippou, Bertero and Popov (1983) thought that the original Menegotto-Pinto Model could simulate the real stress-strain relationship accurately enough if the strain hardening is considered properly. The authors put forward Eq. (1.7) to calculate the stress shift due to isotropic hardening.

$$\sigma_{st} = \sigma_y a_3 \left(\varepsilon_{\max} / \varepsilon_y - a_4 \right) \quad (1.7)$$

Where ε_{\max} is the absolute maximum value at the reversal of previous half cycles, ε_y and σ_y , respectively, are the yield strain and yield stress, and a_3 and a_4 are the experimentally determined parameters.

Dodd and Restrepo (Dodd & Restrepo-Posada, 1995) built one model for the cyclic behaviors of carbon steel rebar without buckling and proposed the empirical formulas for updating the tangent modulus at reversal in

tension and compression respectively, which could be used to modify the Menegotto-Pinto model.

1.2.2 Steel Model Incorporating Inelastic Buckling

Monti and Nuti (1992) proposed the first model which could consider the buckling of the reinforcement based on a series of experimental tests on carbon steel rebar. The authors proposed a series of rules to consider the effects of strain hardening on the yield stress and hardening ratio between the second asymptote and the first asymptote.

The Monti-Nuti model is proposed based on the experimental observation of carbon steel rebar FeB44 with yield stress 450 MPa which was produced in Italy. The effect of the yield stress of different types of rebar is not considered properly in the model.

Gomes and Appleton (1997) built up one model describing the monotonic compressive skeleton curve based on the equilibrium of plastic mechanism of a buckled rebar. The authors describe the buckled compressive branch with the proposed model and simulate the tensile branch and the unbuckled compressive branch with the Menegotto-Pinto model. The combined model is illustrated in Figure 1.12.

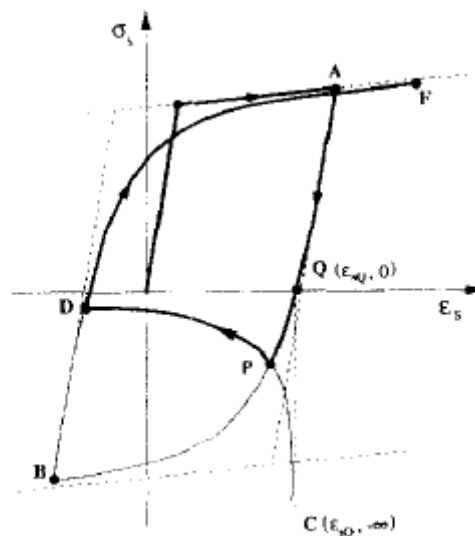
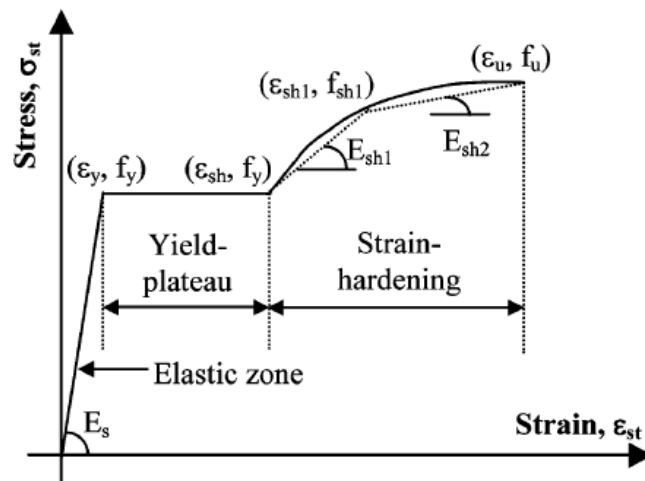


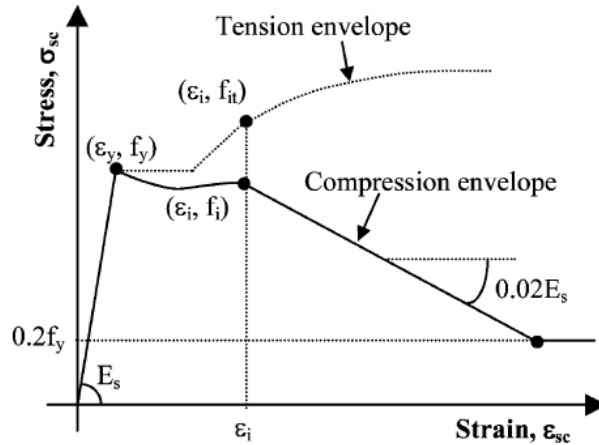
**Figure 1.12 Combination of Gomes and Appleton Model
and Menegotto-Pinto Model**

The Gomes-Appleton Model is set up based on the equilibrium equation of fix-ended column and assumption that the plastic hinge occurs in the midspan of the column. This model doesn't consider the effect of cyclic loading and unloading on the yield stress variation.

Dhakai and Maekawa (2002b) suggested the monotonic skeleton curves of reinforcement in tension and compression, respectively, shown in Figure 1.13. Also the authors presented formulas to update the tangent modulus at the reversal points in tension and compression, respectively. Then the parameter b in the Menegetto-Pinto model is modified and the skeleton curves are applied to describe the stress-strain relationship when the strain exceeds the attained maximum or minimum strain of previous half cycles. This model doesn't consider the yield stress variation at the reversal.



a) Monotonic tensile skeleton curve



b) Monotonic compressive skeleton curve

Figure 1.13 Monotonic Skeleton curve proposed by Dhakal and Maekawa(2002b)

Kunnath, Heo, and Mohle (2009) developed the combined material model in OpenSees named as “ReinforcingSteel” based on the Chang and Mander (1994) uniaxial steel model incorporating Gomes-Appleton model and Dhakal-Maekawa model.

Zong (2010) proposed the “beam on spring” model to simulate the stiffness of the confinement from the transverse stirrups, as illustrated in Figure 1.14, and then the model was simplified into trilinear model to adopt the “Hysteretic” material model in OpenSees, shown in Figure 1.15. The formulas in the model are empirical formulas derived through data fitting on a series of numerical data generated by the 3D FEM model of the rebar.

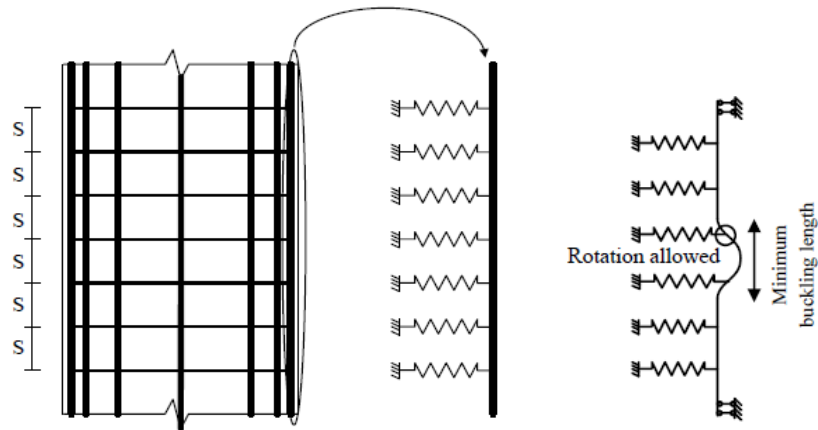
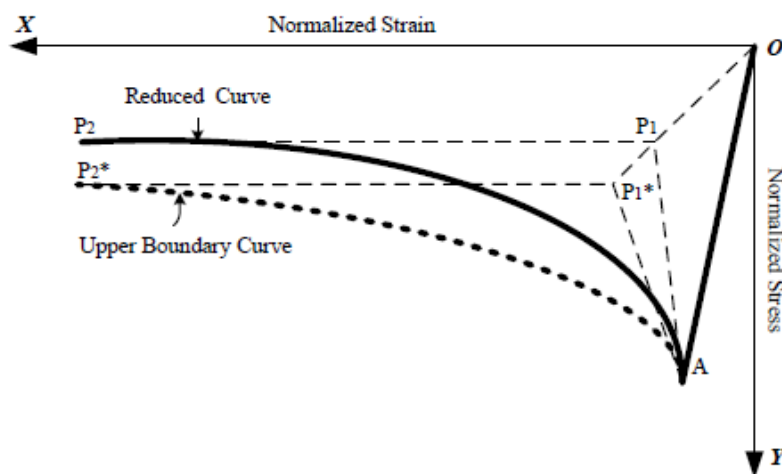
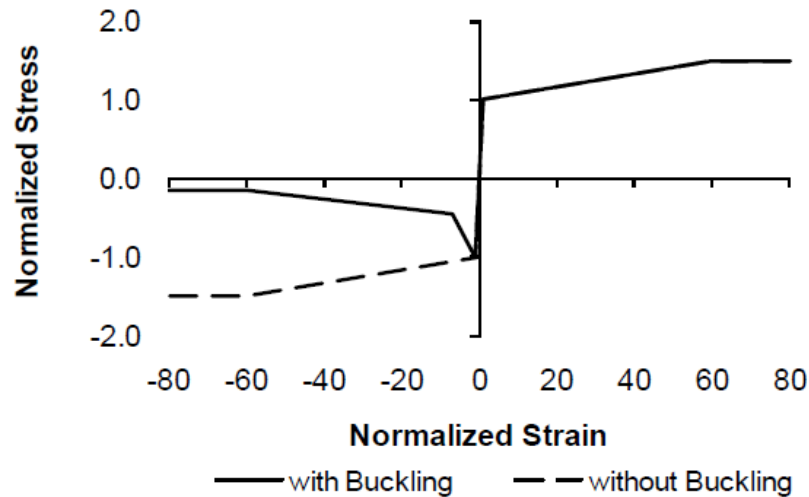


Figure 1.14 Schematic Diagram of rebar in Concrete Column



a) model proposed by Zong (2010)



b) proposed model application in OpenSees

Figure 1.15 Trilinear Model proposed by Zong (2010)

1.3 SIGNIFICANCE AND AIMS OF CURRENT RESEARCH

The proper steel material model for rebar incorporating buckling is crucial for the seismic analysis of the reinforced concrete structures. In this paper, the modified Monti-Nuti model is proposed and the effectiveness is demonstrated.

1.3.1 Significance

As introduced above, evaluation of the seismic performance of existing reinforced concrete structures is important to ensure the inhabitants and property safe in case of earthquake. The accurate cyclic model for rebar incorporating inelastic buckling is very important for seismic analysis of the concrete structures (Bae, Miseses, & Bayrak, 2005).

In this study, cyclic behaviors of different types of rebar are carefully researched and one improved Monti-Nuti model for rebar is proposed.

This model solves the drawbacks of existing model and could obtain more accurate result with less computational cost.

1.3.2 Aims of Current Research

In this thesis, one modified Monti-Nuti model is proposed to simulate the cyclic behaviors of rebar such as carbon steel rebar and stainless steel rebar, based on the experimental and numerical study of carbon steel rebar and stainless steel rebar.

The parameters in the modified Monti-Nuti model are identified by the Genetic Algorithm. The effectiveness and robustness of the parameters are verified.

The modified material model is implemented in the OpenSees, and the material model is named as “Steel05”.

The numerical curves generated by the modified model are calibrated with the experimental curves.

The material model is applied in the structural analysis of cantilever column.

Finally, the effect of corrosion of rebar on the cyclic stress-strain behavior is studied and the corrosion extend model is proposed.

1.4 Organization of this Thesis

In section 2, the essence of the original Monti-Nuti model is explained in detail. In section 3, the drawbacks of the original model are studied and then the improved Monti-Nuti is proposed. In section 4, the parameters in the model are identified by the Genetic Algorithm and the formulas for the parameters are proposed. In section 5, the implementation of the material in OpenSees is briefly introduced, and the numerical model is validated with the experimental curves. In section 6, the application of the modified Monti-Nuti model in reinforced concrete piers is made to verify the effectiveness of the new material model. In section 7, the effects of corrosion of rebar are studied and the corrosion extended model is proposed. Finally in section 8, main conclusions and the further work are briefly discussed.

2. ORIGINAL MONTI-NUTI MODEL

The Monti-Nuti Model is proposed based on experimental observation of the carbon steel rebar (Giorgio Monti & Nuti, 1992). This model consists of four hardening rules such as kinematic rule, isotropic rule, memory rule and saturation rule. The model calculates the yield stress, elastic modulus, hardening ratio and the curve transition parameter at each reversal, which considers the effects of strain hardening in absence of buckling and in presence of buckling respectively.

2.1 MONOTONIC SKELETON CURVE

A series of experiments on carbon steel rebars Feb44, with yield stress equal to 450 MPa, diameter $D=16, 20, 24$ mm, were tested under monotonic tensile, compressive and cyclic loads, and the monotonic curves are illustrated in Figure 2.1.

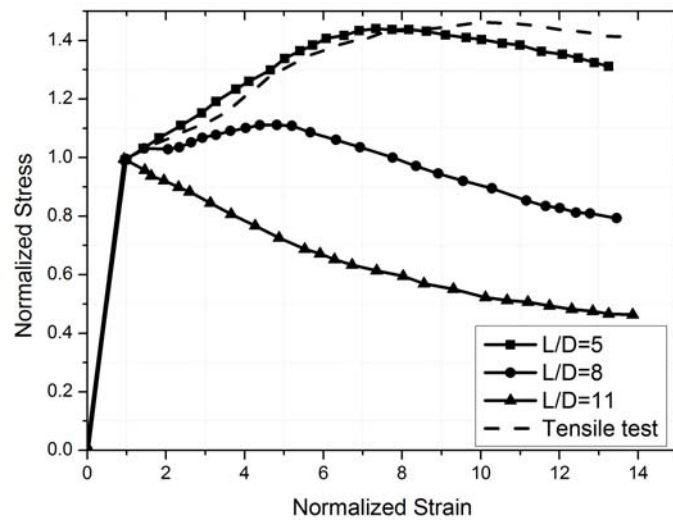


Figure 2.1 Monotonic tests of carbon steel rebar (Giorgio Monti & Nuti, 1992)

Several observations could be obtained in Figure 2.1. 1) the tensile monotonic curves are identical regardless of the slenderness of the rebar; 2) even though the diameters of the rebars are different, the monotonic compressive could be identical if the slenderness ratios L/D are equal; 3) when the slenderness ratio L/D equals 5, the monotonic compressive curve coincides with the monotonic tensile curve; 4) when the slenderness ratio L/D is 11, the monotonic compressive curve diverges from the tensile curve as soon as it reaches the yield point; 5) when the slenderness ratio L/D varies between 5 and 11, the compressive curve coincides with the tensile curve for certain length, and then the compressive curve diverges from the tensile curve.

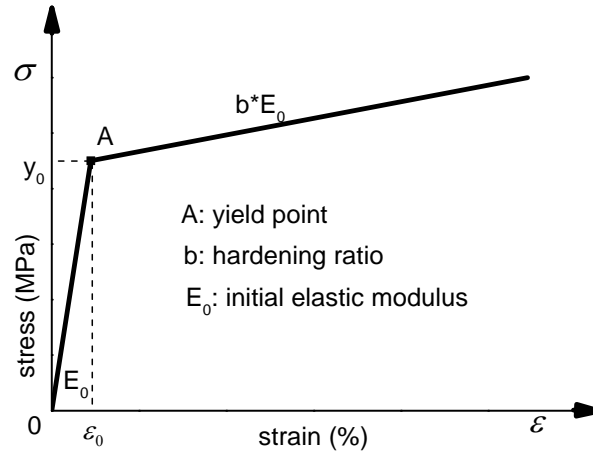
The skeleton curve for the rebar in the Monti-Nuti model is shown in Figure 2.2. The skeleton curve in tension is a bilinear curve. As shown in Figure 2.2 a), the slope of the first line is the initial tangent modulus E_0 , after the stress exceeds the yield stress σ_y^0 , the curve converts to the second line with slope equal to bE_0 , where b is the hardening ratio.

The monotonic compressive skeleton is shown in Figure 2.2 b). After the stress reaches the yield point A, the path for the curve depending on the slenderness ratio L/D :

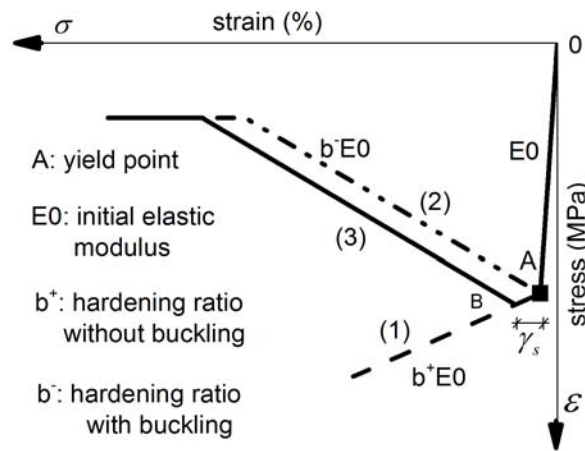
The curve converts to the line (1) with the slope ratio equal to $b_0^+E_0$, where b_0^+ is positive and equals the hardening ratio in the tensile curve, if the slenderness ratio $L/D \leq 5$;

The curve converts to the line (2) with the slope ratio $b_0^-E_0$, where b_0^- is negative representing the hardening ratio in compression, if the slenderness ratio $L/D \geq 11$;

The curve follows the line (1) for length γ_s until point B, and then swiths to line (3) with slope ratio $b_0^-E_0$, if the slenerness ratio $5 < L/D < 11$.



a) Tensile skeleton curve



b) Compressive skeleton curve

Figure 2.2 Monotonic skeleton curve of Monti-Nuti model

γ_s is the superposition length between the monotonic tensile curve and the monotonic compressive curve after the yield point, and the formula is given in Eq. (2.1) based on the experimental observation.

$$\gamma_s = \frac{11 - L/D}{e^{c(L/D-5)} - 1} \geq 0 \quad \text{for } 5 < L/D \leq 11 \quad (2.1)$$

c is a parameter related to the rebar, and the given as 0.5 in the test.

2.2 HARDENING RULES FOR CYCLIC BEHAVIORS OF STEEL REBAR

As mentioned above, the effect of strain hardening on the cyclic behaviors of stress-strain curves should be considered properly if the Menegotto-Pinto Model is adopted to simulate the cyclic behaviors of reinforcing bar. The Monti-Nuti model could update the yield stress of each half cycle and the hardening ratio between the hardening modulus and the initial elastic modulus.

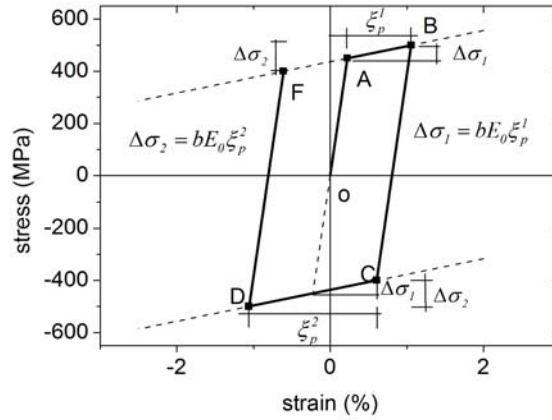
The stress variation is calculated by equations incorporating the strain hardening which represents the plastic deformation of the rebar after exceeding the yielding point. If an isotropic specimen under tension or compression is loaded exceeding the yield strength, and then it is unloaded and reloaded towards the opposite direction, the yield strength will become smaller or larger due to the plastic deformation at pervious loading process. The effect of the plastic deformation could be divided into kinematic hardening and isotropic hardening.

According to the experimental results, the critical slenderness L/D equals 5, where L is the distance between the subsequent transversal rebars and D is the diameter of the longitudinal rebars. If the slenderness L/D exceeds 5, the buckling could be observed in the experimental stress-strain curves, otherwise, no buckling occurs. The effects of strain hardening in absence of buckling and in presence of buckling are different.

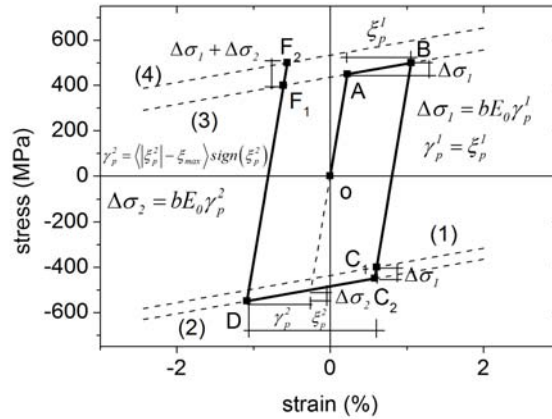
2.2.1 In Absence of Buckling

The kinematic hardening results in the yield stress reduction in the opposite direction after the specimen is loaded exceeding the yield strength in tension or compression. The kinematic hardening could explain the Bauschinger Effect. This kinematic hardening is considered in the original Menegotto-Pinto model. In Figure 2.3 a), the yield stress

corresponding to point C is $\Delta\sigma_1$ smaller than that of point A due to the kinematic strain hardening ξ_p^1 . Meanwhile, the yield stress corresponding to point F is $\Delta\sigma_2$ smaller than the enlarged yield stress corresponding to point B in tension, due to the kinematic strain hardening ξ_p^2 in the second half cycle. In one word, the effect of the kinematic is to pull the yield strength towards the horizontal axis.



a) Effect of kinematic hardening



b) Effect of isotropic hardening

Figure 2.3 Effect of strain hardening in absence of buckling

On the contrary, the isotropic strain hardening causes the yield stress to increase in the opposite direction. As shown in Figure 2.3 b), the isotropic strain hardening ξ_p^1 causes the yield point in the second half cycle to move from C_1 to C_2 . Likewise, the isotropic strain hardening ξ_p^2 results in the shift of the yield point from F_1 to F_2 . However the isotropic hardening will have no effect on the stress variation if the absolute value of the plastic deformation (like $|\xi_p^2|$) doesn't exceed the absolute value of the maximum plastic deformation of previous half cycles (like ξ_{\max}). This means that the isotropic hardening has the memory character which decides that the isotropic hardening only take effect when the current strain hardening is beyond the maximum previous plastic strain deformation. Different from the effect of the kinematic hardening, the effect of the isotropic hardening is to transfer the yield point away from the horizontal axis.

A half cycle is the path between two subsequent load reversals. The plastic excursion at the n th half cycle is defined in Eq. (2.2):

$$\xi_p^n = \varepsilon_r^n - \varepsilon_y^n \quad (n = 1, 2, 3, \dots) \quad (2.2)$$

where ε_r^n is the strain corresponding to the reversal point at the end of the n th half cycle and ε_y^n is the strain corresponding to the yielding point which is the intersect of the two envelope lines at the n th half cycle, and is calculated according to Eq. (2.3).

$$\varepsilon_y^n = \varepsilon_r^{n-1} + \frac{\sigma_y^n - \sigma_r^{n-1}}{E} \quad (n = 2, 3, 4, \dots) \quad (2.3)$$

where σ_y^n is the yield stress of the n th half cycle, σ_r^{n-1} is the stress corresponding to the end reversal point of the $n-1$ half cycle.

Then the half cycle plastic work Φ_p^n decides the sign of the stress variation and is defined as follows, in Eq. (2.4):

$$\Phi_p^n = \frac{1}{2} (\sigma_r^n - \sigma_y^n) \xi_p^n \quad (2.4)$$

The hardening ratio b is always positive both in tension and in compression, so the stress increases with the strain increasing and the

stress reduces with the strain decreasing. Thereby the plastic work Φ_p^n is always positive in absence of buckling.

1. Kinematic rule

The kinematic rule corresponds to the effect of the kinematic strain hardening. The stress variation due to the kinematic rule is given in Eq. (2.5):

$$\Delta\sigma_K^n = \sum_{i=1}^n bE\xi_p^i \quad (2.5)$$

For each half cycle, the stress variation $bE\xi_p^i$ reduces the absolute value of the yield stress in the opposite direction.

2. Isotropic rule

The isotropic rule corresponds to the effect of the isotropic strain hardening. The stress variation due to the isotropic rule is defined in Eq. (2.6):

$$\Delta\sigma_I^n = \left[\sum_{i=1}^n |bE\xi_p^i| \text{sign}(\Phi_p^n) \right] \text{sign}(-\xi_p^n) \quad (2.6)$$

where $\text{sign}(x)$ is the sign function: $\text{sign}(x)=1$ if $x>0$; $\text{sign}(x)=-1$ if $x<0$; otherwise $\text{sign}(x)=0$.

The stress variation due to the isotropic rule is always opposite to the strain variation of current half cycle, thus it will always increase the yield stress in the opposite direction.

3. Memory rule

According to the experimental results, if the plastic excursion at current half cycle ξ_p^n doesn't exceed the maximum plastic excursion of the previous $n-1$ half cycles ξ_p^{\max} , no isotropic hardening develops at current half cycle. Thus one new symbol γ_p^n is defined in Eq. (2.7) to describe this character.

$$\gamma_p^n = \left\langle |\xi_p^n| - \xi_p^{\max} \right\rangle \text{sign}(\xi_p^n) \quad (2.7)$$

where $\langle u \rangle = uH(u)$ is the step function. If $u > 0$, $H(u) = 1$; otherwise, $H(u) = 0$. Replace ξ_p^i in Eq. (10) with γ_p^i in Eq. (11), the stress variation due to the isotropic rule and memory rule is named as $\Delta\sigma_{IM}^n$ and is defined in Eq. (2.8):

$$\Delta\sigma_{IM}^n = \left[\sum_{i=1}^n |bE\gamma_p^i| \text{sign}(\Phi_p^i) \right] \text{sign}(-\xi_p^n) \quad (2.8)$$

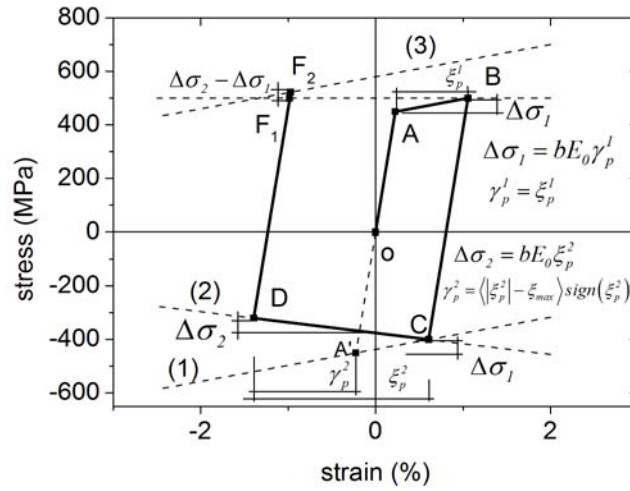
The yield stress at the n+1th half cycle could be calculated by Eq. (2.9):

$$\sigma_y^{n+1} = \sigma_y^1 \text{sign}(-\xi_p^n) + P\Delta\sigma_K^n + (1-P)\Delta\sigma_{IM}^n \quad (2.9)$$

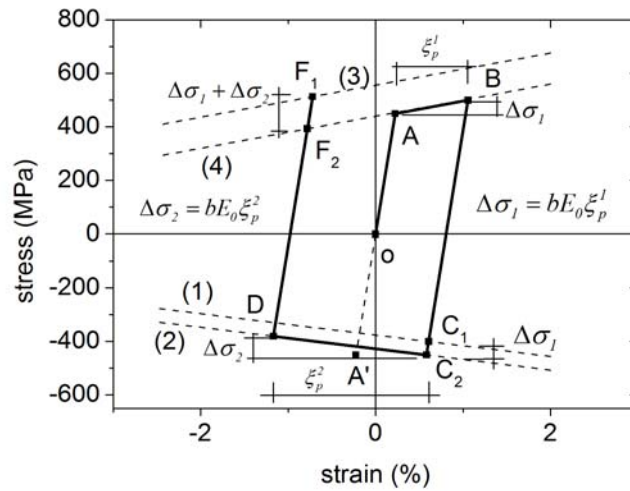
where P is the weight coefficient which determines the contribution made by the kinematic rule and the isotropic rule. The value of P depends on the properties of the material. In the experimental tests on the carbon steel rebar, P is given as 0.5 (Giorgio Monti & Nuti, 1992).

2.2.2 In Presence of Buckling

Due to buckling, the absolute value of the stress in compression decreases with the strain increasing after the unloading path exceeds the yield point. Hereby the effects of the kinematic hardening and isotropic hardening are different from that in absence of buckling.



a) Effect of kinematic hardening



b) Effect of isotropic hardening

Figure 2.4 Effect of strain hardening in presence of buckling

As shown in Figure 2.4 a), the effects of the kinematic hardening are different in tension and compression. The strain hardening in tension could cause the absolute value of the yield stress reduction in compression. The absolute value of the stress corresponding to point C is

smaller than the yield stress of point A. However, the strain hardening in compression increases the yield stress in tension (The yield point shifts from F_1 to F_2). Like the isotropic hardening rule in absence of buckling, the kinematic hardening will have no effect if the absolute value of the plastic hardening of current half cycle doesn't exceed the maximum plastic deformation of previous half cycles (for instance, if $|\xi_p^2| \leq \xi_{\max}$, the stress variation $\Delta\sigma_2=0$), which means that the kinematic hardening has the memory character in presence of buckling. In general terms, the effect of the kinematic hardening is to move the cyclic curve upwards in presence of buckling.

In Figure 2.4 b), the isotropic hardening will increase the absolute value of the yield stress in compression but reduce the yield stress in tension. In one word, the effect of the isotropic hardening is to shift the cyclic curve downwards (Move the yield point C_1 to C_2 and shift the yield point F_1 to F_2).

In presence of buckling, the half cycle plastic work Φ_p^n is still positive in tension, but it becomes negative in compression due to the stress increase with the strain decreasing as the hardening ratio b is negative in compression. Thus the rules corresponding to the kinematic strain hardening and isotropic hardening in presence of buckling are different from those in absence of buckling.

1. Kinematic rule and Memory rule

The stress variation due to the kinematic rule will not develop if the plastic excursion at current half cycle ξ_p^n doesn't exceed the maximum plastic excursion of the previous $n-1$ half cycles ξ_p^{\max} . Thus, the stress variation is calculated via the combination of the kinematic rule and the memory rule, and is given in Eq. (2.10):

$$\Delta\sigma_{KM,b}^n = \sum_{i=1}^n bE\gamma_p^i \quad (2.10)$$

In tension, the hardening ratio b and the additional plastic excursion γ_p^i are positive, thus $bE\gamma_p^i$ is positive, and then the absolute value of the yield stress in compression will reduce. In compression, the hardening

ratio b and the additional plastic excursion γ_p^i are negative, thus $bE\gamma_p^i$ is positive, which will result in the increase of the yield stress in tension.

2. Isotropic rule

The expression of stress variation is the same with that defined in absence of buckling. However, the effect of the isotropic rule is different. In tension the plastic work Φ_p^n is positive, thus the absolute value of the yield stress in compression will increase. In compression, the plastic work Φ_p^n is negative; as a result, the yield stress in tension will decrease.

The yield stress at the $n+1$ th half branch could be calculated according to the Eq. (2.11):

$$\sigma_y^{n+1} = \sigma_y^1 \text{sign}(-\xi_p^n) + P\Delta\sigma_{KM,b}^n + (1-P)\Delta\sigma_I^n \quad (2.11)$$

3. Stress shift

If the slenderness ratio $5 < L/D < 11$, as shown in Figure 2.5, the superposition length γ_s will be positive, thus the intersection between the two asymptotes will shift from the original yield point A to another position B. In order to eliminate the discontinuity, the shifted yield stress could be calculated according to Eq. (2.12), which is deduced based on geometrical considerations.

$$\sigma_{sh} = \gamma_s E \frac{b^+ - b^-}{1 - b^-} \quad (2.12)$$

Where E is the tangent modulus at the original point of the unloading half cycle, b^+ is the hardening ratio of the superposition zone, b^- is the slope of the buckled asymptote, which is negative.

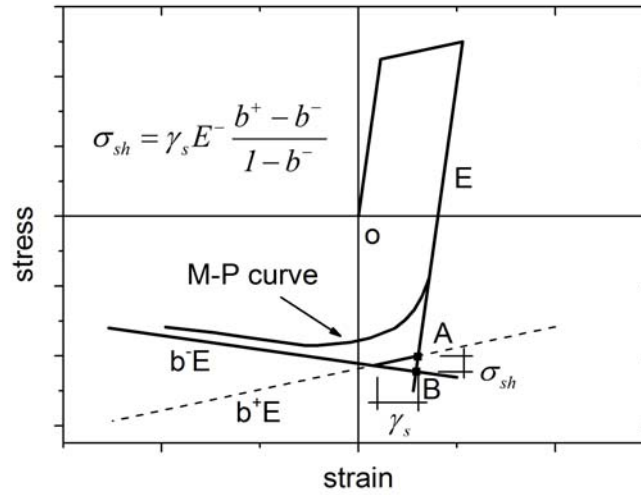


Figure 2.5 Stress shift in compressive curve

2.3 CURVE TRANSITION PARAMETER R

The curve transition parameter R defines the curvature of the transition from the first asymptote to the second envelope. The larger the value of R , the steeper the curve transition. In Figure 2.6, $R_0 > R(\xi_1) > R(\xi_2)$, the curve transition becomes smoother.



2.3.1 In Absence of Buckling

$$R_{n+1} = R_0 - \frac{A_1 \xi_{\max}}{A_2 + \xi_{\max}} \quad (2.13)$$

2.3.2 In Presence of Buckling

The parameters A_1 and A_2 in the formula corresponding to R , are modified according to the calibration of the experimental results, and the formula is given in Eq. (2.14).

$$R_{n+1} = R_0^b - \frac{A_1^b \xi_{\max}}{A_2^b + \xi_{\max}} > R_1^b \quad (2.14)$$

where ξ_{\max} is the maximum plastic excursion, defined as $\xi_{\max} = \max(|\xi_p^n|)$, $A_1^b = 19.5$, $A_2^b = 0.001$, R_0^b is defined in Eq. (2.15) and the lower boundary R_1^b is defined in Eq. (2.16).

$$R_0^b = R_0 - 2 \left[L/D - (L/D)_{cr} \right] \quad (2.15)$$

$$R_1^b = 10 \left[L/D - (L/D)_{cr} \right] b^+ \quad (2.16)$$

2.4 HARDENING RATIO

b represents the ratio between the hardening modulus and the initial elastic modulus at the reversal point. In Figure 2.7, the effect of b on the curve is illustrated. If $b > 0$, the stress increase with the increase of strain after the yield point; if $b < 0$, the stress reduce with increase of strain after the yield point.

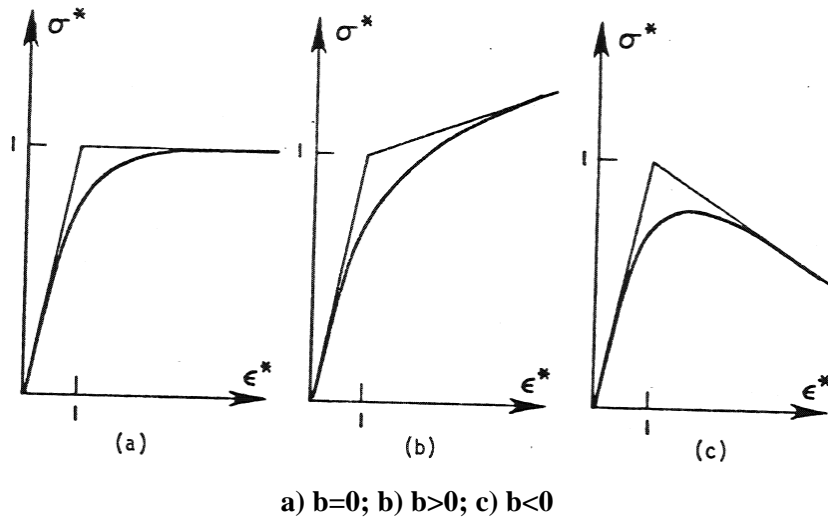


Figure 2.7 The effect of b on the curve transition

The initial value of b is determined by the mechanical properties of the material. Then the value of b varies according to the plastic deformation. In absence of buckling, b is updated by the same formula for tensile branch and compressive branch. In presence of buckling, b is defined for tensile branch and compressive branch respectively.

2.4.1 In Absence of Buckling

In the original Menegotto-Pinto model, the hardening ratio b is constant, which is always equal to the original hardening ratio b in the monotonic skeleton curve. According to the experimental observation, the hardening ratio b varies and is expressed in Eq. (2.17):

$$b^{n+1} = b_0 e^{(b_0 E \sum \gamma) / (\sigma_y - \sigma_\infty)} \quad (2.17)$$

where $\sum \gamma$ is the sum of additional plastic excursion of previous half cycles, defined as $\sum \gamma = \sum_{i=1}^n \gamma_p^i$, and σ_∞ is the limitation value of the asymptote for softening branch and the approximation of σ_∞ is evaluated by Eq. (2.18):

$$\sigma_\infty = \frac{6\sigma_y}{L/D} \quad (2.18)$$

2.4.2 In Presence of Buckling

The formulas for hardening b are different in tension and in compression due to buckling and are given in Eq. (2.19).

$$b^- = \begin{cases} b_0^+ e^{b_0^+ E \sum \gamma / (\sigma_y - \sigma_\infty)}, & \sum \gamma \leq \gamma_s \\ b_0^- e^{b_0^- E \sum \gamma (\sigma_y - \sigma_\infty)}, & \sum \gamma > \gamma_s \end{cases} \quad (2.19)$$

Where b_0^+ is the initial hardening ratio which could be obtained through monotonic tensile tests, and b_0^- is the strain hardening ratio of the first unloading branch and is given in Eq. (2.20).

$$b_0^- = a \left[\left(\frac{L}{D} \right)_{cr} - \frac{L}{D} \right] \quad \text{for } \frac{L}{D} > \left(\frac{L}{D} \right)_{cr} \quad (2.20)$$

in which, for the tested bars, $a = 0.006$.

2.5 ELASTIC MODULUS E

The elastic modulus at the reversal could be different from the original elastic modulus, as shown in Figure 2.8.

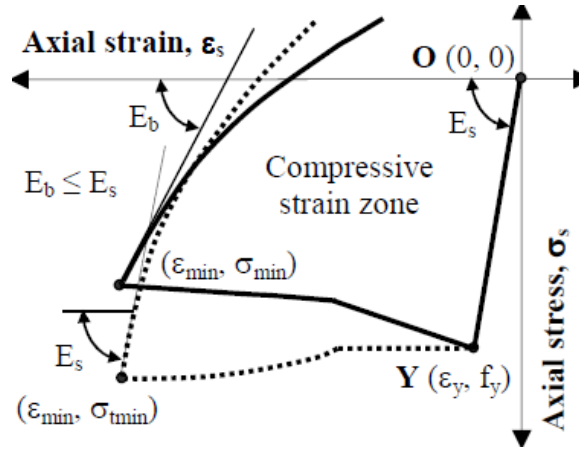


Figure 2.8 Degradation of elastic modulus

2.5.1 In Absence of Buckling

In absence of buckling, the elastic modulus at the reversal from compressive branch towards tensile branch could be considered as the same as the original elastic modulus of the first half cycle.

2.5.2 In Presence of Buckling

When the curve reloads from the compressive reversal point, the tangent modulus will reduce according to the experimental observation. Eq. (2.21) was proposed to evaluate the reduced modulus.

$$E = E_0 \left[A_5 + (1 - A_5) e^{-A_6 \left(\frac{\varepsilon_p^n}{\varepsilon_p} \right)^2} \right] \quad (2.21)$$

where E_0 is the initial elastic modulus; A_5 is defined by $A_5 = 1 + \left[(L/D)_{cr} - L/D \right] / 7.5$ and A_6 is set as 620 for the tested bars.

3. IMPROVEMENT OF THE ORIGINAL MODEL

The original Monti-Nuti model was proposed based on the experiments on Carbon Steel rebars FeB44 of the Italian production, with the nominal yielding strength 450 MPa (G Monti & Nuti, 1989). Three different slenderness ratios between Length L and diameter D such as $L/D=5, 8, 11$ were designed for the monotonic and cyclic tests. The diameters of the tested rebar are 16mm, 20mm and 24 mm (G. Monti & Nuti, 1990).

In the original model, the yield stresses of the tested rebars are identical, the effect of different yield stress of the rebar is not considered. In order to study the effect of yield stress on the original Monti-Nuti model, several experimental tests on rebar with yield stress equal to 500 MPa (Dhakal & Maekawa, 2002b) are simulated by the original Monti-Nuti model, and the geometric characteristics, mechanical properties and the loading strain histories are listed in Table 3.1.

Table 3.1 Properties of test rebar (Dhakal & Maekawa, 2002b)

<i>Test</i>	<i>L/D</i>	<i>f_y (MPa)</i>	<i>E_s (MPa)</i>	<i>b</i>	<i>Strain histories (%)</i>
S5	5	500	200000	0.037	+1 -1 +2 -2 +3 -3
S8	8	500	200000	0.037	+1 -1 +2 -2 +3 -3
S11	11	500	200000	0.037	+1 -1 +2 -2 +3 -3

The comparisons between the numerical curves of the rebars, with slenderness equal to 5, 8 and 11, generated by the original Monti-Nuti model and the experimental curves are shown in Figure 3.1, Figure 3.2 and Figure 3.3.

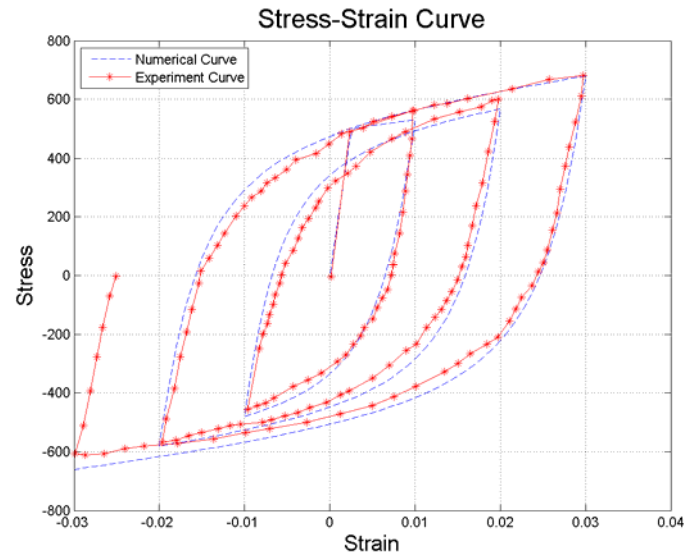


Figure 3.1 Comparison between experimental curve and numerical curve generated by original Monti-Nuti model (S5, L/D=5)

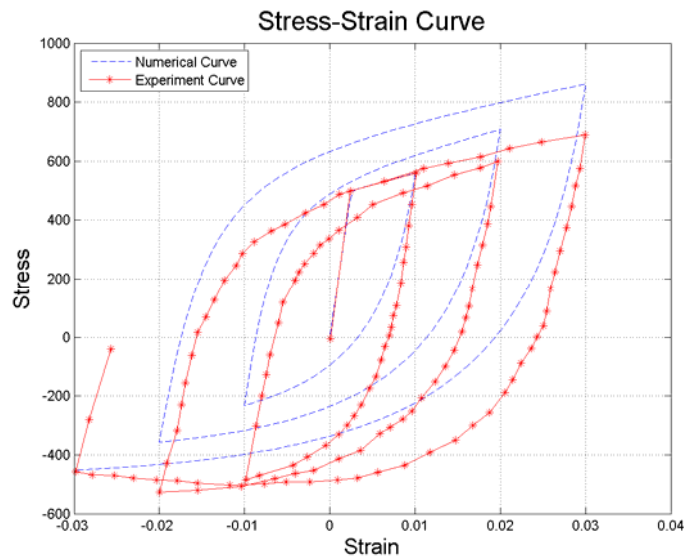


Figure 3.2 Comparison between experimental curve and numerical curve generated by original Monti-Nuti model (S8, L/D=8)

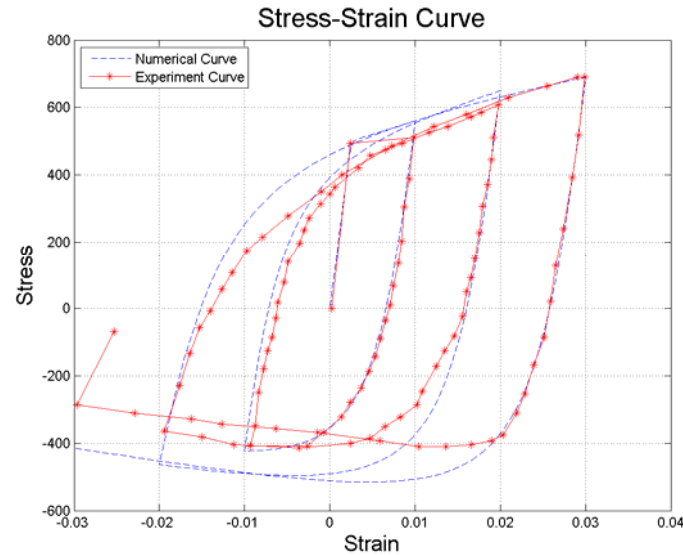


Figure 3.3 Comparison between experimental curve and numerical curve generated by original Monti-Nuti model (S11, L/D=11)

Obvious disagreements between the experimental curves and the numerical curves could be observed, especially in the curves for the rebar with slenderness equal to 8 and 11. This disagreement could be eliminated if the effect of the yield stress on the cyclic behaviors is considered properly.

The original Monti-Nuti model is able to simulate the rebar with the same yield stress in tension and in compression. However, some types of stainless steel rebar are not isotropic which means that the yield strengths in tension and in compression are different. The stainless steel rebar AISI304 or 1.4301, produced in Italy before 2008 according to the old product standard (DM14.01.08, 2008), shows obvious anisotropic (Albanesi et al., 2006). The chemical contents of the specimen are listed in

Table 3.2 and the monotonic stress-strain curve of the specimen is illustrated in Figure 3.4.

Table 3.2 Content of chemical composition in stainless steel AISI304

<i>AISI304</i>	<i>C</i>	<i>Si</i>	<i>Mn</i>	<i>P</i>	<i>S</i>	<i>N</i>	<i>Cr</i>	<i>Mo</i>	<i>Ni</i>
content	0.034	0.53	1.85	0.029	0.001	-	18.09	-	8.58

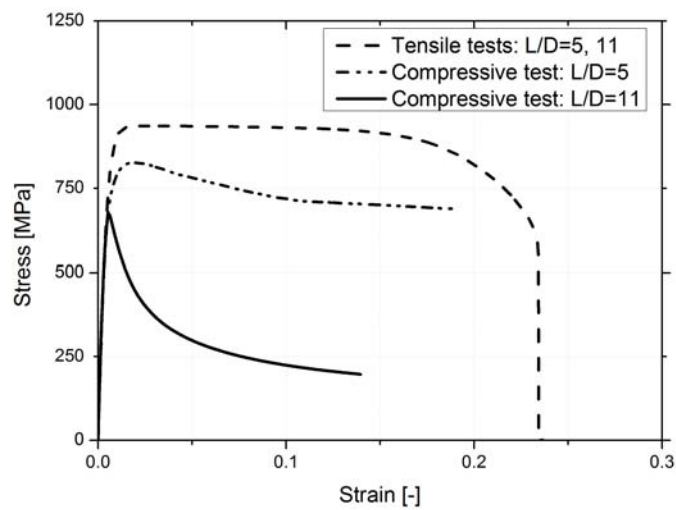


Figure 3.4 Monotonic tests on stainless steel rebar (AISI304 or 1.4301)

The yield stress of the specimen in tension is 790 MPa, while the yield stress in compression is 680 MPa.

Figure 3.5, Figure 3.6 and Figure 3.7 are the comparisons between the numerical curves generated by the original Monti-Nuti model and the experimental curves of stainless steel rebar with slenderness L/D equal to 5.

The original Monti-Nuti is not able to capture the main characteristics of the cyclic stress-strain curves of the stainless steel rebar with different yield stresses in tension and in compression.

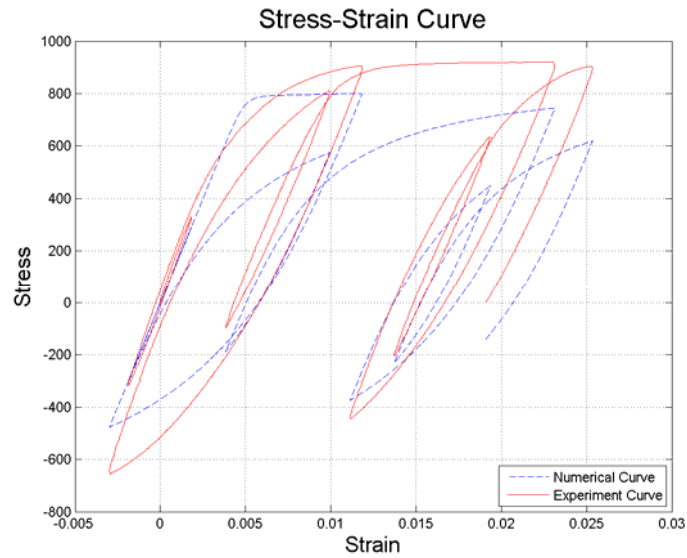


Figure 3.5 Comparison between experimental curve and numerical curve generated by original Monti-Nuti model (Stainless steel rebar, XA1, L/D=5)

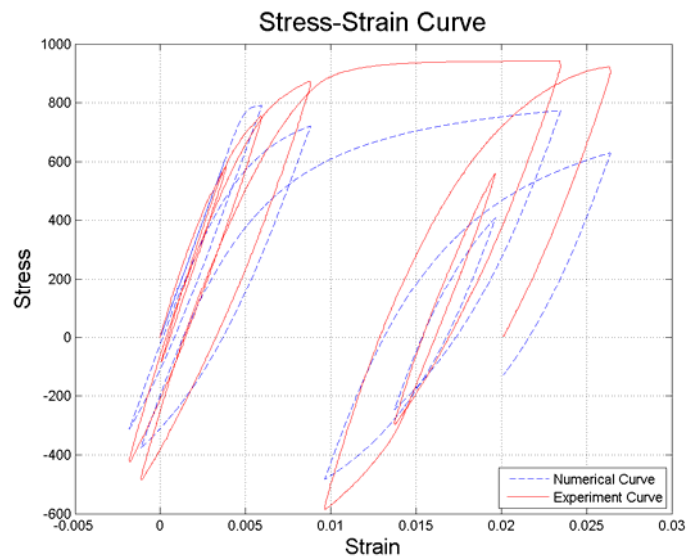


Figure 3.6 Comparison between experimental curve and numerical curve generated by original Monti-Nuti model (Stainless steel rebar, XA2, L/D=5)

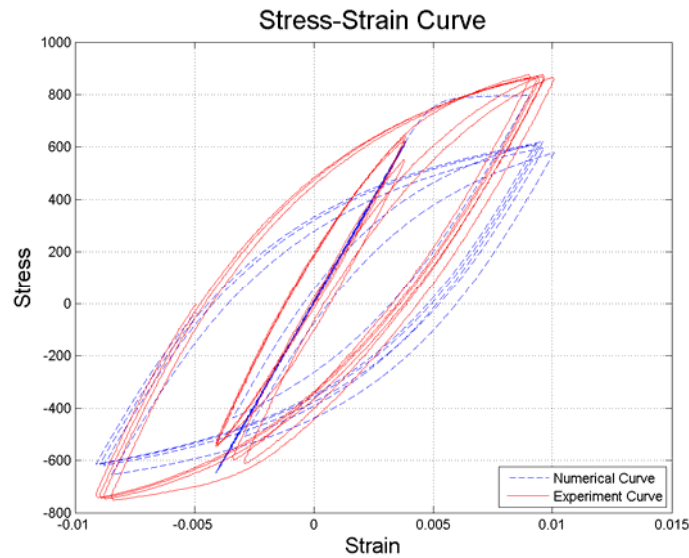


Figure 3.7 Comparison between experimental curve and numerical curve generated by original Monti-Nuti model (Stainless steel rebar, XA3, $L/D=5$)

Figure 3.8, Figure 3.9 and Figure 3.10 illustrate the comparisons between the numerical curves generated by the original Monti-Nuti model and the experimental curves of stainless steel rebar with slenderness L/D equal to 11.

The comparisons between the numerical curves generated by the original Monti-Nuti model and the experimental curves indicate the original Monti-Nuti model needs be improved to incorporate the effect of anisotropy on the cyclic behaviors.

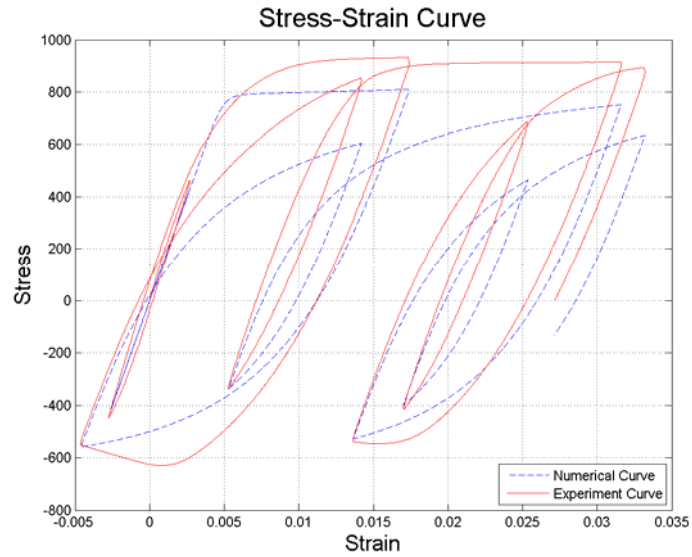


Figure 3.8 Comparison between experimental curve and numerical curve generated by original Monti-Nuti model (Stainless steel rebar, XC1, L/D=11)

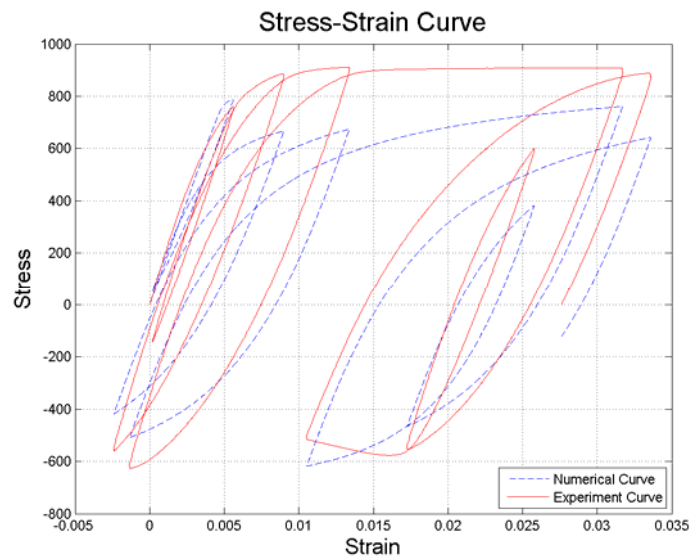


Figure 3.9 Comparison between experimental curve and numerical curve generated by original Monti-Nuti model (Stainless steel rebar, XC2, L/D=11)

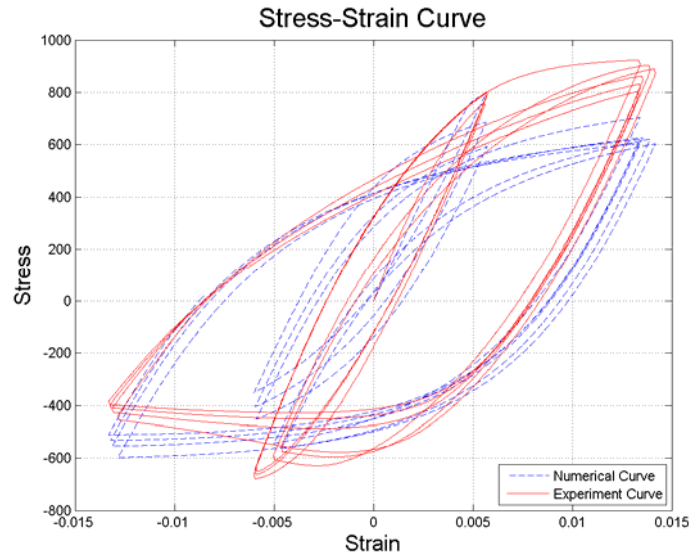


Figure 3.10 Comparison between experimental curve and numerical curve generated by original Monti-Nuti model (Stainless steel rebar, XC3, L/D=11)

The effects of the yield strength and the anisotropy are fully studied in the following section and the original Monti-Nuti is improved to be applicable for different types of steel reinforcing bars.

3.1 EFFECT OF YIELD STRESS ON CRITICAL SLENDERNESS

According to the experiments on the carbon steel reinforcement with yield stress equal to 450 MPa, Monti and Nuti (1992) suggested that the critical slenderness ratio (the length between two subsequent transversal rebars divided by diameter of the reinforcing bar) is 5 when buckling could emerge. Mau and El - Mabsout (1989) pointed out that the critical slenderness is 6, above which the buckling of the reinforcement will occur. Dhakal and Maekawa (2002a) demonstrated that both the yield strength and the slenderness have effect on the critical slenderness and proved that the combined parameter $L/D\sqrt{f_y}$ determines the cyclic behaviors. Through a series of numerical experiments, it is illustrated that the rebars

with different slenderness ratios L/D and different yield strengths could generate the identical cyclic stress-strain curves if the combined parameters $L/D\sqrt{f_y}$ of different reinforcing bars are equal.

3.1.1 Fiber Model Adopted in Microanalysis of Bare Bar

In order to study the effect of yield stress on the effect of stress-strain relationship of the rebar, the fiber model is built to simulate the behavior of one bare rebar. As shown in Figure 3.11, the rebar is divided into segments along its axial length, and each segment is simulated by one finite element. At each end cross section, the finite element is divided into sub-elements named as fibers. The strain of each fiber is calculated based on the Euler-Kirchoff's hypothesis that plane section remains plane after bending. The corresponding stress of each fiber is calculated according to the constitutive material model. Then the response of the cross section of the element is calculated by integral the stress of the fibers (Patxi Uriz, 2008).

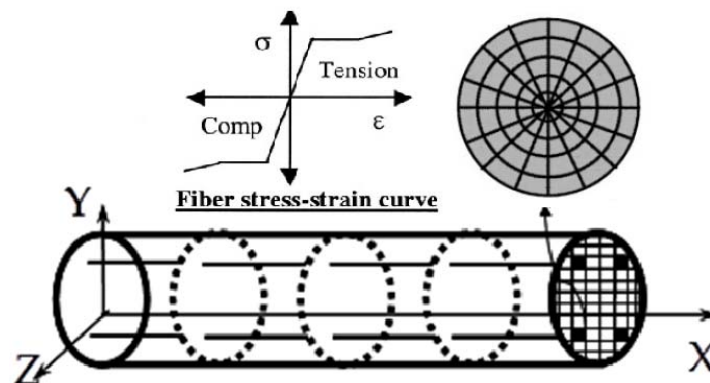


Figure 3.11 Fiber technique in simulating the bare rebar

(P. Uriz, Filippou, & Mahin, 2008) proposed the method to simulate the inelastic buckling of the brace with slenderness larger than 60. Initial imperfection is applied in the middle of the brace to induce and capture the inelastic buckling of brace. Adopting the force-based element and steel material model without buckling, here one fiber model is built to simulate the monotonic and cyclic behavior of rebar with slenderness no

larger than 20. In order to capture the characteristics of the behaviors of rebar including buckling, the precise fiber model should be built properly. Thus the parameters study of the fiber model is made, including effect of initial imperfection on buckling, number of elements, number of Integration Points of the element, and meshing at the cross section of element.

1. Geometry nonlinearity

According to the experiments carried out by Monti and Nuti (1992), when its slenderness exceeds 5, obvious lateral deformation will emerge at the middle of the rebar if the corresponding stress of the rebar is over the yield stress. In order to capture the buckling of the rebar in the fiber model, the initial imperfection should be adopted at the middle of the rebar.

As shown in Figure 3.12, the slenderness L/D of the rebar equals 5, 8 and 11, same to the slenderness of the carbon steel rebar tested by Monti and Nuti (1992). If initial imperfection is not applied at the middle of the rebar, the stress-strain curves of rebars with different slenderness are identical and no buckling could be observed. If the initial camber is considered, the stress-strain curve of rebar with slenderness $L/D=5$ coincides with the curve of the rebar without initial camber; while the curves of rebar with slenderness L/D equal to 8 and 11 will diverge from the curves without initial imperfection and buckle after reaching the yield point.

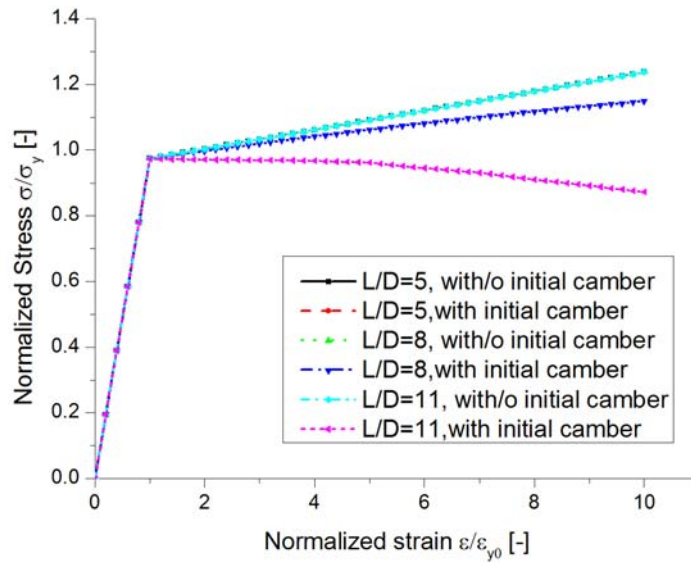
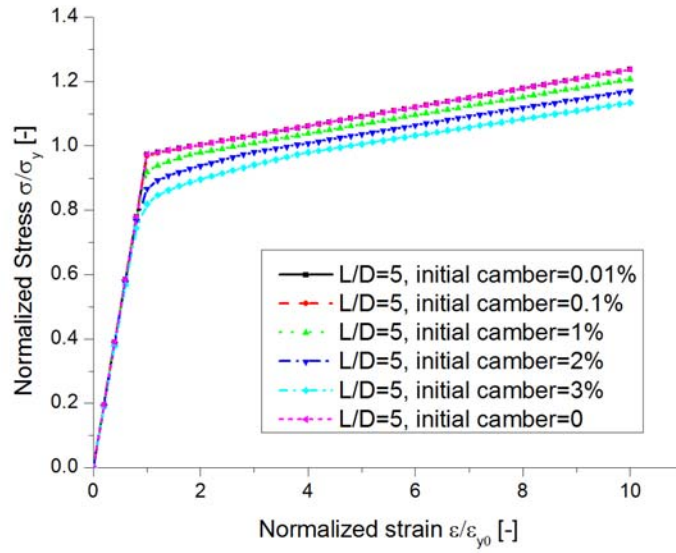


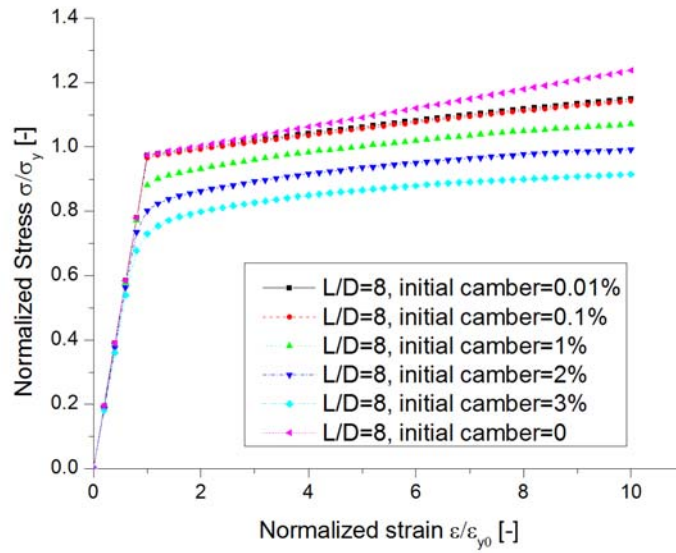
Figure 3.12 Comparisons between monotonic compressive curves of rebar generated by fiber model with or without initial imperfection

2. Effect of Initial Imperfection

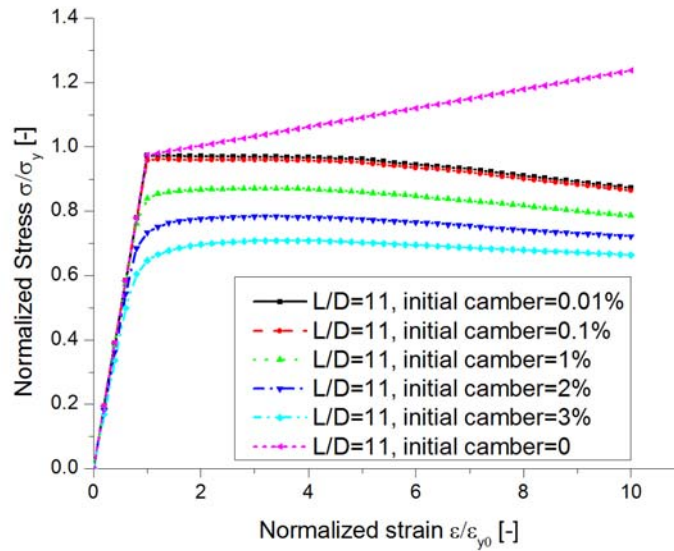
In Figure 3.13, the sensitivity of the initial camber of the fiber model is illustrated. In Figure 3.13 a), for the curves of rebar with $L/D=5$, when the initial camber equals 0.01% or 0.1% of the length of rebar, the curves coincide with the curve without initial buckling. However, if the initial is larger than 1%, buckling emerges before yield stress, which means that the initial camber is so large that the induced second order moment is too big. In Figure 3.13 b) and Figure 3.13 c), similar conclusions could be obtained, thus the initial camber is set as 0.01% of the length of the rebar. Another conclusion could be drawn that the rebar with L/D equal to 5 doesn't buckle, while buckling emerges in the curves of the rebar with L/D equal to 8 and 11. This conforms with the observations from the experiment (Giorgio Monti & Nuti, 1992).



a) $L/D=5$



b) $L/D=8$



c) $L/D = 11$

Figure 3.13 Comparisons between the monotonic curves of rebar with different slenderness (L/D) generated by fiber model with different initial imperfections

3. Number of elements

Figure 3.14 demonstrates the sensitivity analysis of the number of elements used for one bare rebar. It could be concluded that 2 elements could simulate the behavior of the rebar precisely.

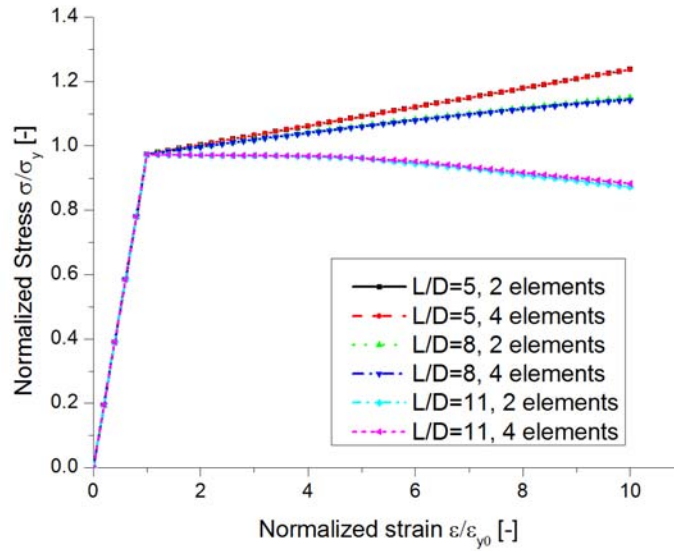
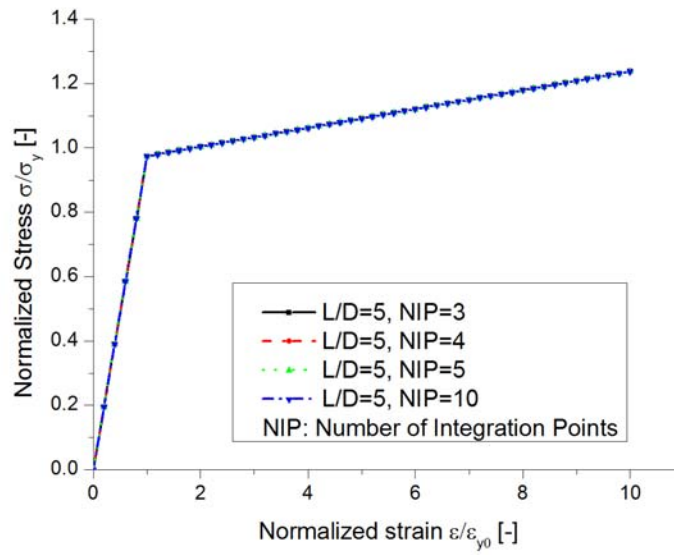


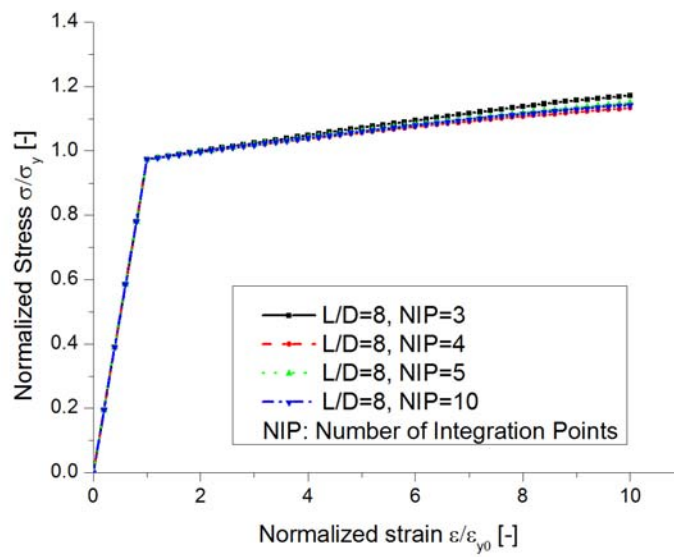
Figure 3.14 Comparisons between monotonic curves of rebar with different slendernesses generated by fiber model using different numbers of elements

4. Effect of Number of Integration Points

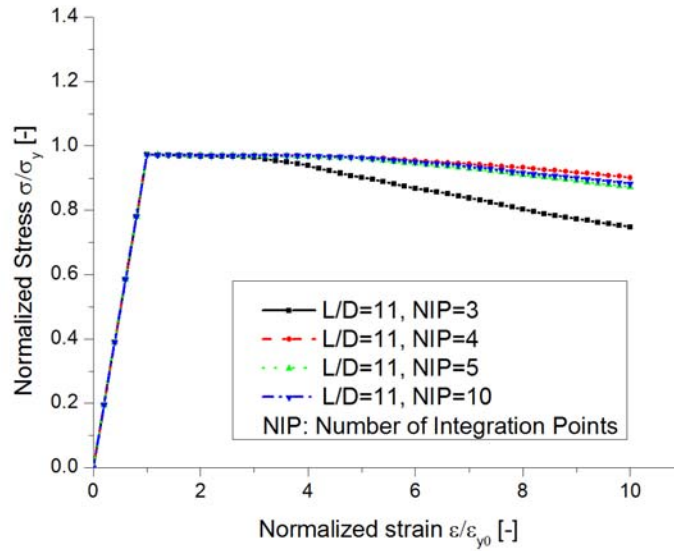
For the force-based element, to increase the number of integration points (NIP) in the element could improve the computational accuracy but doesn't make computation more expensive. In Figure 3.15, the sensitivity of NIP is illustrated for the rebar with different slenderness respectively. The minimum number of integration points should be two and the limitation of the maximum NIP for each element is 10 (Scott, 2011). From the comparisons, it is found that when NIP equals 5, computational accuracy could be guaranteed.



a) $L/D=5$



b) $L/D=8$

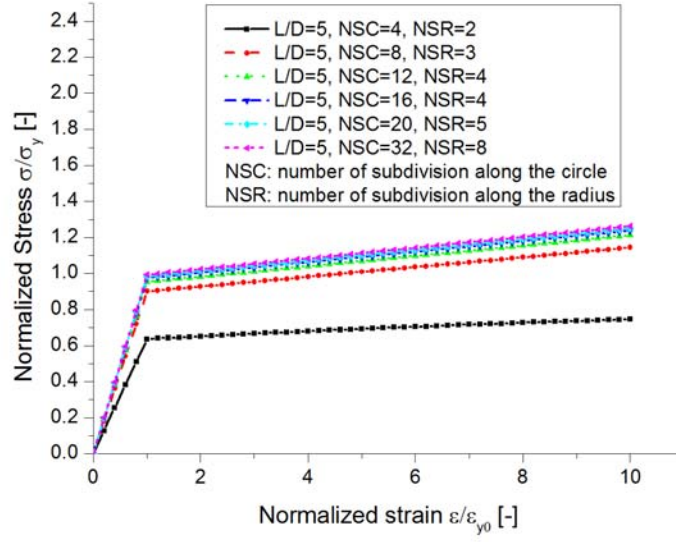
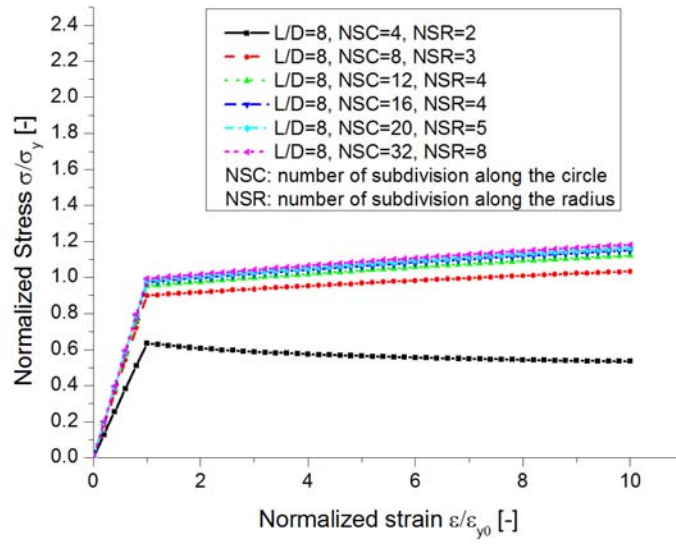


c) $L/D=11$

Figure 3.15 Comparisons between monotonic curves of rebar with different slendernesses generated by fiber model using different numbers of Integration Points for each element

5. Meshing of cross section

The cross section is divided along the circle and along the radius. The sensitivity analysis is made for the rebar with different slenderness respectively. From Figure 3.16, when the subdivision along the circle equals 16 and the subdivision along the radius equals 4, satisfactory computational accuracy is obtained for the reinforcing bar with different slenderness.

a) $L/D=5$ b) $L/D=8$

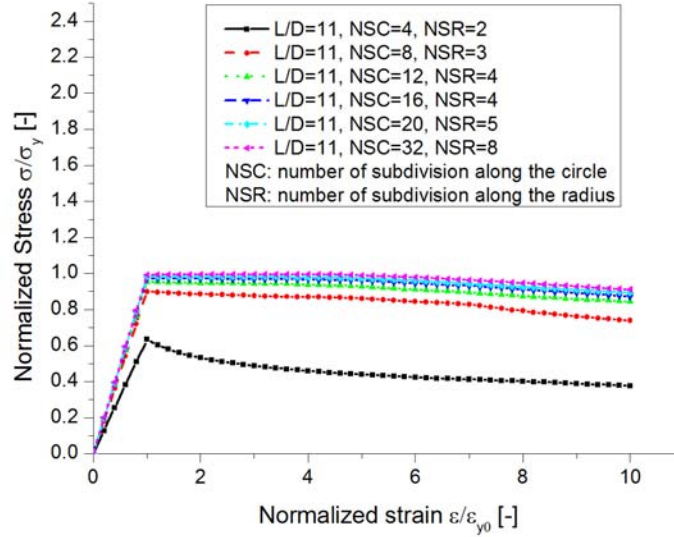
c) $L/D=11$

Figure 3.16 Comparisons between monotonic curves of rebar with different slendernesses generated by fiber model adopting different numbers of subdivisions along the circle and the radius for cross section meshing

Through the above parameter study and sensitivity analysis, the parameter of the fiber could be determined and shown in Table 3.3.

Table 3.3 Selection of Parameters for Fiber Model

Model parameters	Values
Number of elements	2
Initial imperfection	0.01%
NIP	5
Cross section meshing	NSC=16, NSR=4

Note: NIP is short for number of integration points for each element;
NSC is the number of subdivisions along the circle of the cross section;
NSR is the number of subdivisions along the radius of the cross section.

3.1.2 Verification of the Fiber Model

After the parameters in the fiber model are determined, the experiments on carbon steel rebar with slenderness L/D equal to 5, 8, 11 and diameters equal 16, 20, and 24mm (Giorgio Monti & Nuti, 1992) are simulated and the comparisons between the numerical curves and the experimental curves of the rebar under monotonic compression are illustrated in Figure 3.17. The fiber model could simulate the monotonic behaviors quite well.

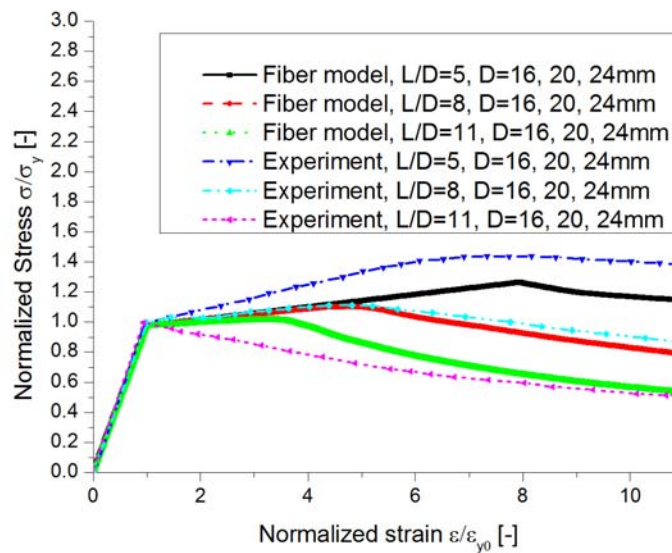


Figure 3.17 Verification of the fiber model with monotonic compressive experimental curves with different slendernesses

Then the cyclic tests of the rebar are simulated by the fiber model. The geometric and mechanical properties of the specimen are shown in Table 3.4.

Table 3.4 Geometric and Mechanical properties of bare rebar

Load case	L [mm]	D [mm]	F_y [MPa]	E [MPa]	b [-]
A1	80	16	470	200000	0.03
C1	176	16	470	200000	0.03

The cyclic stress-strain behaviors of the rebar are path-dependent, thus the cyclic material model “Steel02” in OpenSees is adopted. The material model “Steel02” is developed based on the Menegotto-Pinto model improved by Filippou et al. (1983) introducing the isotropic hardening rule. This material model could not simulate precisely the cyclic behavior of the rebar in presence of buckling; however the buckling behavior could be captured by the fiber model adopting initial imperfection. The parameters of “Steel02” used in the fiber model in absence of buckling and in presence of buckling are listed respectively in Table 3.5.

Table 3.5 Parameters values of “Steel02” adopted in the fiber model

Load case	R0	CR1	CR2	a1	a2	a3	a4	sigInit
A1	20	0.925	0.15	0.05	1	0	1	0
C1	20	0.925	0.15	0.03	1	0	1	0

The loading histories for two test cases are identical and illustrated in Figure 3.18.

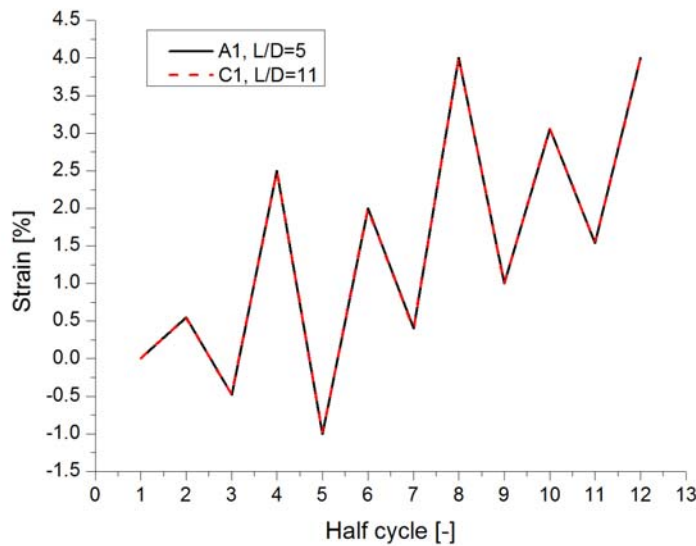
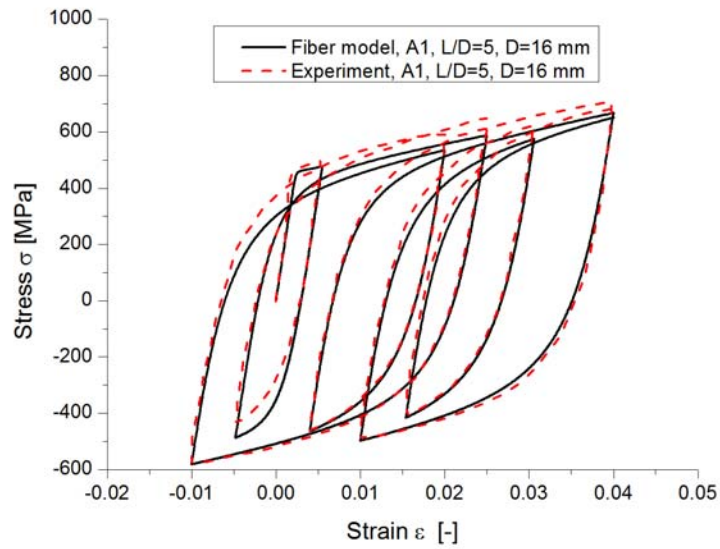
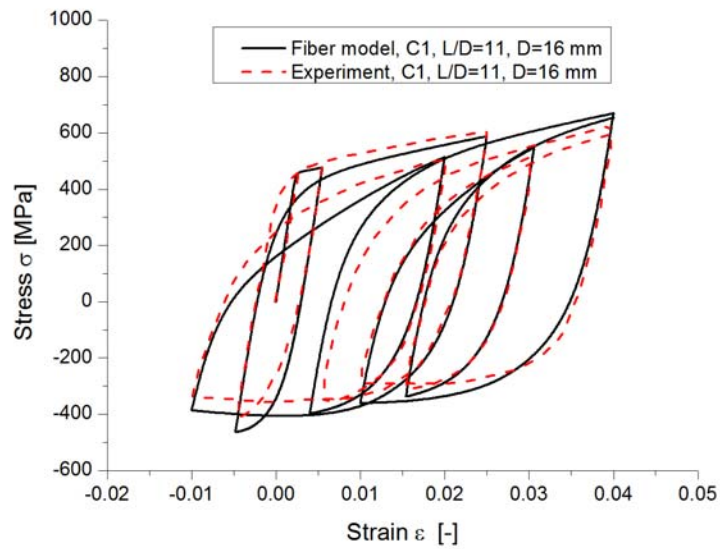


Figure 3.18 Loading strain histories of cyclic test A1 and C1



a) $L/D=5$, in absence of buckling



b) $L/D=11$, in presence of buckling

Figure 3.19 Verification of the fiber model with the experimental cyclic stress-strain curves of rebar with different slendernesses

In Figure 3.19, the comparisons between the numerical curves generated by the fiber model and the experimental curves are illustrated. The numerical curve could coincide with the experimental results very well. Hereby, the effectiveness of the fiber model is verified for the rebar under monotonic loading and cyclic loading in absence of buckling and in presence of buckling.

3.1.3 Combined Factor Affecting Critical Slenderness

In order to verify the effect of yield stress on the behavior of the rebar, a series of tests adopting the fiber model are built for the rebar with different slenderness and yield stresses, and the details are listed in Table 3.6.

Table 3.6 Combined parameter for different rebars

L/D	F_y [MPa]	$L/D\sqrt{F_y/450}$
5	112.5	5/2
	225	$5\sqrt{2}/2$
	450	5
	900	$5\sqrt{2}$
	1800	10
10	112.5	5
	225	$5\sqrt{2}/2$
	450	10
	900	$10\sqrt{2}$
	1800	20

In Figure 3.20, the stress-strain curves could coincide with each other quite well if the combined parameters $L/D\sqrt{F_y/450}$ are equal. This combined parameter could be named as computational slenderness which incorporates the effect of yield stress on the critical slenderness.

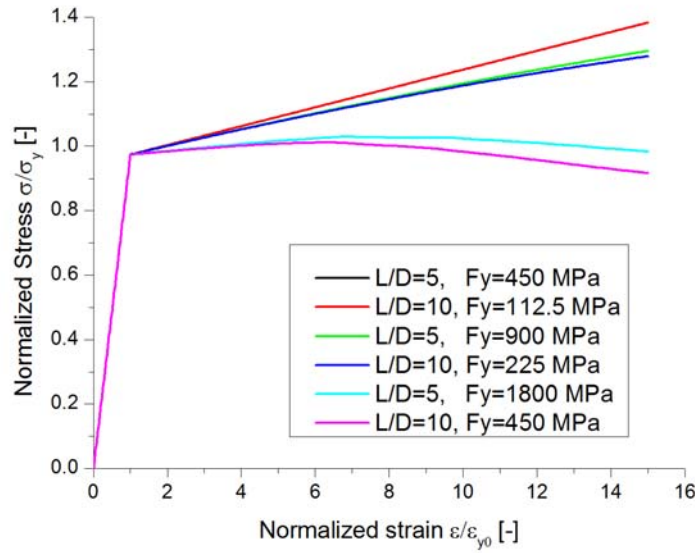


Figure 3.20 Effect of yield stress on the stress-strain curves of rebar with different slenderness and yield stress generated by fiber model

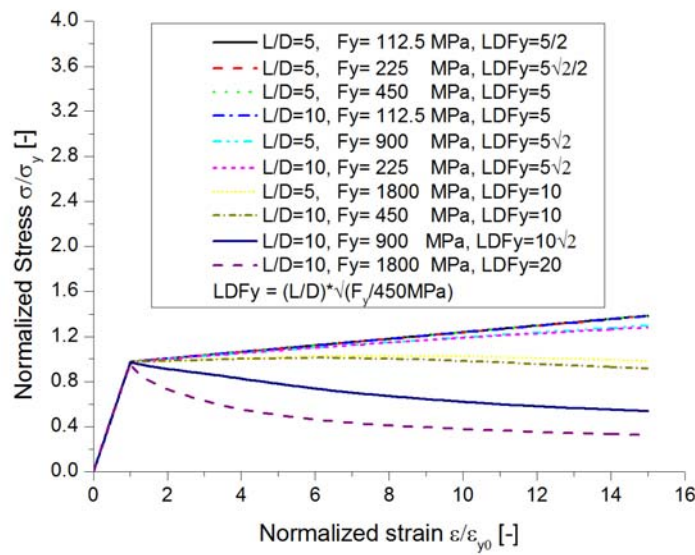


Figure 3.21 Monotonic stress-strain curves of rebar with different combined parameters generated by fiber model

In Figure 3.21, the stress-strain curves of the rebars with different computational slenderness are illustrated. The curves of rebar will be identical when the computational slenderness equal. And the buckling of the rebar will be more obvious if its computational slenderness is larger.

Monti and Nuti (1992) pointed out the critical slenderness is 5 when buckling emerges, based on the experimental observation of the carbon steel rebar Feb44, with yield stress equal to 450 MPa. Given the computational slenderness obtained from the fibre model simulation, the critical slenderness is affected by one parameter named as critical slenderness coefficient β , defined in Eq. (3.1).

$$\beta = \frac{f_{yc}}{f_y} \quad (3.1)$$

where f_{yc} is the yield stress of the material in compression, and f_y is the base yield stress, equaling 450 MPa.

Thus the critical slenderness could be defined in Eq. (3.2).

$$\lambda_{cr} = 5/\sqrt{\beta} \quad (3.2)$$

For the carbon steel rebar with yield stress 450 MPa, the critical slenderness remains 5. It could be concluded that the greater the yield strength, the smaller the critical slenderness ratio L/D when the buckling turns up.

Zong (2010) who built three dimensional finite element model of individual reinforcing bar and verified that identical stress-strain curves could be obtained for the same value of the combined parameter $\sqrt{f_y/420}(L/D)$ where 420 representing the average yield stress of commonly used steel rebar in structure and the unit is MPa.

3.2 ANISOTROPY OF STEEL REBAR

For the stainless steel reinforcing bar produced according to earlier production specifications, the yield stresses in tension and in compression are different, and this phenomenon is named as anisotropy of stainless steel.

The tested stainless steel rebars specimens AISI304 or 1.4301 are provided by Valbruna Italy. The test machine is MTS 810 operating under displacement control, and the loads were applied axially with four strain gauges along the specimen. The tests were conducted at ambient temperature, with the increment of load at 60Mpa/s, or at equivalent deformation 0.044mm/s. Displacements were obtained by transducers placed on the rebars. Thus a series of load-displacement curves were obtained. The machine and the tested specimen were shown in Figure 3.22.

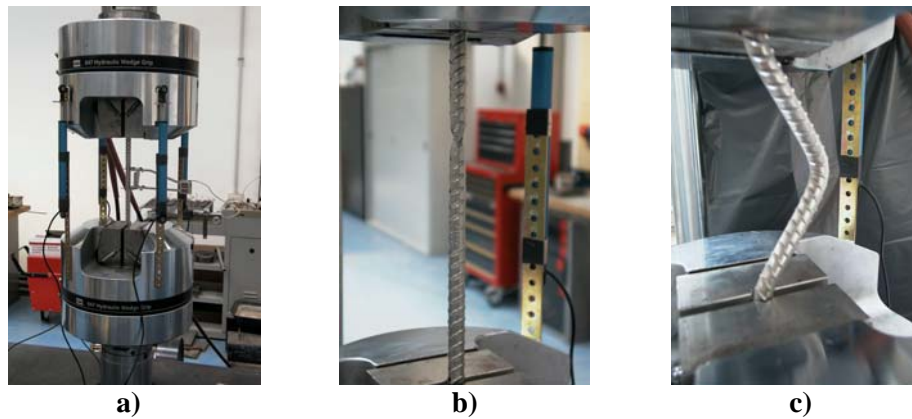


Figure 3.22 Testing machine and the specimen: a) Test machine MTS 810; b) specimen in tension; c) specimen in compression

The slenderness ratio of the specimen equals 5 and 11; and the monotonic tensile and compressive curves are demonstrated in Figure 3.4. It could be observed that the yield stress in tension is around 790 MPa, but the yield stress in compression is 680 MPa.

Several different monotonic tensile material models for stainless steels have been set up based on Ramberg-Osgood model improved by Hill. The behaviors of stainless steel in tension and compression are unsymmetrical, named as anisotropic, which is quite different from the carbon steel. Consequently, several material models are developed to describe the stainless steel stress-strain behavior. Romberg-Osgood stress-strain relationship, which is improved by Hill (1944), is mostly used to describe the stainless steel. This model could simulate the stress-strain relationship accurately up to $\sigma_{0.2}$ but fails at higher stress.

Rasmussen (2003) and Gardner and Nethercot (2004) respectively propose new expressions to predict the stress-strain relationship when the stress exceeds $\sigma_{0.2}$.

Quach, Teng, and Chung (2008) points out that Rasmussen Model succeeds in simulating accurately the behavior of stainless steel in tension but fails in compression. The Gardner-Nethercot Model could predict the stress-strain relationship both in tension and compression, but fails when the stress exceeds $\sigma_{2.0}$. Consequently, one three-stage stress-strain model is proposed by Quach et al. (2008).

In order to improve the versatility of the model for reinforcing bar with different yield stresses in tension and in compression which is different from the original carbon steel rebar, the parameter named as anisotropy coefficient α (Zhou, Nuti, & Lavorato, 2014), is defined in Eq. (3.3).

$$\alpha = \frac{f_{yt}}{f_{yc}} \quad (3.3)$$

where f_{yt} is the yield strength of stainless steel rebar in tension, and f_{yc} is the yield strength in compression.

For the stainless steel with different yield stresses in tension and in compression, the critical slenderness should depend on the yield stress in compression because the buckling of reinforcement emerges under compressive load. Thus, the combined parameter should be modified as $L/D\sqrt{f_{yc}}$, where f_{yc} is the yield stress of the reinforcement in compression.

3.3 MODIFIED MONTI-NUTI MODEL

To make the original Monti-Nuti model applicable in general cases, the effects of different yield stress and anisotropy on the model should be considered to improve the model (Zhou, Nuti, & Lavorato, 2015a).

3.3.1 Effect of the Yield Strength

The different yield strengths result in the variation of the slenderness ratio $(L/D)_{cr}$, which is a critical parameter to decide whether considering the buckling or not when the yield strength at the reversal point of each half cycle is updated. The original critical slenderness ratio $(L/D)_{cr}$ is 5, and hereby should be revised according to Eq. (3.4):

$$\lambda_{cr} = (L/D)_{cr} = 5\sqrt{450/f_y} \quad (3.4)$$

where f_y is the yield stress of the reinforcing bar.

The critical slenderness varies according to the yield stress, thus it will result in the variation of the superposition length γ_s .

$$\gamma_s = \frac{11 - L/D\sqrt{\beta}}{e^{c(L/D\sqrt{\beta}-5)} - 1} \geq 0 \quad \text{for } 5 < L/D\sqrt{\beta} \leq 11 \quad (3.5)$$

c is related to the rebar and is set as 0.5 in the original test. The value of γ_s is normalized by the strain corresponding to the yield stress. The real superposition length γ_s^* is defined in Eq. (3.6).

$$\gamma_s^* = \gamma_s \frac{f_y}{E_0} \quad (3.6)$$

The lower bound for the curve transition parameter is determined by the critical slenderness λ_{cr} , thus the lower bound is redefined as:

$$R_1^b = 10[L/D - \lambda_{cr}]b^+, \quad \lambda_{cr} = 5/\sqrt{\beta} \quad (3.7)$$

3.3.2 Effect of the Anisotropy

The anisotropy of the reinforcing bar results in different curve transitions in tension and in compression. Thus the parameters in the formula related to R were redefined. The values of parameters R_0 , A_1 and A_2 are defined by Eqs. (3.8-3.12), considering the effects of anisotropy and the yield

strength. The anisotropy is depicted by two parameters: anisotropy coefficient α , critical slenderness coefficient β .

The formula for R in the original model is modified in Eq. (3.8):

$$R = \begin{cases} R_0 - \frac{A_1^t \xi_{max}}{A_2^t + \xi_{max}}, & \text{in tensile branch} \\ R_0 - \frac{A_1^c \xi_{max}}{A_2^c + \xi_{max}}, & \text{in compressive branch} \end{cases} \quad (3.8)$$

where R_0 is the initial value of R , defined in Eq. (3.9); A_1^t , A_2^t are the coefficients under tensile loading defined in Eq. (3.11) and A_1^c , A_2^c are the coefficients under compressive loading defined in Eq. (3.12), which are related to the mechanical properties of reinforcing bar; in presence of buckling R_1^b is the lower bound, thus $R \geq R_1^b$, is defined in Eq. (3.13).

$$R_0 = \begin{cases} r_t R_0^1 & (\text{in tension}) \\ r_c R_0^1 & (\text{in compression}) \end{cases} \quad (3.9)$$

where r_t and r_c are the coefficients to calculate the initial value of R_0 for the tensile curve and compressive curve respectively, and are defined by the anisotropy coefficient α and the critical slenderness coefficient β in Eq. (3.10).

$$r_t = \frac{\alpha\beta}{2}, \quad r_c = \frac{r_t}{\alpha} = \frac{\alpha\beta}{2\alpha} \quad (3.10)$$

A_1^t and A_2^t are the parameters to update the curve transition parameter R at each reversal in tension, defined in Eq. (3.11).

$$A_1^t = \frac{1}{100} [\lambda_c (\alpha\beta)^2 (\lambda - \lambda_c)] + \alpha, \quad A_2^t = -\frac{8\alpha\beta}{10^4} (\lambda - 4\lambda_c) \quad (3.11)$$

Where α is the anisotropy coefficient, β is the critical slenderness coefficient, λ is the slenderness of the rebar, and λ_c is the critical slenderness of the rebar.

A_1^c and A_2^c are defined in Eq. (3.12) to update the curve transition parameter R at each reversal in compression

$$A_1^c = \alpha A_1^t, A_2^c = \frac{6\beta}{10^3}(\lambda - 2\beta) \quad (3.12)$$

Where α is the anisotropy coefficient, defined in Eq. (3.3), A_1^t is the parameter to update the curve transition parameter R at each reversal in tension, defined in Eq. (3.8), and β is the critical slenderness coefficient, calculated in Eq. (3.1).

$$R_1^b = 10[L/D - \lambda_{cr}]b^+ \quad (3.13)$$

3.4 ADDITIONAL CRITERIA FOR UPDATE THE MODEL PARAMETERS

Under seismic action, the rebar in the reinforced concrete structures could suffer very complicated partial unloading and reloading strain histories. In this case, the Menegotto-Pinto model could overestimate the corresponding stress of the rebar, as in the original Menegotto-Pinto model, two straight lines are adopted as the envelope lines and the stress-strain curve is controlled by the two envelopes and the curve transition parameter R . In general, the parameters such as the elastic modulus at the origin (or the reversal), the new intersection between the two envelopes, the hardening ratio b , the curve transition parameter R are updated. However, if the reversal doesn't exceed the strain corresponding to the intersection of previous branch, the Menegotto-Pinto model will overestimate the stress.

In order to solve the above phenomenon of Menegotto-Pinto model, several researchers proposed different solutions.

3.4.1 Discussion of the Proposed Solutions to Address the Above Issues

Filippou et al. (1983) pointed out that the new partial reloading curve should follow the previous loading branch once it reaches the previous loading branch (curve (a) in Figure 3.23). However, to achieve this aim, it requires the model to store all necessary information, such as the origin,

reversal, intersection, elastic modulus at origin and tangent modulus at target and curvature parameter R , to retrace all previous reloading curves. This will increase the memory cost and reduce the computational efficiency.

To simplify the solution, only four controlling curves besides the current branch need be memorized:

- 1) The monotonic tensile skeleton curve;
- 2) The monotonic compressive skeleton curve;
- 3) The ascending up branch originating at the reversal with the smallest strain value;
- 4) The descending lower branch originating at the reversal with the largest strain value.

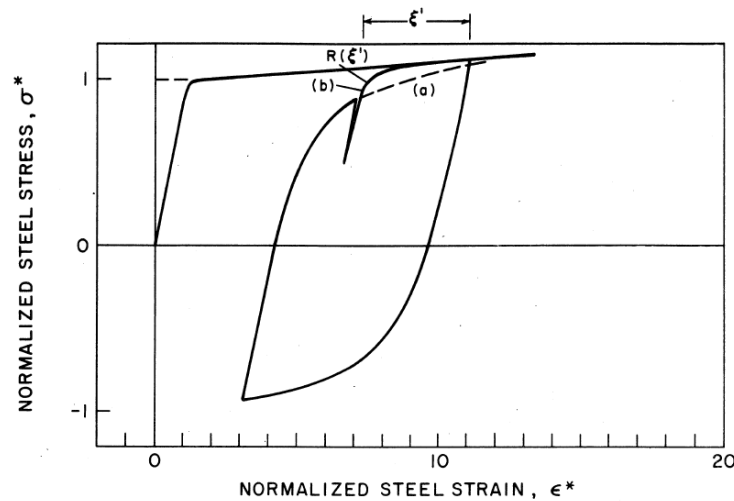
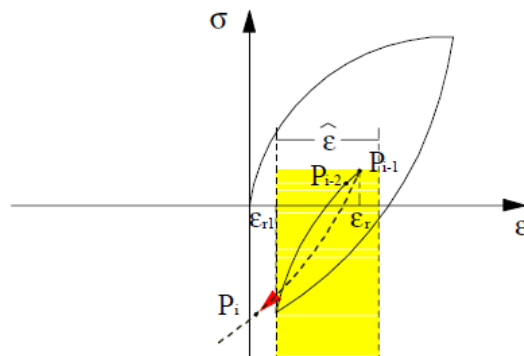


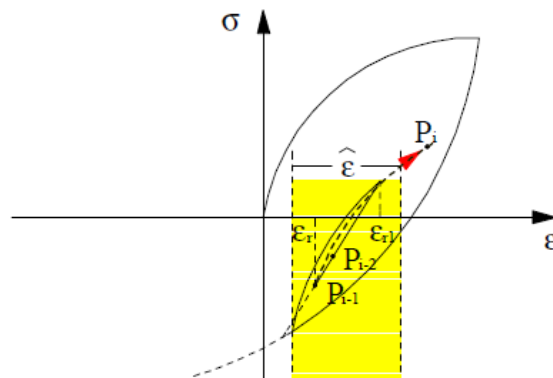
Figure 3.23 Update curvature parameter $R(\xi)$ in the case of partial unloading and reloading

Adopting the aforementioned solution, the reloading branch (in Figure 3.23) will follow branch (b) instead of branch (a). The proposed solution joints tangently the new partial reloading branch to the controlling branch memorized. But the criteria to define the partial unloading and reloading is not given. Furthermore, if the strain distance between two consecutive partial unloading and reloading reversal is too small, the transition from the current strain step to the controlling line should be elastic.

Attolico, Biondi, Nuti, and Petrangeli (2000) proposed another solution for the Monti-Nuti model combining with the Menegotto-Pinto model to eliminate the overestimation problem in the case of partial unloading and reloading. The new unloading curve joints tangently to the previous unloading branch which update all parameters, if the reversal does exist inside the small interval specified as $\hat{\varepsilon}$, shown in Figure 3.24 a); the unloading or reloading will be linear elastic if the previous reversal also exists inside the loops, shown in Figure 3.24 b). The expression for $\hat{\varepsilon}$ is not given by the authors, but it could be defined based on the maximum plastic excursion of previous branches.



a) tangently joint to the previous branch



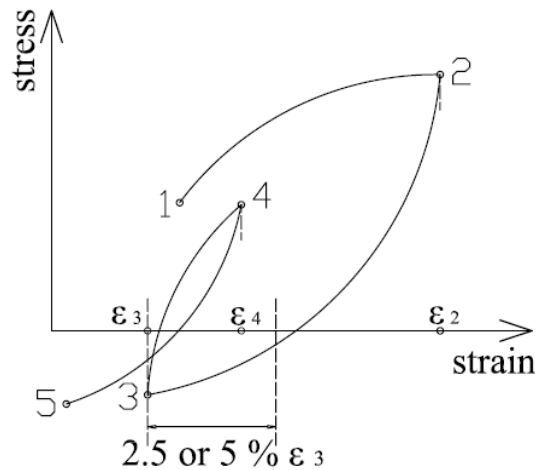
b) linear elastic stress-strain relationship inside the small interval

Figure 3.24 Solution to eliminate the overestimation under partial unloading and reloading (Attolico et al., 2000)

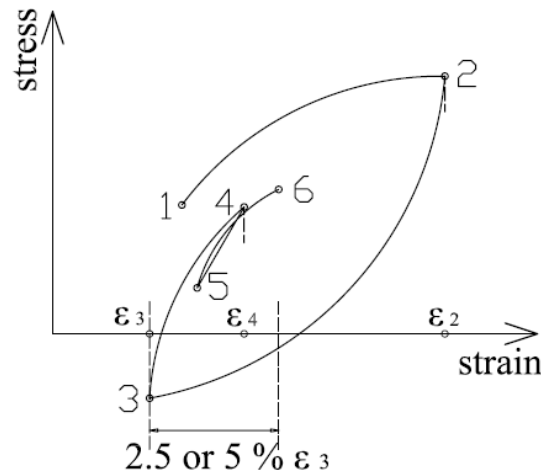
This solution calculates the corresponding stress at each strain step using the Monti-Nuti model or simple line model depending on the position of the reversal. The criteria to judge partial unloading or reloading is that whether the reversal exceeds the interval $\hat{\epsilon}$.

Fragiadakis, Pinho, and Antoniou (2007) proposed another solution to update the Monti-Nuti model under partial unloading and reloading strain histories. The new branch is calculated based on the Monti-Nuti model or the straight line, depending on the position of the reversal and the status of the new branch.

In Figure 3.25 a), the origin (reversal, point 4) of the new branch exists in the interval based on the origin (point 3) of previous branch, thus the branch 3-4 is partial reloading branch; and then the new branch 4-5 exceeds this interval (point 5 is outside the interval), branch 4-5 joints tangently to the previous branch which update all the controlling parameters. In Figure 3.25 b), the origin of branch 4-5 existing the interval, and the reversal (point 5) of the following branch 5-6 still existing in the interval, thus branch 4-5 should be linear elastic. Then point 6 of the branch 5-6 exceeds the interval, joints branch 5-6 tangently to the previous branch 3-4 which updated all controlling parameters.



a) tangently joint to the previous branch



b) linear elastic unloading inside the interval

Figure 3.25 Solution to eliminate the overestimation under partial unloading and reloading

The solution needs to judge whether the new branch exists inside the interval or goes beyond the interval. That means it is necessary to know all the strain steps of the new branch at the reversal. It is not practical for the structural analysis, because it is impossible to know in advance the strain steps of the reinforcement in the structural element like reinforced concrete column or beam.

As for the fiber element method, shown in Figure 3.26, the cross section of the column is divided into fibers; then the strain of different fibers could be obtained by the fiber element. When the displacement at each step is applied into the fiber element, the strain step could be obtained for the fiber, and then the corresponding stress could be calculated based on the fiber material model. And then the force of the cross section could be calculated by integral. Hereby, it is impractical to judge the status of the new branch at the reversal.

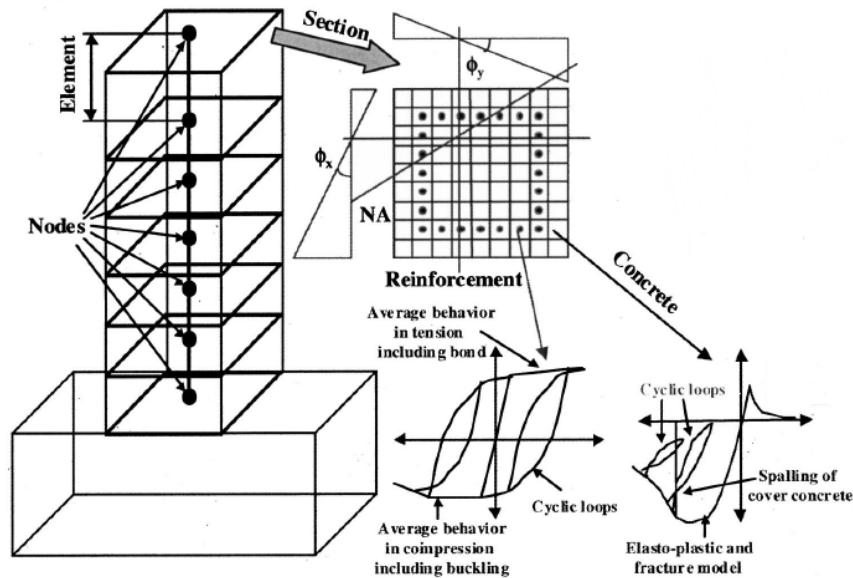


Figure 3.26 Fiber technique and applied in Finite Element Method (Dhakal & Maekawa, 2002c)

3.4.2 Proposed Criteria to Update the Model Parameters under Generalized Loading

As discussed above, the Menegotto-Pinto model is used to define the stress-strain relationship between two reversal; at the reversal, the Monti-Nuti model could update the controlling parameters, such as intersection, hardening ratio b , curve transition parameter R . However, if the model is applied under generalized loading, the criteria to apply the Monti-Nuti model to update the controlling parameters should be defined to avoid overestimation of the stress.

The model is path-dependent, thus how to update the controlling parameter at the reversal depends on the status of previous branch. There are three statuses for the previous branch: full parameters are updated, partial parameters are updated, no parameters are updated. Accordingly, it is necessary to define the criterion to judge different cases of unloading and reloading branches.

For each status of the previous branch, three important aspects need be considered at the reversal which is the critical point between two consecutive branches. There are twelve possible conditions for the previous branch, all the possible conditions are listed in Table 3.7. To be clear, the start point of one branch is named as origin, and the end of the branch is called target point.

Table 3.7 Possible conditions of the previous branch

Properties of the previous branch	Position of target point	Loading direction	Whether buckle
	Plastic;	Unloading	In absence of
	Elastic;	(UL);	buckling (AB);
	Small	Reloading	In presence of
		(RL)	buckling (PB)
Different cases	3	2	2

The position of the target point is critical to determine the strategy for the new branch. The position of the target point could be classified as: plastic, elastic and small, which depends on the intersection of the branch and the previous branch.

As shown in Figure 3.27, the target point 2 exceeds the intersection 1, thus point 2 is plastic; target point 4 doesn't exceed the intersection 3, and the absolute stress difference between target point 4 and origin point 2 is smaller than the difference of previous branch between target point 2 and origin point 1, thus position of point 4 is small; target point 7 doesn't exceed intersection point 6, but the absolute stress difference between target point 7 and origin point 5 is larger than the difference between target point 5 and origin point 1 in previous branch which update the controlling parameters, thus the position of point 7 is elastic.

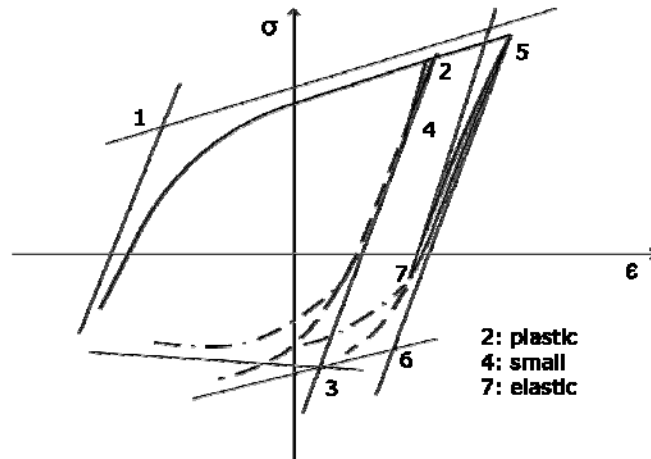


Figure 3.27 Different types of positions of reversal

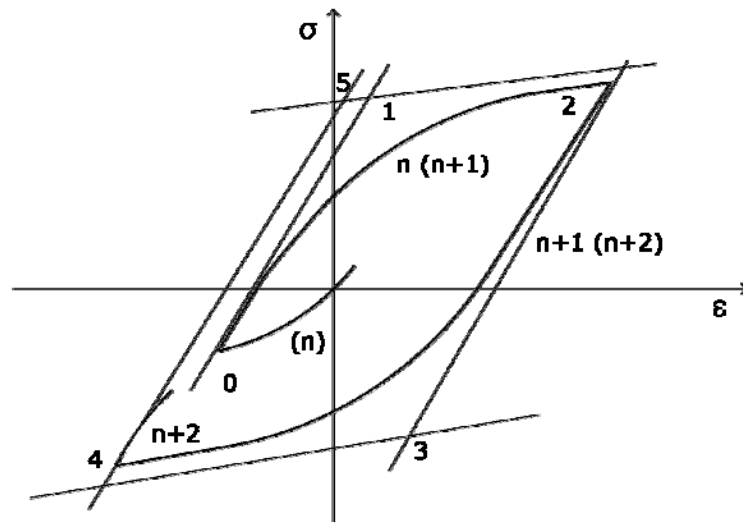
Then the strategies are defined for updating the parameters in the new branch at the reversal. Three reasonable strategies are enough to deal with different cases, named as fully update (FU), partially update (PU) and non update (NU). The strategies are listed in Table 3.8.

Table 3.8 Strategy for model update at reversal

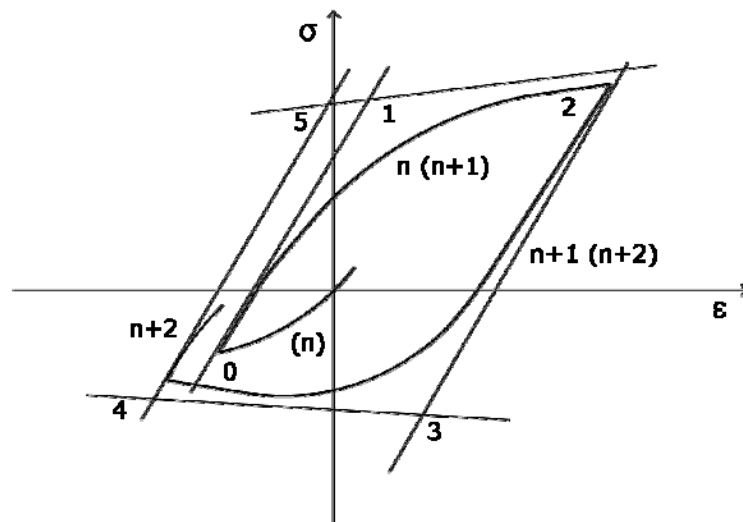
Figures	Status of previous branch			Update Strategy	Cases
	Reversal	Loading	Buckling		
Figure 3.28 a)	Plastic	UL RL	AB	FU	2
Figure 3.28 b)	Plastic	UL RL	PB	FU	2
Figure 3.29	Elastic	UL	AB PB	PU	2
Figure 3.30	Elastic	RL	AB	PU	1
Figure 3.31	Elastic	RL	PB	PU	1
Figure 3.32	Small	UL	AB PB	NU	2
Figure 3.33	Small	RL	AB	NU	1
Figure 3.34	Small	RL	PB	NU	1

UL: unloading, RL: reloading, AB: in absence of buckling, PB: in presence of buckling; FU: fully update, PU: partially update, NU: non update.

The criteria to judge the position of target point and the application of strategies in different cases are given below.



a) In absence of buckling (AB)



b) In presence of buckling (PB)

Figure 3.28 Status of branch $n+1$: Plastic, UL/RL, AB/PB;

Update strategy: Fully update

At the reversal, the new branch to update is named as branch $n+2$, the previous branch is called branch $n+1$, and the previous branch with the same loading or unloading direction to the new branch is called branch n . In Figure 3.28 a), in absence of buckling, unloading branch $n+1$ reverses at point 4, whose position is plastic, or the reloading branch $(n+1)$ reverses at the plastic point 2, thus the strategy to update branch $n+2$ or $(n+2)$ is to update all the controlling parameters. In branch $n+2$, the controlling parameters is expressed as: $\Theta_{n+2}(b, R, E, \varepsilon_r^{n+2}, \sigma_r^{n+2}, \varepsilon_y^{n+2}, \sigma_y^{n+2})$. The criteria to judge the status of branch $n+1$ is defined in expression (3.14).

$$\begin{cases} |\varepsilon_r^{n+2} - \varepsilon_r^{n+1}| > |\varepsilon_y^{n+1} - \varepsilon_r^{n+1}| \\ kon(n+1) = 1 \parallel kon(n+1) = -1 \\ flagBuckling = 0 \end{cases} \quad (3.14)$$

Where ε_r^{n+1} and ε_r^{n+2} are the strain at the origin of branch $n+1$ and $n+2$ respectively; ε_y^{n+1} is the yield strain corresponding to the intersection of branch $n+1$; $kon(n)$ is defined to mark the loading direction of the branch, 1 means reloading ascending upwards, and -1 stands for the unloading descending towards lower bound; $flagBuckling$ represents buckling could occur or not, if $flagBuckling(n)=0$, no buckling will emerge; otherwise, in presence of buckling, $flagBuckling(n)=1$.

In Figure 3.28 b), the condition that the unloading or reloading branch reverses from the plastic point in presence of buckling could be identified by expression (3.15).

$$\begin{cases} |\varepsilon_r^{n+2} - \varepsilon_r^{n+1}| > |\varepsilon_y^{n+1} - \varepsilon_r^{n+1}| \\ kon(n+1) = 1 \parallel kon(n+1) = -1 \\ flagBuckling = 1 \end{cases} \quad (3.15)$$

The strategies to update the controlling parameters of the model in the aforementioned four cases are identical. Thus the criterion to judge the four cases could be summarized in expression (3.16).

$$\left| \varepsilon_r^{n+2} - \varepsilon_r^{n+1} \right| > \left| \varepsilon_y^{n+1} - \varepsilon_r^{n+1} \right| \quad (3.16)$$

The steps to update the controlling parameters are shown below:

i) *update* $(\varepsilon_r^{n+2}, \sigma_r^{n+2})$

ii) *update* σ_y^{n+2}

iii) *update* b, R, E

iv) *update* ε_y^{n+2}

In Figure 3.29, unloading branch $n+1$ reverses at point 4 which doesn't exceed the intersection point 3 in absence of buckling or in presence of buckling. And the absolute stress difference between target point 4 and origin point 2 of branch $n+1$ is larger than the difference between the target point 2 and intersection point 1 of branch n , which means the position of reversal point 4 is elastic.

The expression to judge the status of branch $n+1$ is shown in expression (3.17).

$$\left\{ \begin{array}{l} \left| \varepsilon_r^{n+2} - \varepsilon_r^{n+1} \right| < \left| \varepsilon_y^{n+1} - \varepsilon_r^{n+1} \right| \\ \left| \sigma_r^{n+2} - \sigma_r^{n+1} \right| > \left| \sigma_r^{n+1} - \sigma_y^n \right| \\ kon(n+1) = -1 \\ \left\| flagBuckling(n+1) = 0 \right\| flagBuckling(n+1) = 1 \end{array} \right. \quad (3.17)$$

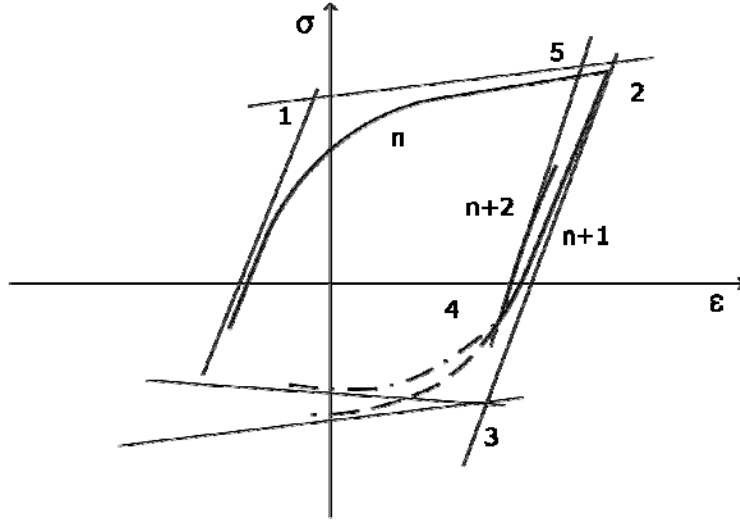


Figure 3.29 Status of branch $n+1$: Elastic, UL, AB/PB;

Update strategy: Partially update

In absence of buckling, the reloading branch $n+1$ reverses at the plastic point 4, as shown in Figure 3.30, and the criteria is given in expression (3.18):

$$\left\{ \begin{array}{l} \left| \varepsilon_r^{n+2} - \varepsilon_r^{n+1} \right| < \left| \varepsilon_y^{n+1} - \varepsilon_r^{n+1} \right| \\ \left| \sigma_r^{n+2} - \sigma_r^{n+1} \right| > \left| \sigma_r^{n+1} - \sigma_y^n \right| \\ kon(n+1) = 1 \\ flagBuckling(n+1) = 0 \end{array} \right. \quad (3.18)$$

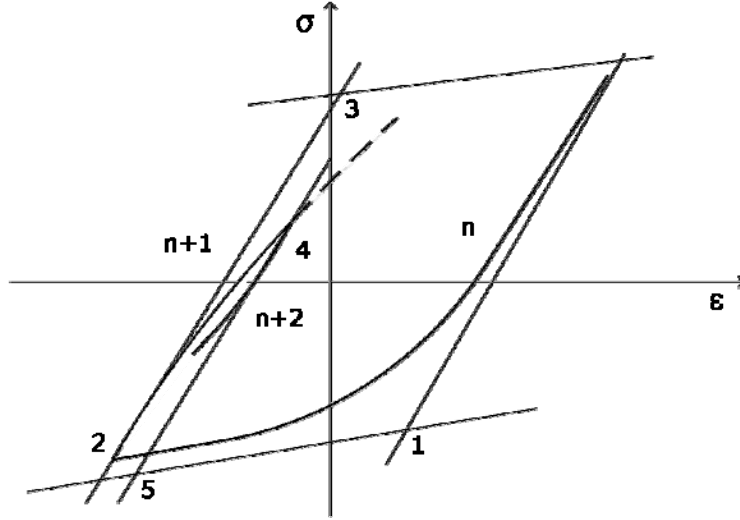


Figure 3.30 Status of branch $n+1$: Elastic, RL, AB;

Update strategy: Partially update

In Figure 3.31, the reloading branch $n+1$ reverse at the plastic point 4 in presence of buckling, and the criteria is defined in expression (3.19).

$$\left\{ \begin{array}{l} \left| \varepsilon_r^{n+2} - \varepsilon_r^{n+1} \right| < \left| \varepsilon_y^{n+1} - \varepsilon_r^{n+1} \right| \\ \left| \sigma_r^{n+2} - \sigma_r^{n+1} \right| > \left| \sigma_r^{n+1} - \sigma_y^n \right| \\ kon(n+1) = 1 \\ flagBuckling(n+1) = 1 \end{array} \right. \quad (3.19)$$

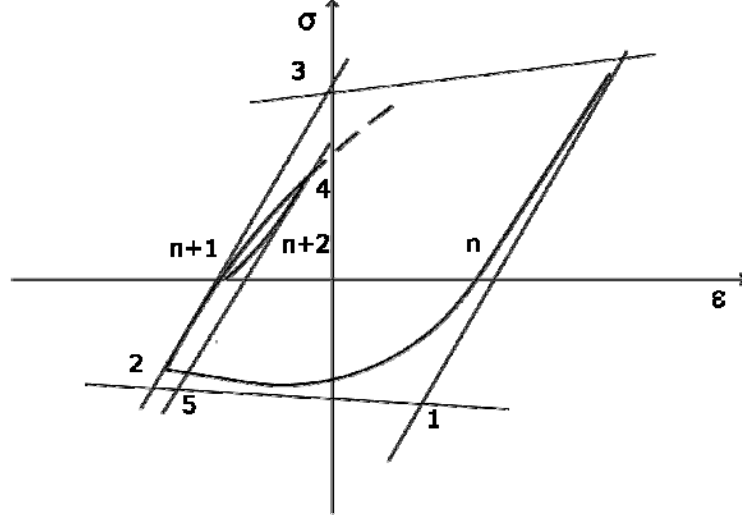


Figure 3.31 Status of branch $n+1$: Elastic, RL, PB;

Update strategy: Partially update

Figure 3.29, Figure 3.30 and Figure 3.31 demonstrate all the cases when the unloading or reloading branch $n+1$ reverse in the plastic point in absence of buckling or in presence of buckling. The strategies to update the model are identical in the aforementioned cases when branch $n+1$ reverses at plastic point. The general criteria to judge the condition when the branch $n+1$ reverses at plastic point could be summarized in expression (3.20).

$$\begin{cases} \left| \varepsilon_r^{n+2} - \varepsilon_r^{n+1} \right| < \left| \varepsilon_y^{n+1} - \varepsilon_r^{n+1} \right| \\ \left| \sigma_r^{n+2} - \sigma_r^{n+1} \right| > \left| \sigma_r^{n+1} - \sigma_y^n \right| \end{cases} \quad (3.20)$$

The strategy to update the model for branch $n+2$ is to joint the branch $n+1$ tangently to the previous branch n , the steps are shown as follows:

- i) retrieve b, R, E from branch n : $\Theta_{n+2}(b, R, E) = \Theta_n(b, R, E)$
- ii) update origin of branch $n+2$

iii) calculate the new intersection $(\varepsilon_y^{n+2}, \sigma_y^{n+2})$ between the first envelope at origin of branch $n+2$ and the tangent envelope of branch n according to Eq. (3.21).

$$\begin{cases} \varepsilon_y^{n+2} = \frac{(\sigma_y^n - \sigma_r^{n+2}) + E(\varepsilon_r^{n+2} - b\varepsilon_y^n)}{E(1-b)} \\ \sigma_y^{n+2} = \sigma_r^{n+2} + E(\varepsilon_y^{n+2} - \varepsilon_r^{n+2}) \end{cases} \quad (3.21)$$

In Figure 3.32, in absence of buckling or in presence of buckling, unloading branch $n+1$ reverses at point 3 which is quite near the origin point 2. The new branch $n+1$ goes towards the branch n along one straightline with the same tangent modulus E to branch E at its origin. Once it reaches the branch n , the new branch $n+2$ should go along the path of branch n . The status of point 3 could be defined as small, and the criteria to judge the small reversal are given in expression (3.22).

$$\begin{cases} |\varepsilon_r^{n+2} - \varepsilon_r^{n+1}| < |\varepsilon_y^{n+1} - \varepsilon_r^{n+1}| \\ |\sigma_r^{n+2} - \sigma_r^{n+1}| \leq |\sigma_r^{n+1} - \sigma_y^n| \\ kon(n+1) = -1 \\ flagBuckling(n+1) = 0 \parallel flagBuckling(n+1) = 1 \end{cases} \quad (3.22)$$

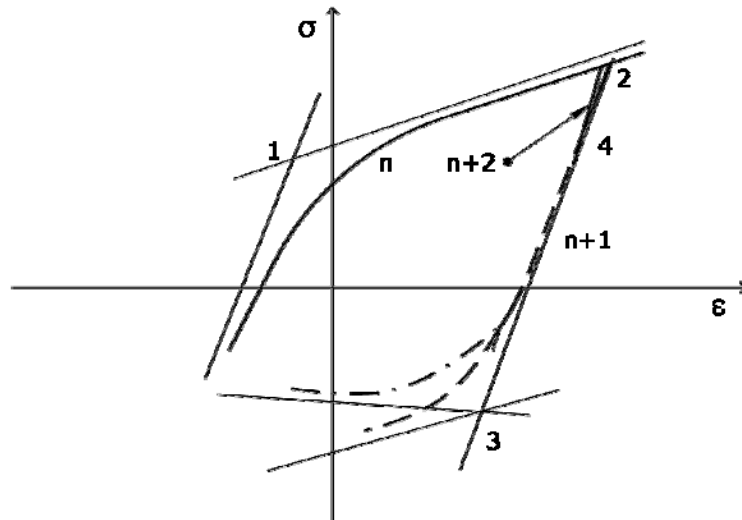


**Figure 3.32 Status of branch n+1: Small, UL, AB/PB;
Update strategy: None update**

In absence of buckling, the reloading branch $n+1$ reverses at small point 3, as shown in Figure 3.33. The criteria to judge this condition are given in expression (3.23).

$$\left\{ \begin{array}{l} \left| \varepsilon_r^{n+2} - \varepsilon_r^{n+1} \right| < \left| \varepsilon_y^{n+1} - \varepsilon_r^{n+1} \right| \\ \left| \sigma_r^{n+2} - \sigma_r^{n+1} \right| \leq \left| \sigma_r^{n+1} - \sigma_y^n \right| \\ kon(n+1) = 1 \\ flagBuckling(n+1) = 0 \end{array} \right. \quad (3.23)$$

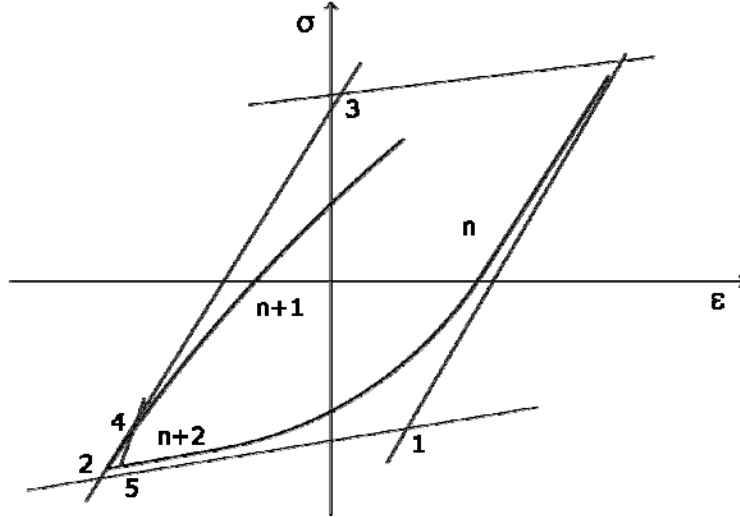


**Figure 3.33 Status of branch $n+1$: Small, RL, AB;
Update strategy: None update**

In Figure 3.34, the reloading branch $n+1$ reverses at the small point 3 in presence of buckling. The judge criterion for this case is given in expression (3.24).

$$\left\{ \begin{array}{l} \left| \varepsilon_r^{n+2} - \varepsilon_r^{n+1} \right| < \left| \varepsilon_y^{n+1} - \varepsilon_r^{n+1} \right| \\ \left| \sigma_r^{n+2} - \sigma_r^{n+1} \right| \leq \left| \sigma_r^{n+1} - \sigma_y^n \right| \\ kon(n+1) = 1 \\ flagBuckling(n+1) = 1 \end{array} \right. \quad (3.24)$$

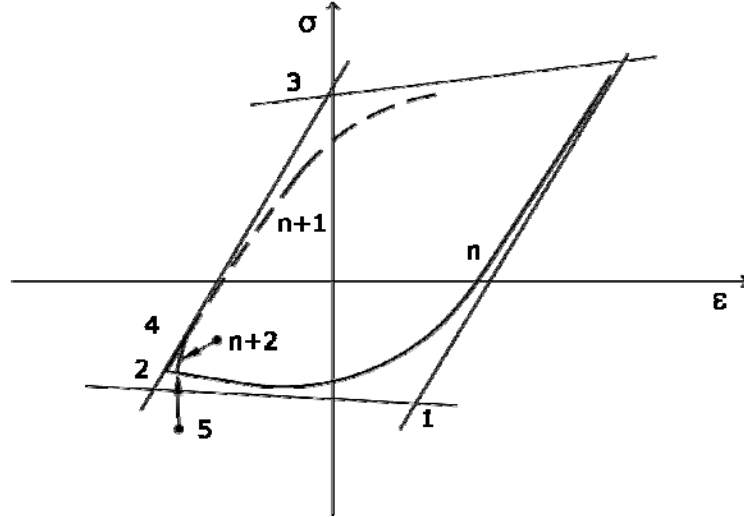


**Figure 3.34 Status of branch $n+1$: Small, RL, PB;
Update strategy: None update**

The strategies to update the model for branch $n+2$ are identical if the branch $n+1$ reverses from the small reversal. All the controlling parameters in the model for unloading or reloading branch $n+2$ are retrieved from the previous branch n no matter in absence of buckling or in presence of buckling. The strategy is given in expression (3.25).

$$\Theta_{n+2}(b, R, E, \varepsilon_r^{n+2}, \sigma_r^{n+2}, \varepsilon_y^{n+2}, \sigma_y^{n+2}) = \Theta_n(b, R, E, \varepsilon_r^n, \sigma_r^n, \varepsilon_y^n, \sigma_y^n) \quad (3.25)$$

It should be highlighted that before the branch $n+2$ reaches branch n , the new branch goes along the line which starts from the target point of branch $n+1$ and retrieves the tangent modulus E from branch n .

4. PARAMETER IDENTIFICATION BY GENETIC ALGORITHM

In the Modified Monti-Nuti Model, the values of the parameters such as A_1^t , A_2^t , A_1^c , A_2^c , r_t and r_c needed to be assigned. In order to obtain the reasonable values of the parameters, the parameter identification is carried out based on a series of experimental curves. Then the empirical formulas are proposed.

4.1 INTRODUCTION OF PARAMETER IDENTIFICATION BY GENETIC ALGORITHM

Parameter identification is used to select the proper values of the parameters in the model (Quaranta, Monti, & Marano, 2010). Here the Genetic Algorithm is used to generate the possible solutions for the parameters in the model.

4.1.1 Parameter Identification

Parameter identification is to determine the proper values of the parameters in the model in order to generate precise numerical curves which could coincide with the experimental curve very well. Theoretically, the numerical should be the same with the experimental curve, thus the experimental curve could be designated as the numerical curve, and subsequently, the values of the parameters in the model could be deduced. The parameter identification is a reversal process.

However, the Monti-Nuti model is one path-dependent model, and it is impossible to deduce the values of the parameters in the model. Thus, above all, a series of values of the parameters could be assigned, and then generate the numerical curve, finally, define some rules to calculate the curvature tolerance between the numerical curve and the experimental curve. Reassign the values of the parameters in the model and repeat this process unless the curve tolerance meets the demand.

The general flowchart of the parameter identification is shown in Figure 4.1. There could be a lot of iterations before the proper set of the

parameter values could be found, thus it is necessary to reassign the values of the parameters and generate the numerical curve and then compare with the experimental curve automatically instead of iterate this progress manually. In order to achieve this aim in an efficient way, the genetic algorithm is adopted.

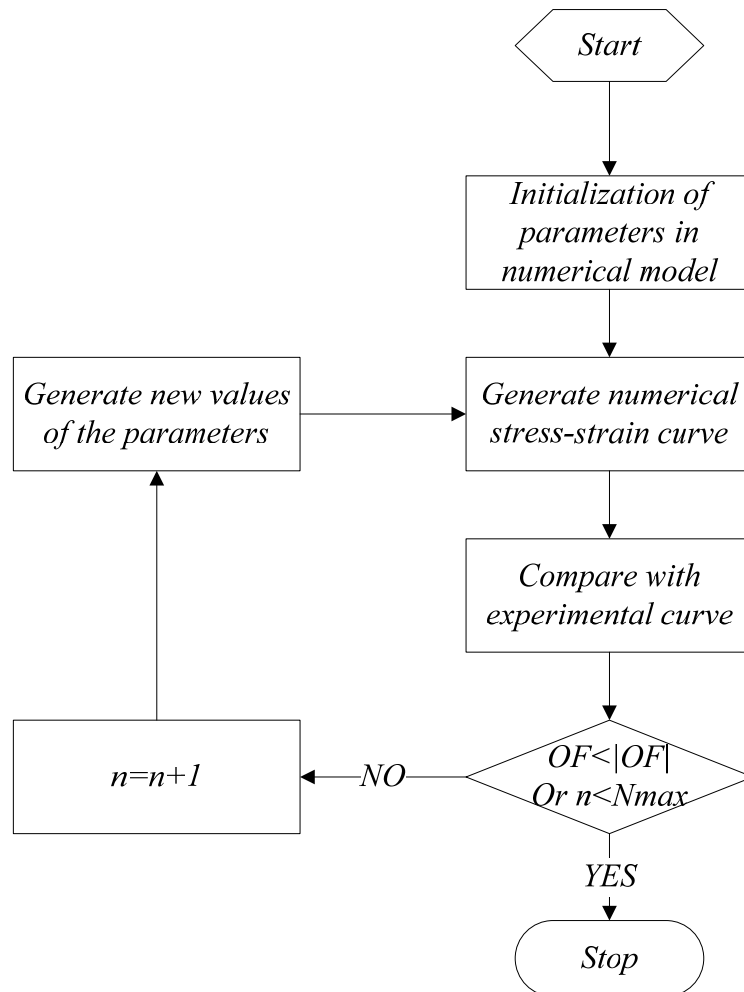


Figure 4.1 General flowchart of parameter identification

4.1.2 Genetic Algorithm

Genetic algorithms belong to evolutionary algorithms (EA), which generate solutions to optimization problems using techniques mimicking natural evolution, such as inheritance, mutation, selection, and crossover. In a genetic algorithm (Marano, Quaranta, & Monti, 2011), a group of candidates named individuals are evolved toward better solutions. Each individual has a set of properties to represent the parameters to be optimized, which can be mutated and altered. The evolution usually starts from a population of randomly assigned individuals, and is an iterative process. The group of the individuals in each iteration is called a generation. In each generation, the fitness of every individual in the group is evaluated; the fitness is usually the value of the objective function in the optimization problem being solved. The fittest individuals are stochastically selected from the current generation, and each individual is modified (recombined and possibly randomly mutated) to form a new generation. The new generation of candidate solutions is then used in the next iteration of the algorithm. Commonly, the algorithm terminates when either a maximum number of generations has been produced, or a satisfactory fitness level has been reached for the population.

A typical genetic algorithm requires:

- 1) A genetic representation of the solution domain;
- 2) A fitness function to evaluate the solution domain.

Once the genetic representation and the fitness function are defined, a GA proceeds to initialize a population of solutions and then to improve it through repetitive application of the mutation, crossover, inversion and selection operators.

4.2 DESIGN OF PARAMETER IDENTIFICATION OF MODIFIED MONTI-NUTI MODEL

In this section, the parameters are selected to carry out parameter identification. Then the flowchart of the parameter identification is illustrated. Next the object function defined for the identification is introduced. Finally the lower bound and upper bound of the parameters are given.

4.2.1 Parameters to Be Calibrated

In the modified Monti-Nuti model, the parameter b , E_0 and f_y are determined by the material properties. However, the curve transition parameter R and weight coefficient parameter P in the strain hardening rule should be specified. In order to update R , r_t , A_1^t and A_2^t are defined to update R in tension, and r_c , A_1^c and A_2^c are defined to update R in compression. Meanwhile, the tangent modulus E_s at reversal from compressive branch to tensile branch is updated by A_5 and A_6 , and A_5 is defined by an empirical formula. According to parameters study, the value of the weight coefficient P could be set as constant 0.5. The parameters need to be calibrated are listed in Table 4.1.

Table 4.1 Lists of parameters to be calibrated

Parameters	Meaning
r_t	Parameter to calculate R_0 in tension
r_c	Parameter to calculate R_0 in compression
A_1^t	Parameter to update R in tension
A_2^t	Parameter to update R in tension
A_1^c	Parameter to update R in compression
A_2^c	Parameter to update R in compression
A_6	Parameter to update E at reversal from compression to tension

4.2.2 Flowchart

The flowchart to identify the parameters in the modified Monti-Nuti model is designed and illustrated in Figure 4.2.

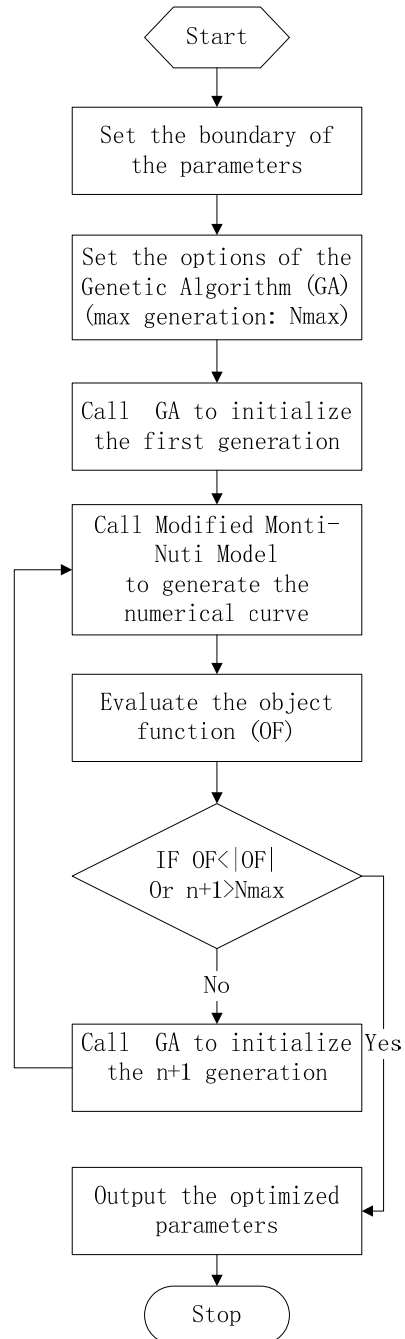


Figure 4.2 Parameter identification of modified Monti-Nuti model

4.2.3 Objective Function

In order to do the parameter identification, the fitness function, as generally defined in Eq. (4.1), has the form:

$$f = \frac{\Delta Y}{Y} \quad (4.1)$$

Where ΔY represents the difference between the numerical curve and the experimental curve and is defined as: $\Delta Y = \sum_{i=1}^n y_{E,i}^2 - y_{N,i}^2$, and $y_{E,i}$ and $y_{N,i}$ are the stress on the experimental curve and numerical curve corresponding to the same strain; Y is the sum of the square of the experimental stresses, and is defined as: $Y = \sum_{i=1}^n y_{E,i}^2$.

If there are more than one experimental tests, define the weight coefficient w_k to decide the contribution of each test, thus the fitness function could be defined as Eq. (4.2) :

$$f = \sum_{k=1}^m w_k f_k \quad (4.2)$$

Where f_k is the value of the fitness function for each experiment, and is defined in Eq. (4.3).

$$f_k = \frac{\Delta Y_k}{Y_k} \quad (4.3)$$

4.2.4 Bounds of the Parameters

The bounds of the parameters determine the region where the Genetic Algorithm could search for the optimized values of the parameters. Theoretically, the larger bounds are specified, the more likely to search better optimized solution. However, if the bounds are not set properly, the model could generate complex stress value which is meaningless and should be avoided. Through a series of trial and error, the bounds of the parameters to be identified are specified in Table 4.2.

Table 4.2 Lower bound and Upper bound of the parameters

	r_t	r_c	A_1^t	A_2^t	A_1^c	A_2^c	A_6
LB	1	1	5	0.00001	5	0.00001	300
UB	20	20	100	0.03	100	0.03	5000

Note: LB is short for Lower Bound, and UB is short for Upper Bound.

4.3 EFFECTIVENESS OF THE OPTIMIZED PARAMETERS

Through parameter identification, the optimized values of the parameters are obtained. The numerical curves generated by the modified model using the optimized parameters are illustrated. Furthermore, the robustness of the parameter identification (Marano, Greco, & Sgobba, 2010) is demonstrated.

4.3.1 Stress-Strain Curve

The comparisons are made between the numerical curves generated by the modified Monti-Nuti model and the experimental curves of the carbon steel rebar shown in Figure 4.3 and Figure 4.4, and the comparisons about the stainless steel rebar are illustrated in Figure 4.5 and Figure 4.6.

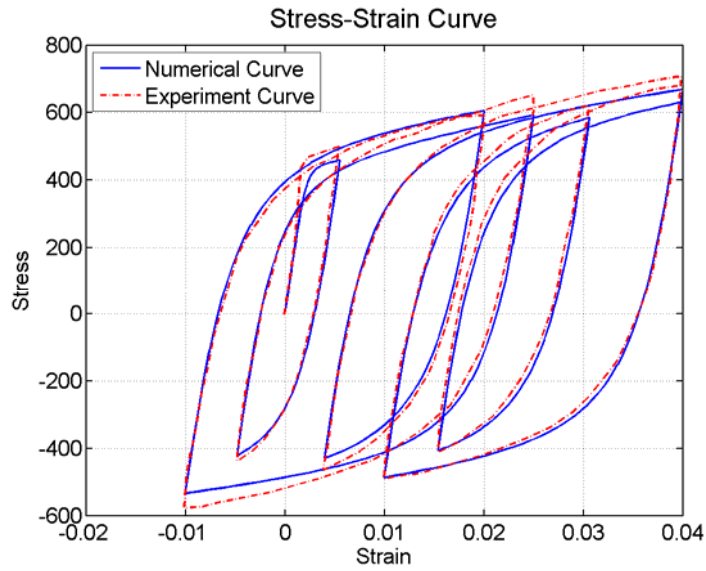


Figure 4.3 Comparison between experimental curve and numerical curve generated by modified Monti-Nuti Model (carbon steel rebar, A1, L/D=5)

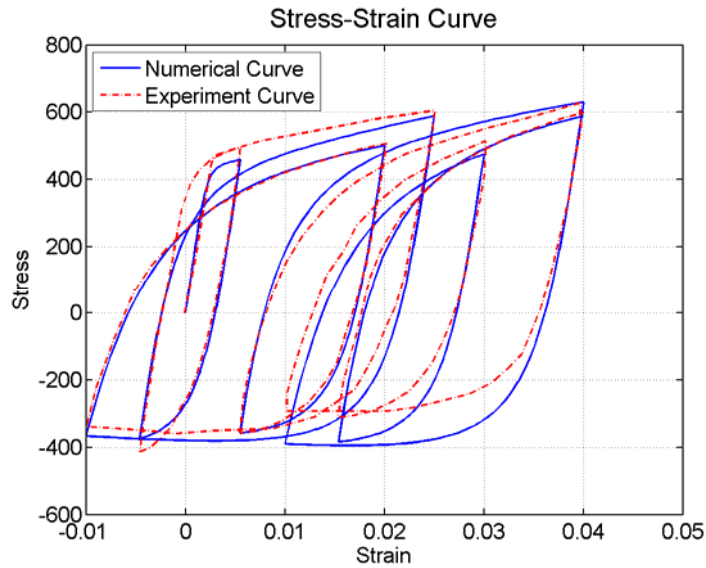


Figure 4.4 Comparison between experimental curve and numerical curve generated by modified Monti-Nuti Model (carbon steel rebar, C1, L/D=11)

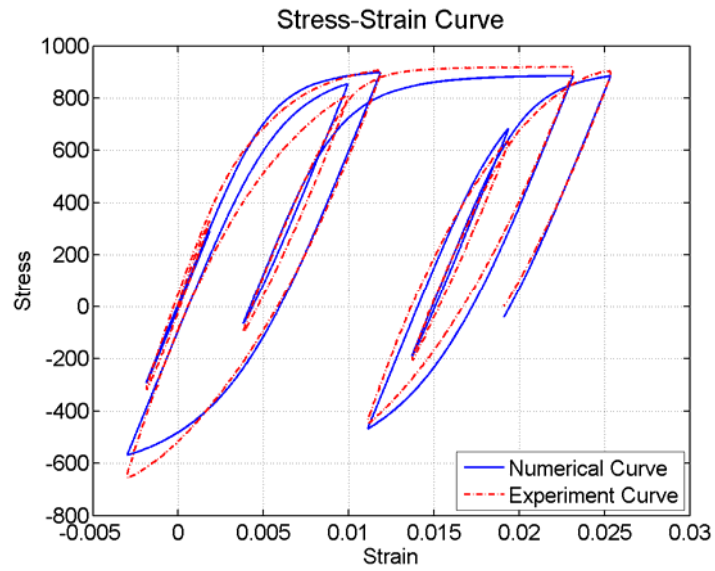


Figure 4.5 Comparison between experimental curve and numerical curve generated by modified Monti-Nuti Model (stainless steel rebar, XA1, $L/D=5$)

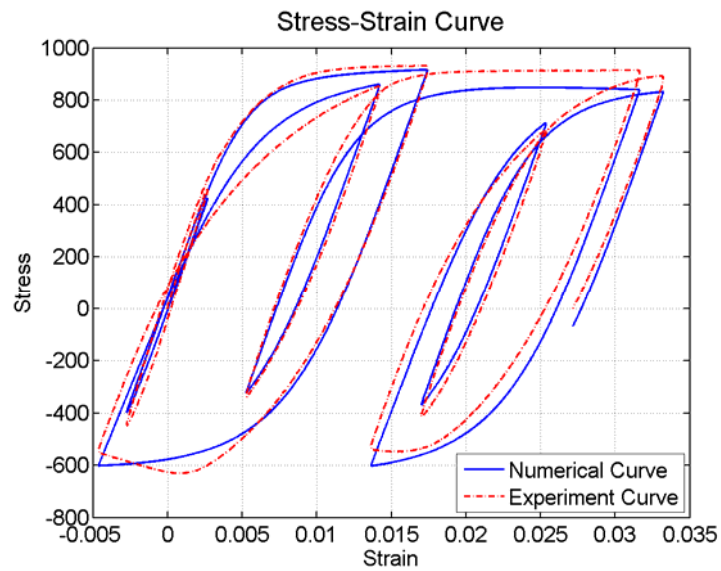


Figure 4.6 Comparison between experimental curve and numerical curve generated by modified Monti-Nuti Model (stainless steel rebar, XC1, $L/D=11$)

4.3.2 Step-Stress Comparison

In the step-stress curves, the step stands for the loading strain histories, the stresses of the experimental curve and the numerical curve correspond to the same strain at each step. From the step-stress curve, the comparison indicates the modified Monti-Nuti model could simulate the experimental curve quite precisely.

The comparisons of the carbon steel rebar with slenderness L/D equal to 5 are shown in Figure 4.7, and the comparisons of the carbon steel rebar with slenderness L/D equal to 11 are shown in Figure 4.8. In Figure 4.9, the step-stress curve of the stainless steel rebar with L/D equal to 5 is demonstrated; and the step-stress curve of the stainless steel rebar with L/D equal to 11 is illustrated in Figure 4.10.

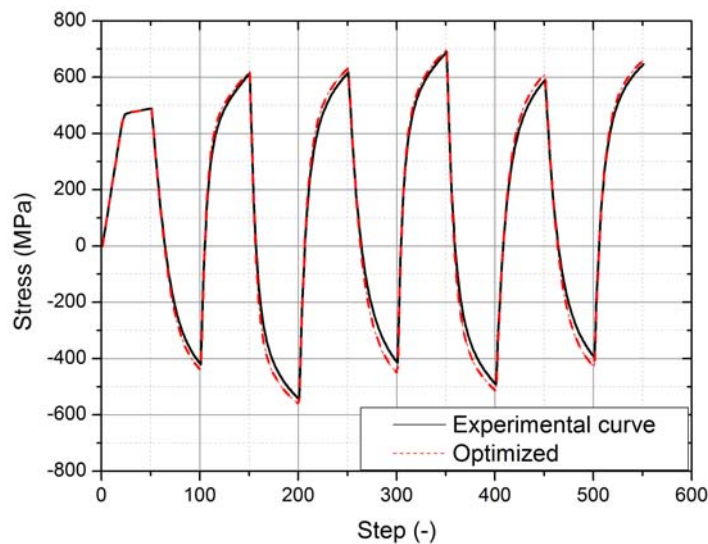


Figure 4.7 Step-Stress comparison between experimental curves and numerical curve with optimized parameters (carbon steel rebar, $L/D=5$, A1)

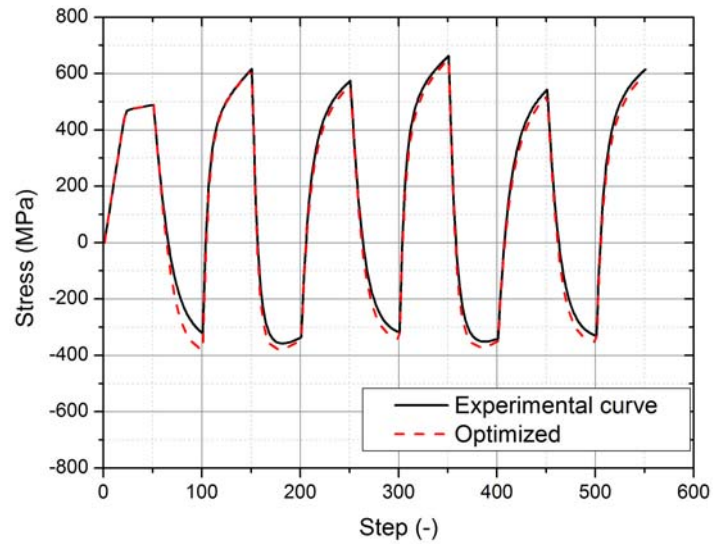


Figure 4.8 Step-Stress comparison between experimental curves and numerical curve with optimized parameters (carbon steel rebar, $L/D=11$, C1)

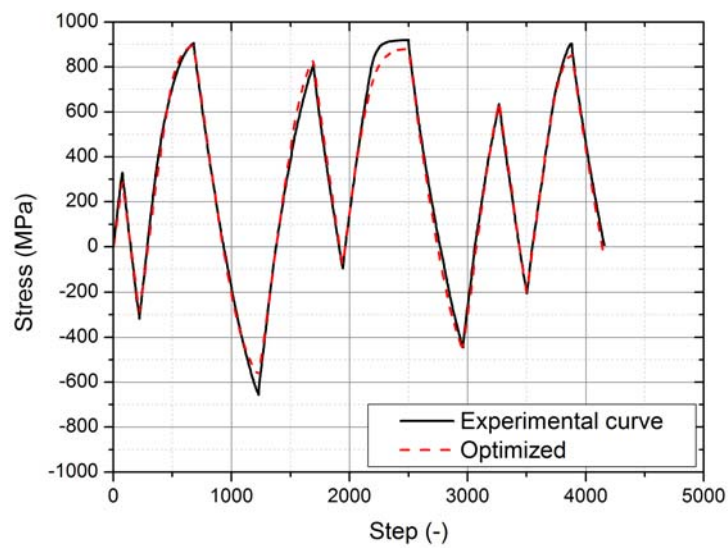


Figure 4.9 Step-Stress comparison between experimental curves and numerical curve with optimized parameters (stainless steel rebar, $L/D=5$, XA1)

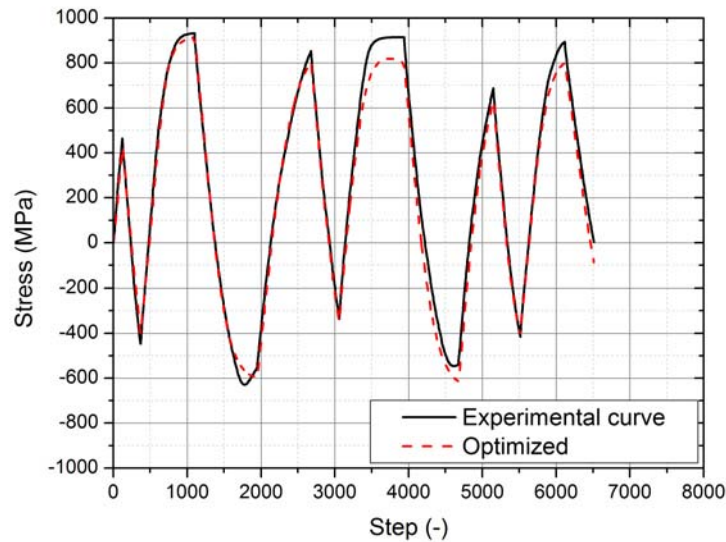


Figure 4.10 Step-Stress comparison between experimental curves and numerical curve with optimized parameters (stainless steel rebar, $L/D=11$, XC1)

4.3.3 Robustness

As for the parameter identification, robustness means that the optimized parameters could be used by the model to generate precise numerical curve for different types of rebar, such as rebar different slenderness and different loading histories.

The parameter identification is carried out for the carbon steel rebar and the stainless steel rebar with different slenderness and different loading histories. First of all, the parameter identification is made for the rebar with different loading histories individually, and then the rebars with same slenderness and different loading histories are identified together to find the best optimization for the rebar with the same slenderness.

The identified values for the stainless steel rebars with slenderness L/D equal to 5 are listed in Table 4.3 and the optimized values of the parameters with slenderness L/D equal to 11 are listed in Table 4.4.

Table 4.3 Parameter Identification for stainless steel rebar (L/D=5)

	XA1	XA2	XA3	XA	Mean	Standard Deviation	Difference (%) Standard Deviation/ Mean
A_1^t	2.524	2.765	2.473	2.759	2.587	0.127	4.9
A_2^t	0.007	0.020	0.004	0.010	0.010	0.007	67.2
A_1^c	2.949	2.254	2.911	2.403	2.705	0.319	11.8
A_2^c	0.002	0.001	0.012	0.001	0.005	0.005	99.3

Note: XA means the optimized values for XA1, XA2 and XA3, with L/D=5.

Table 4.4 Parameter Identification for stainless steel rebar (L/D=11)

	XC1	XC2	XC3	XC	Mean	Standard Deviation	Difference (%) Standard Deviation/ Mean
A_1^t	2.584	2.858	2.985	2.842	2.809	0.167	6.0
A_2^t	0.004	0.003	0.002	0.002	0.003	0.001	27.2
A_1^c	2.509	2.004	2.688	2.429	2.400	0.290	12.1
A_2^c	0.004	0.002	0.009	0.002	0.005	0.003	58.9

Note: XC means the optimized values for XC1, XC2 and XC3, with L/D=11.

The robustness of the optimized could be observed from and Table 4.4. A_1^t and A_1^c are sensitive to the numerical model, and the identified values of the parameters vary in a little range. But A_2^t and A_2^c are not sensitive to the model, thus the derivation of values have little effect on the numerical results. The column diagram of A_1^t and A_1^c is shown in Figure 4.11, the variations of the parameter A_1^t and A_1^c for the stainless steel rebar with different slenderness in different loading cases are small.

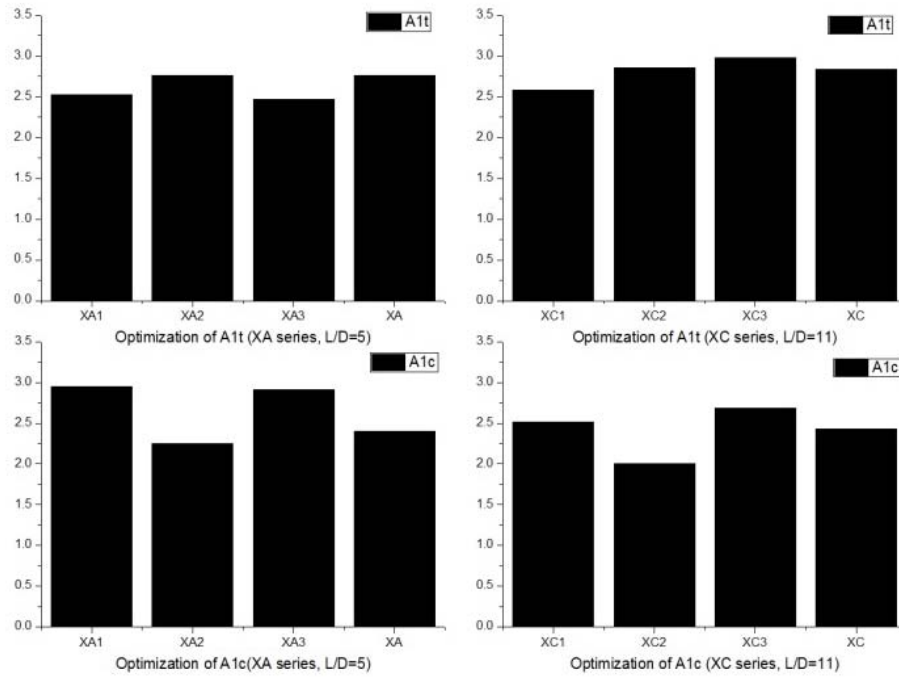


Figure 4.11 Derivations of optimized parameters

4.4 PROPOSED FORMULAS FOR THE PARAMETERS IN THE MODIFIED MONTI-NUTI MODEL

Through parameter identification, a series of optimized parameters are obtained for different types of rebars with different slenderness and different loading histories. Then the empirical formulas are given to evaluate the parameters to calculate R , which are given in Eq. (3.10-3.12).

5. Implementation and Validation of the Modified Monti-Nuti Model

The modified Monti-Nuti model incorporates the effect of the yield strength of different rebar and the effect of the anisotropy. This modified Monti-Nuti model is implemented in OpenSees and named as “Steel05” (Zhou, Nuti, & Lavorato, 2015b).

It is found that the Monti-Nuti model could overestimate the stress if the partial unloading and reloading strain histories are very complicated, and the methods to eliminate this disadvantage of the model is proposed and thus the robustness of the model is improved. Subsequently, in order to validate the effectiveness of the modified Monti-Nuti model, the experiments on the carbon steel rebars and stainless steel rebars are used to compare with the numerical stress-strain curves generated by the modified model.

5.1 IMPLEMENT THE MATERIAL MODEL IN OPENSEES

OpenSees is object-oriented Finite Element program (Mckenna, 1997), and the library file of the custom designed material model could be loaded by the framework when the OpenSees.exe is running and it comes across the custom designed material. The modified Monti-Nuti Model is named as “Steel05” and is compiled as “Steel05.dll”, thus this new material model could be used in OpenSees to simulate the rebar in concrete structures in OpenSees. The inheritance diagram of the new steel model “Steel05” is shown in Figure 5.1.

As OpenSees is open source software, there are two ways to implement the material model into OpenSees (OpenSees). Implement the material as one dynamic link library and the OpenSees executable will automatic to load the Steel05.dll file when the material “Steel05” is used in the OpenSees scripts. The other way is to add the material file into the OpenSees framework and recompile the whole framework to build one

new OpenSees executable. Thus the “Steel05” material is included in the new built executable. The author of this dissertation has succeeded in implementing the new material model in both two ways. The first way is easier to be carried out by OpenSees developers and it is a better way to share the new material model with other users.

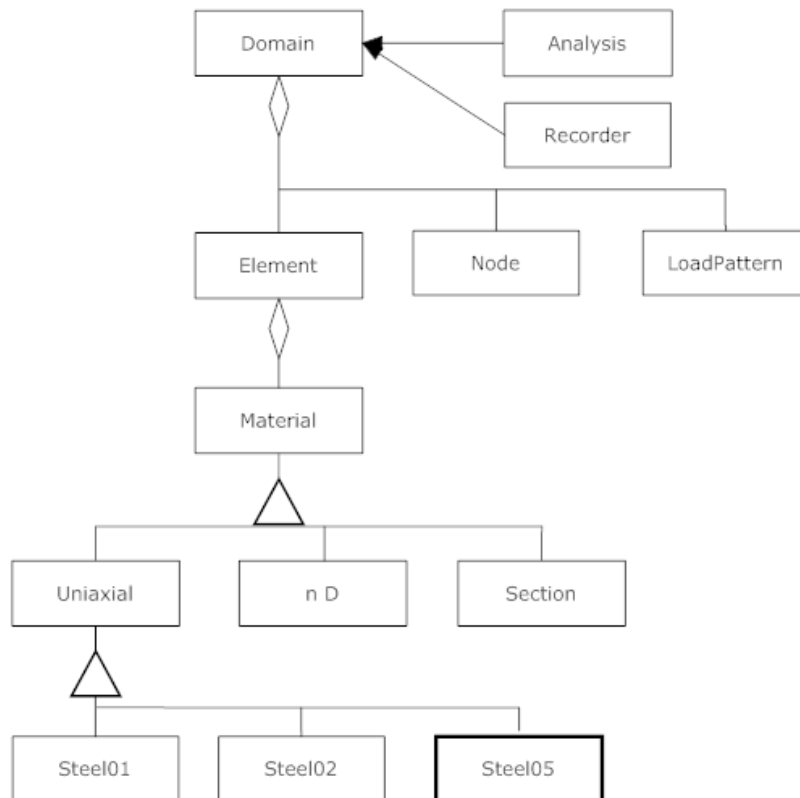


Figure 5.1 Inheritance Diagram of steel model “Steel05”

5.2 Validation of the Modified Monti-Nuti Model

After the modified Monti-Nuti model is implemented in the OpenSees, this material is used to simulate the tested bare rebars and compare with the experimental curves.

In order to test the material model “Steel05” in OpenSees, one structural element such as one column should be built, and proper element could be used to simulate the force-displacement of the column, and then the steel material “Steel05” implemented in OpenSees could be used to describe the stress-strain relationship of the cross section of the element. The benchmark test method proposed by Michael H. Scott was adopted to simplify the test model, as illustrated in Figure 5.2. One special 1D column is set up and the unit length and unit cross section are specified, and the axial displacement is applied on the column. Thus the output force equals the axial force of the column, and the applied axial displacement equals the strain. That is to say, the output axial force-axial displacement curve of the element is identical to the stress-strain curve of the material.

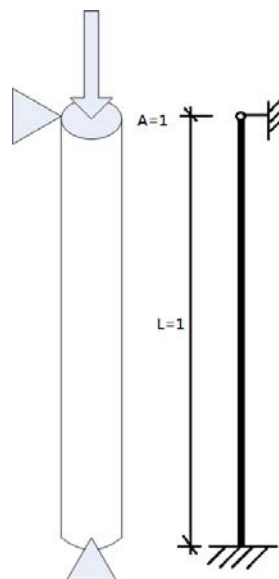


Figure 5.2 Column setup in OpenSees for material test

The scripts in Figure 5.3 are used to build the column in OpenSees and apply the strain histories and output the corresponding axial force. Then the stress-strain curves of different types of rebars are plotted and the comparisons are illustrated.

```

# Units: MP, mm
model BasicBuilder -ndm 1 -ndf 1
# Define nodes
node 1 0.0
node 2 1.0
# Fix node 1
fix 1 1
# Define uniaxialMaterial
# Steel05 $matTag $fy_tension $fy_compression $E0 $stirrup_spacing $D $r0 $A6 $P
uniaxialMaterial Steel05 1 440 440 0.03 200000 220 20 5 1000 0.5
# Define truss element with unit area
# tag ndI ndJ A matTag
element truss 1 1 2 1.0 1
set dt 1.0;      # Increment between data points
set filename pattern1.txt;      # Filename containing data points
set factor 1;    # Factor applied to data values
# Read displacement pattern from file
# Note, any pattern type can be used here: Linear, Path, Sine, etc.
pattern Plain 1 "Series -dt $dt -filePath $filename -factor $factor" {
# Set reference displacement value
# node dof value
sp 2 1 1.0
}
# Record nodal displacements (same as strains since truss length is 1.0)
recorder Node -file truss.out -node 2 -dof 1 disp
# Record truss force (same as stress since truss area is 1.0)
recorder Element -file force.out -ele 1 force
system UmfPack
constraints Penalty 1.0e12 1.0e12
# Set increment in load factor used for integration
# Does not have to be the same as dt used to read in displacement pattern
set dl $dt
integrator LoadControl $dl 1 $dl $dl
test NormDispIncr 1.0e-6 10
algorithm Newton
numberer RCM
analysis Static
analyze 521
exit

```

Figure 5.3 Scripts used to test “Steel05” in OpenSees

5.2.1 Experiments of Carbon Steel Rebar

For the carbon steel rebar tests, the A series tests are the cyclic tests with slenderness ratio L/D equal to 5, and the yield stress is 450 MPa, thus $\sqrt{f_y/450}(L/D)$ is 5, which means that the A series are the cyclic curves without buckling. In the C series tests, the L/D is 11, and $\sqrt{f_y/450}(L/D)$ equals 11, which means that the buckling should emerge in the cyclic curves.

The properties of the tested carbon steel rebars are listed in Table 5.1. The cyclic loading histories of the carbon steel rebar are shown in Figure 5.4.

Table 5.1 Properties of tested carbon steel rebar

<i>Test</i>	<i>L/D</i>	<i>Yield stress</i> <i>f_y</i> (MPa)	<i>Elastic modulus</i> <i>E_s</i> (MPa)	<i>Hardening ratio</i> <i>b</i>
A1/ C1	5/11	470	200000	0.03
A2/ C2	5/11	470	200000	0.03
A3/ C3	5/11	430	180000	0.04
A4/ C4	5/11	450	160000	0.04

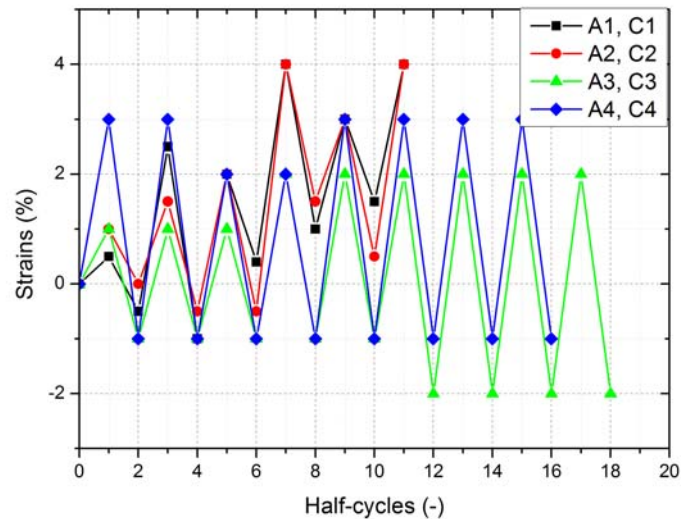
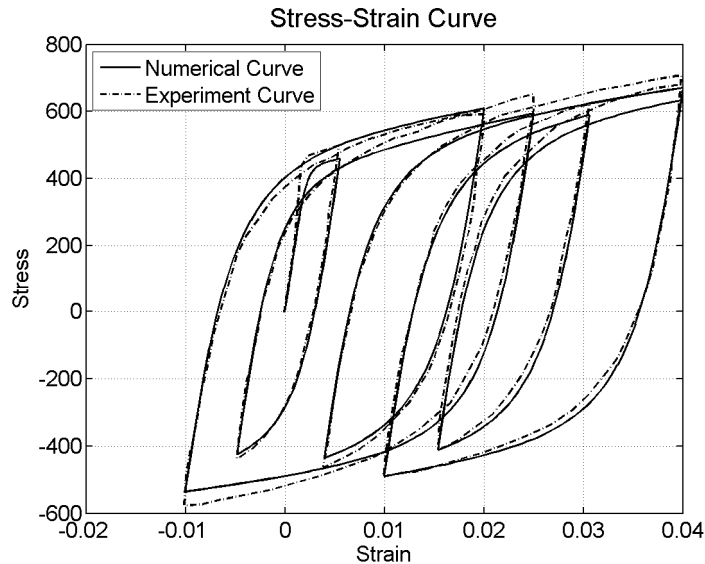


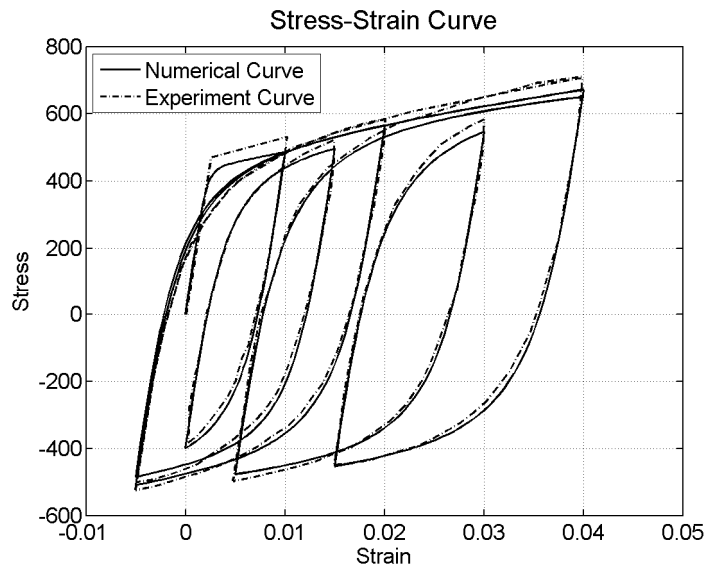
Figure 5.4 Loading strain histories of carbon steel reinforcement
(A1, A2, A3 and A4: $L/D=5$; C1, C2, C3 and C4: $L/D=11$)

The comparisons between the numerical curves generated by the modified model and the experimental curves of the carbon steel rebars are shown in Figure 5.5 and Figure 5.6.

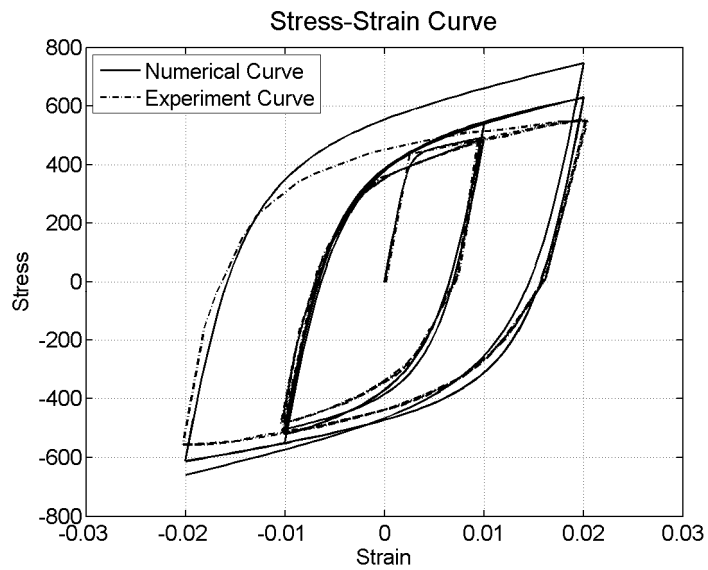
The numerical curves coincide with the experimental curves quite well but there are disagreement to some degree if the compressive strain is smaller than -0.01. However, for the real concrete structures, the strain of the reinforcement could not exceed -0.01 due to the confinement of the concrete, thus the model is applicable in the seismic analysis of real structures.



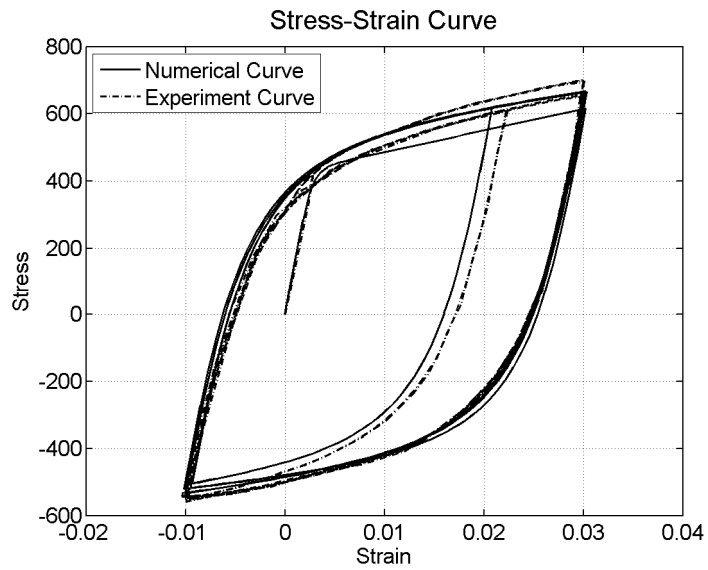
(a) in absence of buckling-A1



(b) in absence of buckling-A2

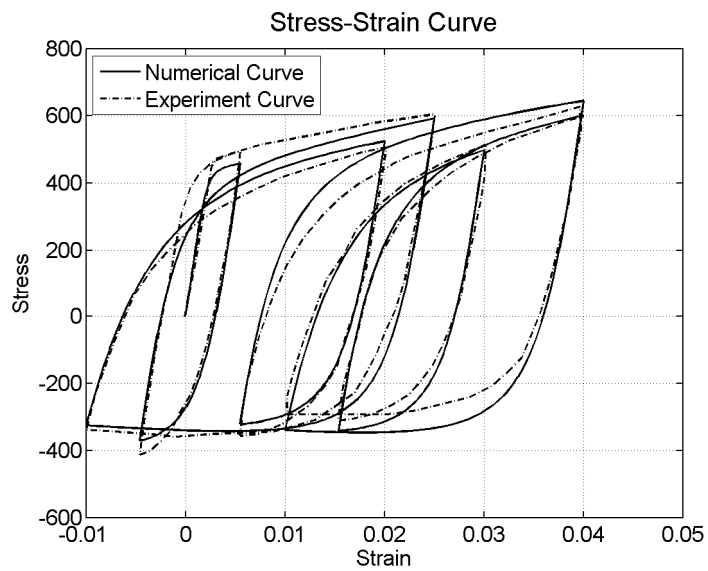


(c) in absence of buckling-A3

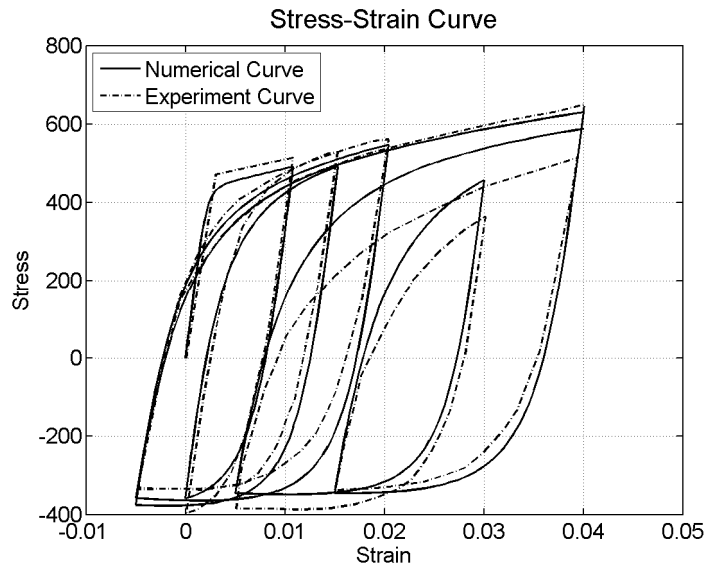


(d) in absence of buckling-A4

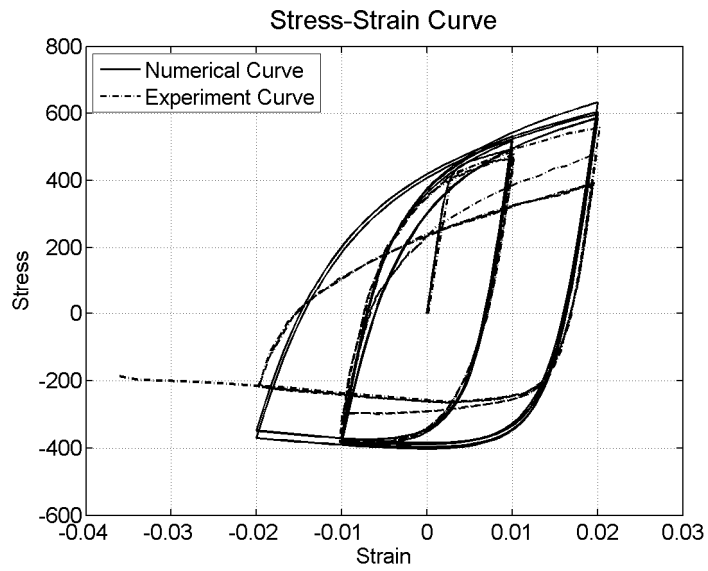
Figure 5.5 Comparison of numerical curves and experimental curves
($L/D=5$)



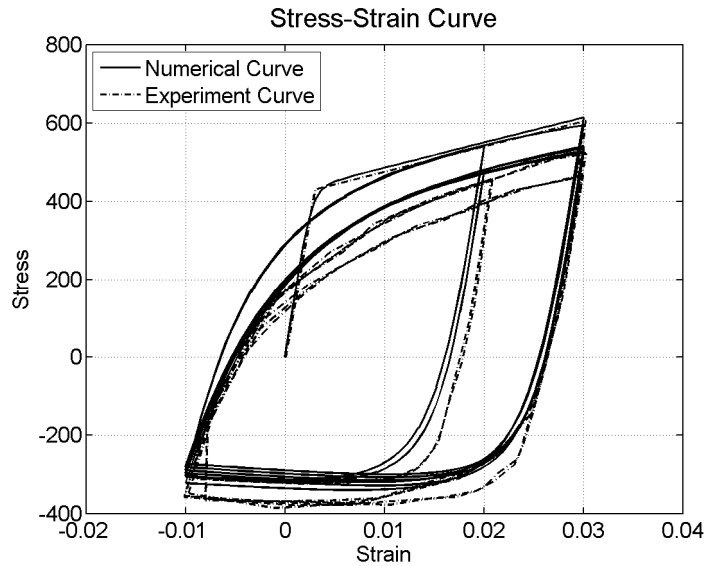
(a) in presence of buckling-C1



(b) in presence of buckling-C2



(c) in presence of buckling-C3



(d) in presence of buckling-C4

**Figure 5.6 Comparison of numerical curves and experimental curves
($L/D=11$)**

In chapter 3, the comparisons between the numerical curves generated by the original Monti-Nuti model are made. The original Monti-Nuti model could not simulate the cyclic behaviors of the rebar with properties listed in Table 5.2.

Here the comparisons between the numerical curves generated by the modified Monti-Nuti model and the experimental curves are made. The loading histories are shown in Figure 5.7. The comparisons are shown in Figure 5.8, Figure 5.9 and Figure 5.10.

Table 5.2 Properties of test rebar (Dhakai and Maekawa 2002)

<i>Test</i>	<i>L/D</i>	<i>f_y (MPa)</i>	<i>E_s (MPa)</i>	<i>b</i>
S5	5	500	200000	0.037
S8	8	500	200000	0.037
S11	11	500	200000	0.037

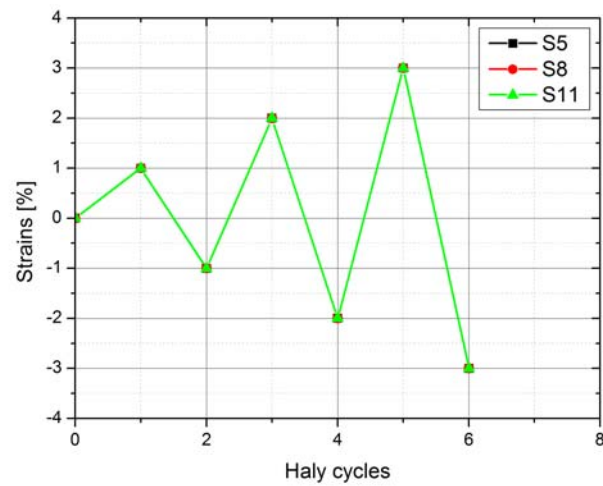


Figure 5.7 Loading strain histories of carbon steel reinforcement (S5, $L/D=5$; S8, $L/D=8$; and S11, $L/D=11$, from Dhakal and Maekawa, 2002)

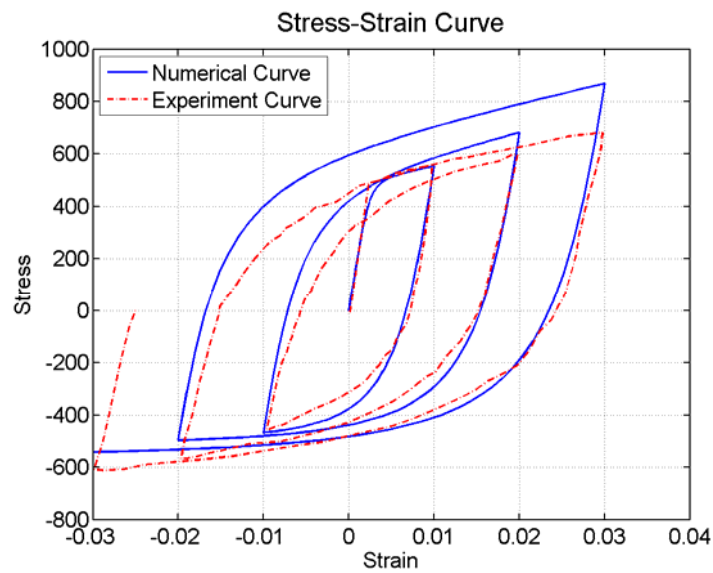


Figure 5.8 Comparison of numerical curves and experimental curves (S5, $L/D=5$)

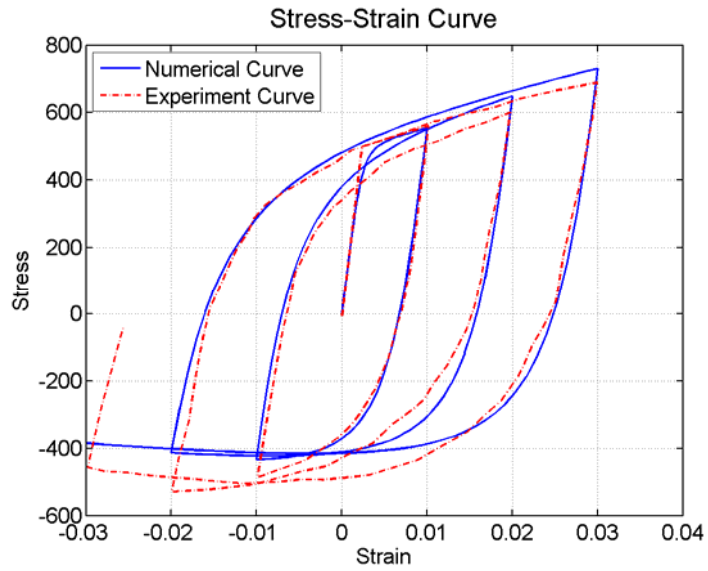


Figure 5.9 Comparison of numerical curves and experimental curves (S8, $L/D=8$)

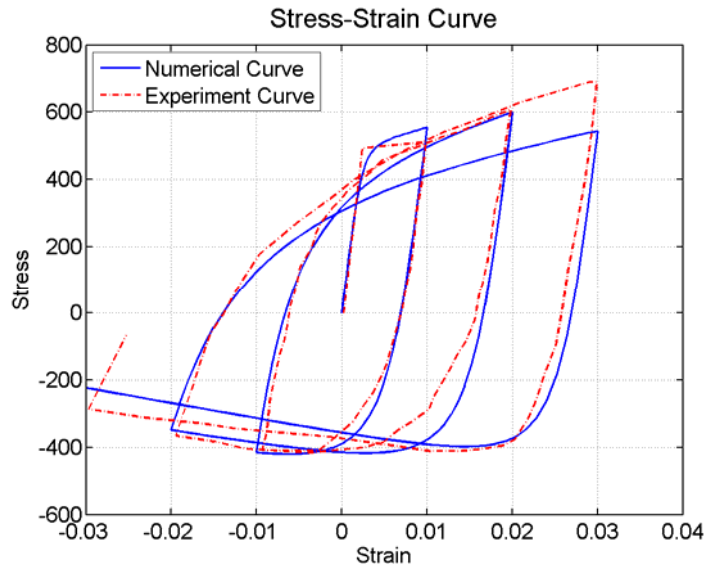


Figure 5.10 Comparison of numerical curves and experimental curves (S11, $L/D=11$)

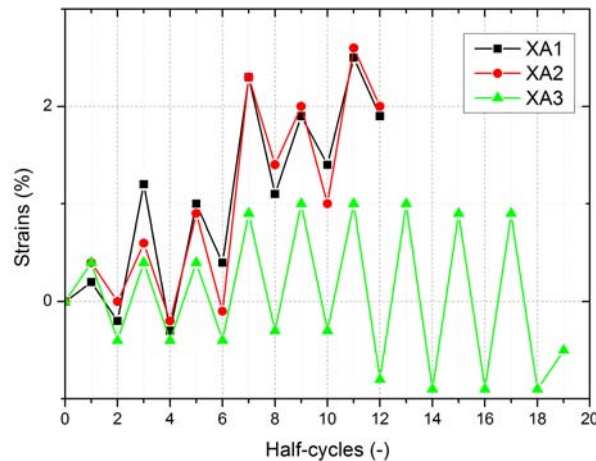
5.2.2 Experiments of Stain Steel Rebar

The effectiveness of the modified Monti-Nuti model is verified by simulating the cyclic behaviors of the stainless steel rebar with different yield stresses in tension and in compression. The properties of the stainless steel rebar are listed in Table 5.3. The XA1, XA2 and XA3 are tests of rebars with slenderness L/D equal to 5; and the XC1, XC2 and XC3 are tests of rebars with slenderness L/D equal to 11.

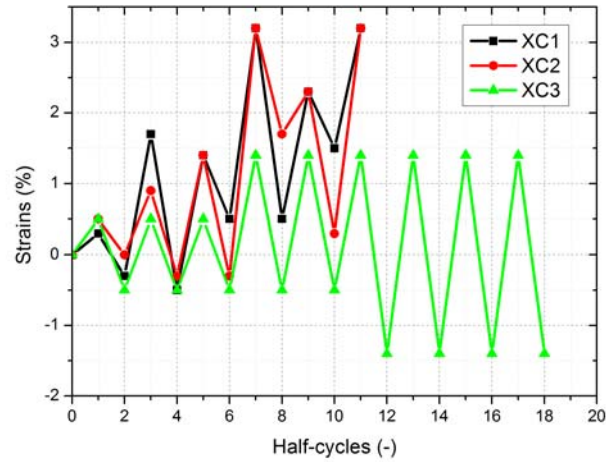
Table 5.3 Properties of tested stainless steel rebar

Test	L/D	Yield stress in tension f_{yt} (MPa)	Yield stress in compression f_{yc} (MPa)	E_s (MPa)	b
XA1/XC1	5/11	790	680	200000	0.02
XA2/XC2	5/11	790	680	200000	0.02
XA3/XC3	5/11	790	680	200000	0.02

The loading histories for XA1, XA2 and XA3 are shown in Figure 5.11 a), and the loading histories for XC1, XC2 and XC3 are shown in Figure 5.11 b).



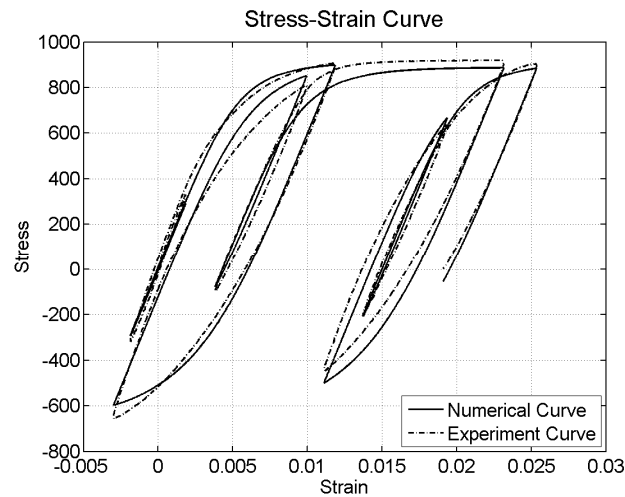
a) XA1, XA2 and XA3 ($L/D=5$)



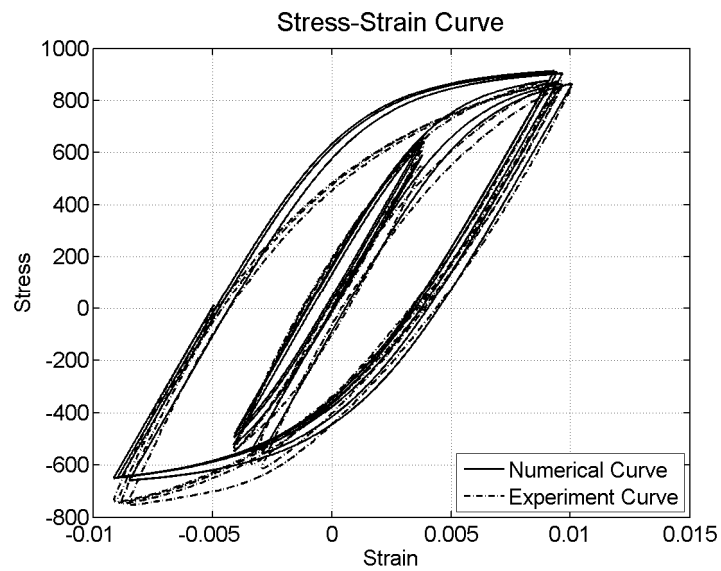
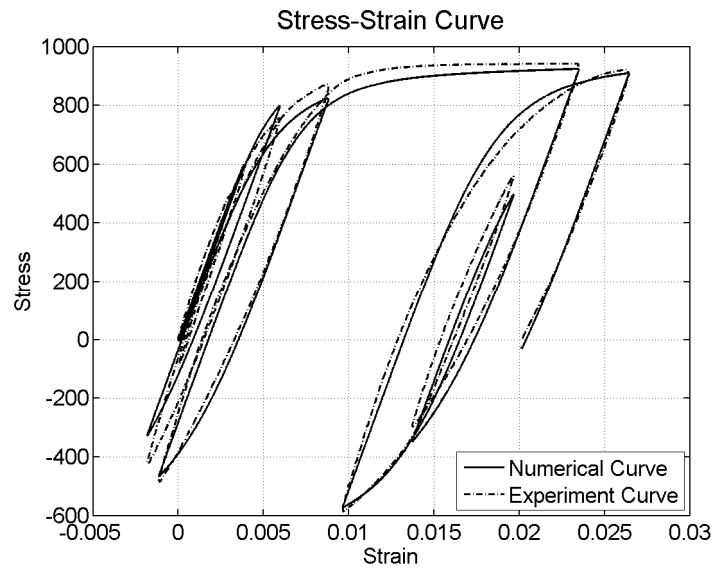
b) XC1, XC2 and XC3 (with $L/D=11$)

Figure 5.11 Loading strain histories of stainless steel reinforcement

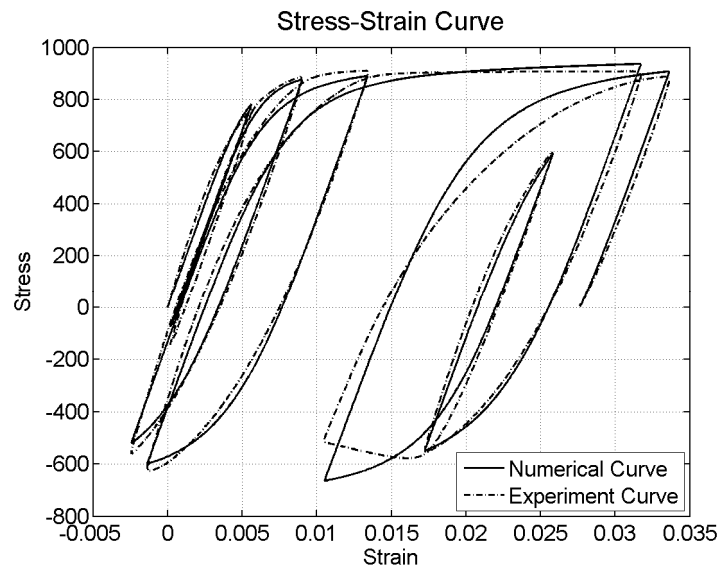
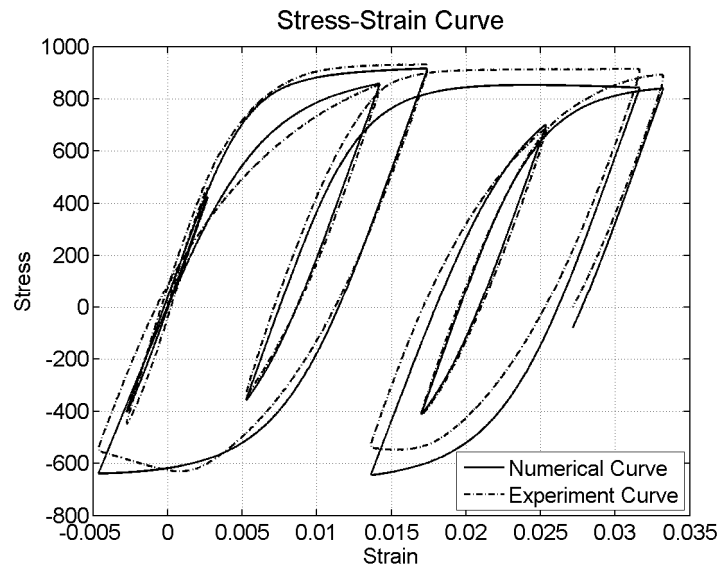
For the stainless steel rebars, the numerical curves could coincide with the experimental curves very well, shown in Figure 5.12 and Figure 5.13, thus the validity of the model in simulating the anisotropic material is also verified.

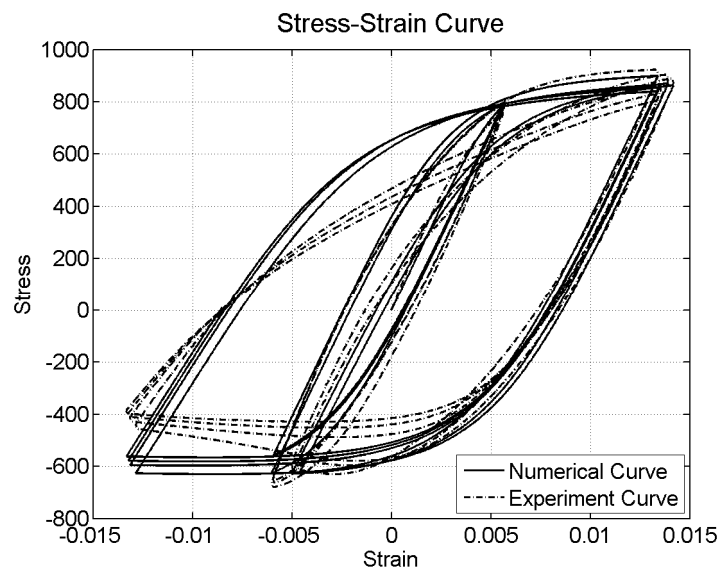


(a) in presence of buckling-XA1



**Figure 5.12 Comparison of numerical curves and experimental curves
($L/D=5$)**





(c) in presence of buckling-XC3

**Figure 5.13 Comparison of numerical curves and experimental curves
($L/D=11$)**

6. APPLICATION IN REINFORCED CONCRETE COLUMN

The application of the steel material “Steel05” is verified in simulating the cyclic behaviors of the reinforced concrete piers. In OpenSees, fiber model is built to simulate the concrete column.

6.1 APPLICATION OF FIBER MODEL IN CANTILEVER COLUMN ANALYSIS

The theory to build the fiber model for the reinforced concrete column is shown in Figure 6.1. The column could be divided into segments along its axial length, and each segment could be simulated by one element.

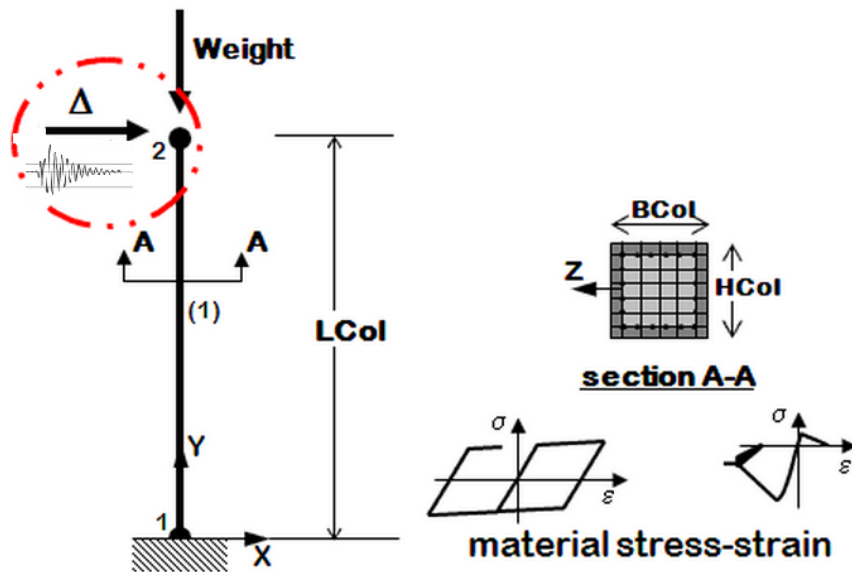


Figure 6.1 Fiber element technique used in reinforced concrete pier analysis under cyclic loading

The force-based element is adopted which allows plasticity to spread at any location along the element, and the accuracy could be improved by the number of integration point in the element without reducing the computational efficiency. Hereby the force-based element named as “nonlinearBeamColumn” in OpenSees is chosen to build the fiber model. As for the steel material model, “Steel05” is selected for the reinforcing bar, and “Concrete07” (Waugh, 2009) is used to simulate the cyclic behaviors of the unconfined concrete cover and confined concrete core.

6.2 PSEUDO-DYNAMIC TEST OF REINFORCED CONCRETE BRIDGE PIER

Two bridges (one regular and the other irregular) were designed by Attolico et al. (2000) according to the Italian Seismic Code (D.M.L.P.P.24.01.1986, 1986) and Eurocode8 Part 2 (EN1998, 2004) concerning the design of anti-seismic structures.

Then the most stressed pier in each bridge was picked and then the 1:6 scaled piers were casted in the laboratory to represent the corresponding piers (De Sortis, Nuti, & Petrangeli, 1998). The scaled pier specimens were pseudo-dynamically tested in the structural laboratory in Rome Tre University (Lavorato, 2009).

6.2.1 Regular Reinforced Concrete Bridge Pier

For the regular bridge shown in Figure 6.2, the most stressed pier is side pier with height equal to 14m. The dead axial load due to deck is 10800 kN. According to the scaled criteria, the dead axial load applied to the pier specimen equals 300 kN.

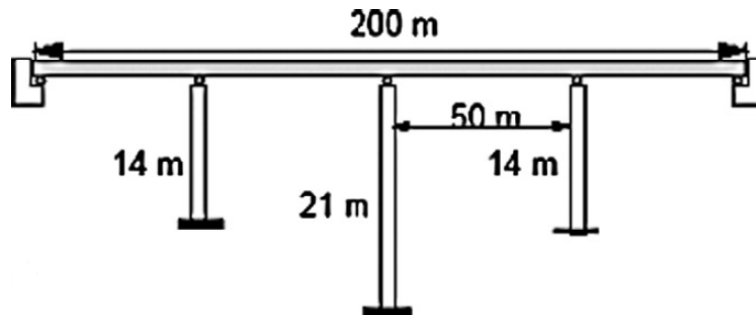


Figure 6.2 Regular bridge

As shown in Figure 6.3, the specimens numbered from 1 to 5 were made in the laboratory to represent the side pier in the regular pier. The number and deposition of the longitudinal rebars, the configuration of the stirrups and the design code are different for different specimen. The details are shown in Table 6.1.



Figure 6.3 Pier Specimen corresponding to the middle pier in the regular bridge

Table 6.1 Geometries and configuration of the piers

pier	design basis	Diameter (mm)	Height (mm)	Concrete cover (mm)	Longitudinal rebars	Spiral (mm)
1	DM	420	2340	30	24Ø10	Ø5/80
2	DM	420	2340	30	24Ø10	Ø5/100
3	DM	420	2340	30	24Ø10	Ø5/100
4	DM	420	2340	30	24Ø10	Ø5/80
5	EC8	420	2340	30	24Ø10	Ø6/40

Note: DM is short for the Italian seismic code D.M. LL.PP. 24.01.1986; EC8 stands for Eurocode8 Part 2 (1998-2).

Pseudo-dynamic tests of the pier specimens were made using the Italian Tolmezzo accelerogram (1976, E-W PGA=0.35g). Figure 6.4 demonstrates the damage state of one pier specimen after tested.

**Figure 6.4 Damage of the specimen at the end of the cyclic tests**

6.3 Comparison between the Numerical Analysis and Experimental Results

The mechanical characteristic of the materials used in the piers are shown as follows:

Concrete

- Ultimate strength $\sigma_{cu} = 25MPa$;
- Initial elastic modulus $E_c = 30000MPa$.

Steel

- Yield Stress $f_y = 500MPa$;
- Initial elastic modulus $E_s = 200000MPa$.

The real mechanical properties of the materials tested in the laboratory are shown in

Table 6.2.

Table 6.2 Mechanical properties of the materials tested in the laboratory

Material	concrete		steel			
Specimen	fcm	Φ	fsy	Fst	ε_{su}	Esh
	[MPa]	(mm)	[MPa]	[MPa]	[%]	[%]
1,2,3,4	17.21	5; 6*	445.46	680.4	16	1.4
		10	513.69	608.04	15.68	2.67
5	17.35	6	444.19	680.82	21.81	1.4
		10	537.61	618.01	16.7	4

6.3.1 Main Parameters in the Fiber Model

The material model “Concrete 07” is used to simulate the concrete, but the parameters for the confined core concrete and unconfined cover concrete are different. All the parameters for “Concrete07” used in the fiber model are listed in

Table 6.3.

Table 6.3 Parameters of “Concrete07” in the fiber model

concrete	Unconfined cover concrete	Confined core concrete
fc [MPa]	17.44	20.17
ec [-]	0.00178	0.00316
Ec[MPa]	24090	24090
ft [MPa]	2.6	2.6
et [-]	0.000215	0.000216
xp [-]	2	2
xn [-]	2.3	30
r [-]	1.4726	1.3605

The material model “Steel05” is used to simulate the behavior of the longitudinal rebar and the values of the input parameters for “Steel05” are listed in Table 6.4.

Table 6.4 Parameters of “Steel05” in the fiber model

Steel05	Fy [Mpa]	b	E0	L/D	r0	A6	P
		[-]	[MPa]	[-]	[-]	[-]	[-]
	574.37	0.0037	200000	10	5	1000	0.5

6.3.2 Experimental Test of the Bridge Piers

As shown in Figure 6.5, the cyclic lateral displacement, corresponding to the accelerogram of the 1976 Friuli earthquake recorded at Tolmezzo, is applied at the top of the pier specimens.

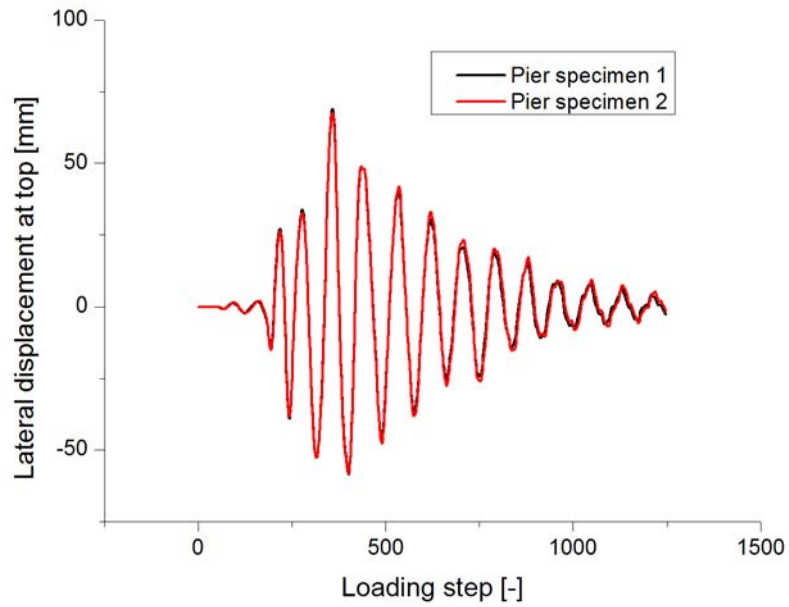


Figure 6.5 Lateral loading displacement histories at the top of the pier

The relationships between the shear forces measured at the bottom and the corresponding lateral displacements at the top of the pier 1 and 5 are illustrated in Figure 6.6 and Figure 6.7.

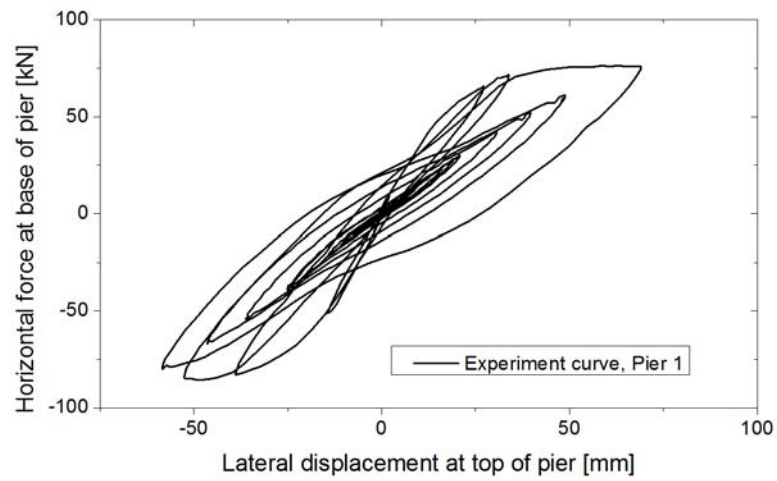


Figure 6.6 Experimental lateral force and displacement curve of pier 1

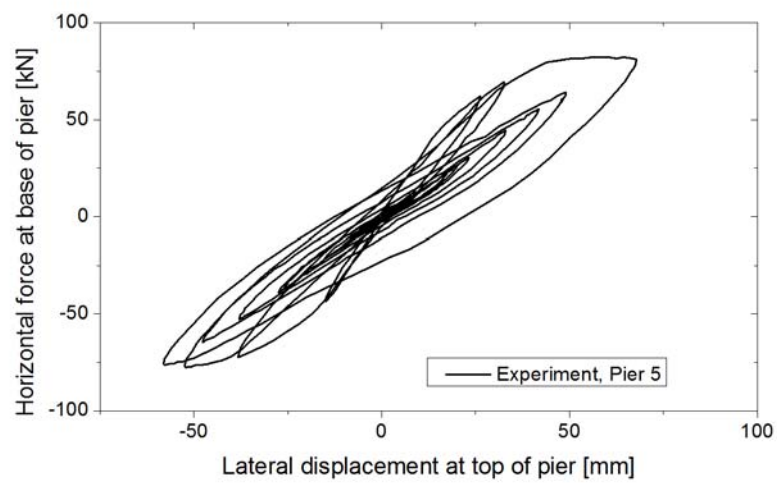


Figure 6.7 Experimental lateral force and displacement curve of pier 5

6.3.3 Comparisons Between Numerical Curves and Experimental Curves

The comparison between the numerical curves generated by the fiber model and the experimental curves of pier 1 is shown in Figure 6.8.

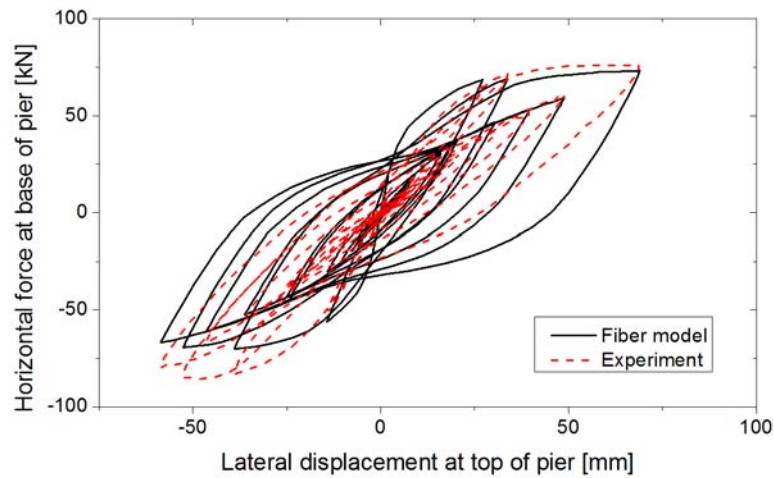


Figure 6.8 Comparison of force-displacement curve (horizontal force at the bottom and lateral displacement at the top of pier) between the fiber model and the experimental curves

The comparison between the numerical curve generated by the fiber model and the experimental curve of pier 5 is shown in Figure 6.9.

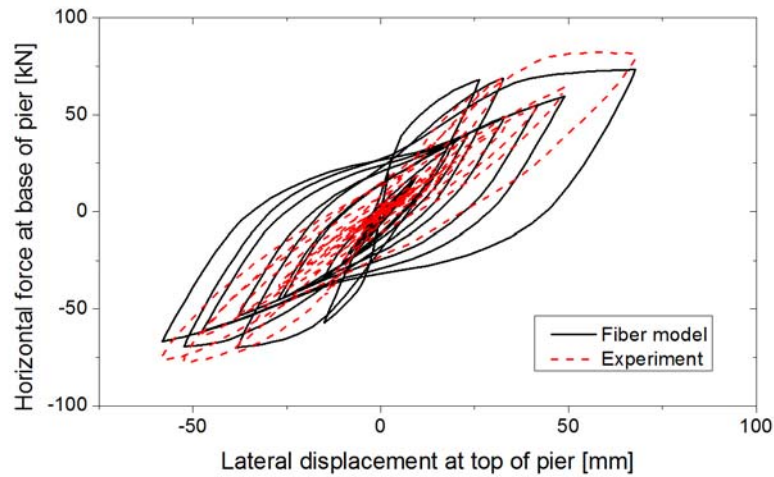
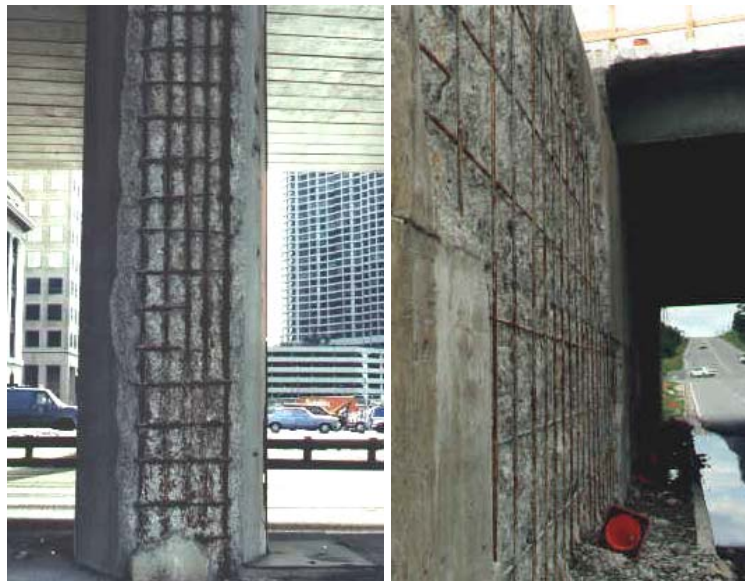


Figure 6.9 Comparison of force-displacement curve (horizontal force at the bottom and lateral displacement at the top of pier) between the fiber model and the experimental curve

From the above comparisons, the fiber could capture the main characteristics of the experimental curves, but the stiffness of the numerical curve is greater than the experimental curves. If the column is divided into two segments to consider the eccentricity and second order effect of the pier, better simulation results could be obtained.

7. EFFECT OF CORROSION ON MODEL FOR REBAR

Serious durability problem has been observed in the reinforced concrete structures such as bridge decks, parking garages, undersea tunnels, and other marine structures even less than 20 years old, when they are exposed to corrosive environments like deicing salts and seawater (Mehta & Burrows, 2001). The structures could fail to provide sufficient bearing capacity or plastic deformation performance before the designed service life, resulting from the corrosion of the rebar (as shown in Figure 7.1) in the reinforced concrete elements which is the leading cause of deterioration in concrete.



a)

b)



c)

Figure 7.1 Corrosion of rebar in the highway bridge: a) corrosion of the pier b) corrosion of the rebar and spalling of the cover concrete of the wall c) overview of the highway bridge (Tullmin, 2010)

In the following section, the mechanism of corrosion of rebar will be briefly introduced and the effect of the corrosion of rebar on the mechanical performance of the rebar will be studied.

7.1 MECHANISM OF CORROSION OF REBAR IN REINFORCED CONCRETE

As a result of the hydration reactions of cement, the pore solution of concrete tends to be alkaline, with pH values typically in the range 12.5-13.6. Under such alkaline conditions, reinforcing steel tends to passivate

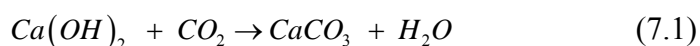
and display negligible corrosion rates. However, due to the porous nature of concrete, corrosive species and chemical species supporting corrosion reactions can enter the concrete and lead to corrosion problems (Associate, 1995).

Chloride ions and carbonation are two important inducements to promote rebar corrosion.

Primarily due to exposure of reinforced concrete to chloride ions, which could permeate through sound concrete pore or cracks into reinforced concrete, the premature corrosion of steel reinforcement occurs, if oxygen and moisture are available to sustain the electrochemical reaction.

Chloride-containing admixtures can also cause corrosion. The mechanism how chlorides promote corrosion is not completely understood. The widely accepted theory is that chloride ions get through the protective oxide film easier than other ions, leaving the steel vulnerable to corrosion. The initiation of corrosion primarily results from chlorides, but chlorides don't affect directly the rate of corrosion after initiation. Instead the availability of oxygen, the electrical resistivity and relative humidity of the concrete, and the pH and temperature are the primary rate-controlling factors.

When carbon dioxide in the air gets through the concrete and reacts with hydroxides such as calcium hydroxide, calcium carbonates is formed, which progress is called carbonation of concrete. The reaction is shown as follows in Eq. (7.1):



This reaction reduces the pH of the pore solution to as low as 8.5, resulting in the passive film on the steel not stable.

Another effect of carbonation of concrete is that the chloride ions threshold needed to promote corrosion becomes lower. When pH equals 12 to 13 in new concrete, the chlorides threshold to corrosion initiation of rebar is about 7000 to 8000 parts per million (ppm) of chlorides; while the chloride threshold for corrosion could reduce to 100 ppm or below if the pH is lowered to a range of 10 to 11(PortlandCementAssociation).

However, like chloride ions, carbonation destroys the passive film of the reinforcement to promote corrosion initiation, but does not influence the rate of corrosion.

When steel corrodes, the rust generated occupies greater volume than the steel. This expansion creates tensile stresses in the concrete, and eventually causes cracking, delamination, and spalling of concrete.

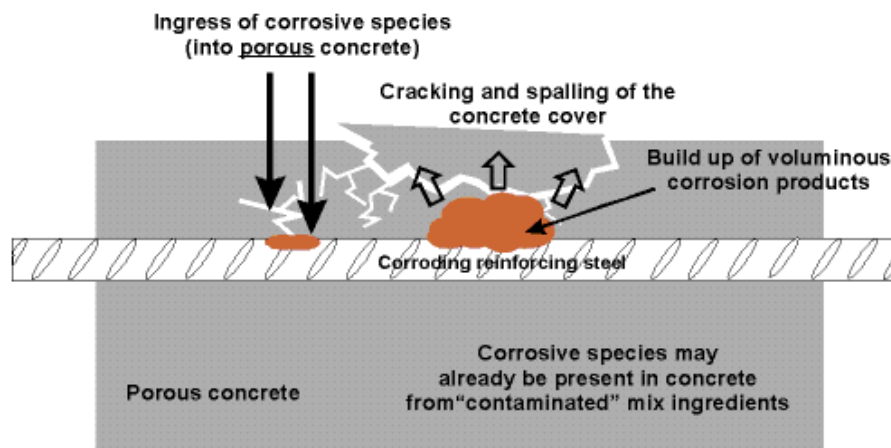


Figure 7.2 corrosion of rebar in concrete (Tullmin, 2010)

After the protective concrete cover is collapsed, the reinforcing steel is more vulnerable to further corrosion.

The corrosion of rebar in the reinforced concrete could be divided into four stages (Kumar Mehta, 2000):

Stage 1: At beginning, the concrete appears to be sound with relatively inevitable little macroscopic cracking due to shrinkage of concrete, illustrated in Figure 7.3.



Figure 7.3 Stage 1 of corrosion (Tullmin, 2010)

Stage 2: Obvious macroscopic cracks have appeared and the concrete surface is stained by reddish discoloration from corrosion product formation, shown in Figure 7.4.



Figure 7.4 Stage 2 of corrosion (Tullmin, 2010)

Stage 3: Voluminous of corrosion products are built up, causing the concrete cover over the reinforcing steel to spall, as illustrated in Figure 7.5.



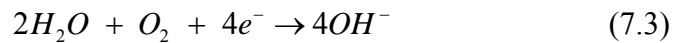
Figure 7.5 Stage 3 of corrosion (Tullmin, 2010)

Stage 4: With the development of the spalling of the concrete cover, the reinforcing steel bars directly exposed to the atmosphere, shown in Figure 7.6.



Figure 7.6 Stage 4 of corrosion (Tullmin, 2010)

Corrosion of rebar (Trethewey & Chamberlain, 1995) is an electrochemical process involving the flow of charges (electrons and ions). Two half-cell reactions occur in the process of corrosion: an oxidation reaction at the anode where iron atoms lose electrons and move into the surrounding concrete as ferrous ions, demonstrated in Eq. (7.2); and a reduction reaction at the cathode, where electrons combine with water and oxygen in the concrete, defined in Eq. (7.3).



To maintain electrical neutrality, the ferrous ions migrate through the concrete pore water to these cathodic sites and form iron hydroxides, or rust, expressed in Eq. (7.4):

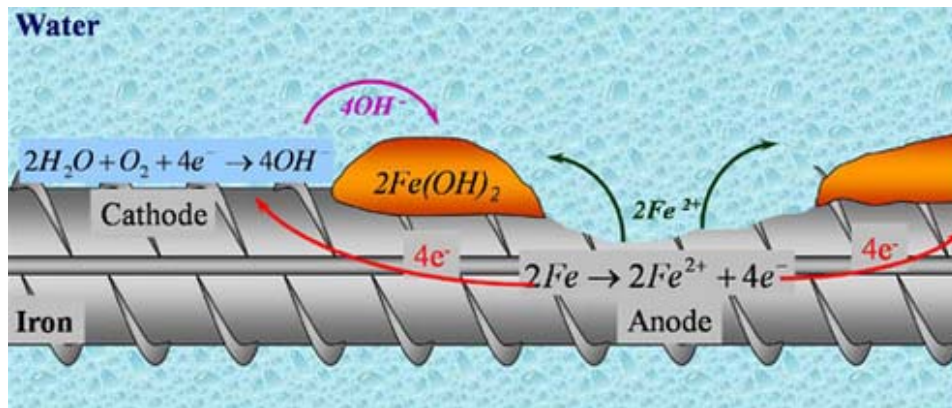
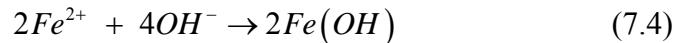


Figure 7.7 Electrochemical reaction of rebar in concrete

For corrosion of rebar to occur, four fundamental components are necessary in an electrochemical (Daily, 1999):

- An anode.
- A cathode.
- A conducting environment for ionic movement (electrolyte).
- An electrical connection between the anode and cathode for the flow of electron current.

If any of the above components is missing or disabled, the electrochemical corrosion process will be stopped. Thus different methods to prevent rebar corroding based on prevent or reduce the aforementioned electrochemical progress (Song & Shayan, 1998).

Most previous research topics related to corrosion of rebar are concentrated on mechanism of corrosion, methods to prevent corrosion of rebar and techniques to repair the corroded rebar in the concrete structures (Verma, Bhadauria, & Akhtar, 2014).

Next the effect of corrosion on the mechanical properties of rebar in the reinforced concrete will be introduced and studied.

For the reinforced concrete structures, in order to evaluate the seismic performance precisely, deterioration due to the corrosion of rebar should be considered properly. Following the effects of corrosion of rebar on the seismic behaviors of the reinforced concrete will be considered.

7.2 EFFECT OF CORROSION

The effects of corrosion on the residual tensile capacity and the mechanical properties like ductility of reinforcement have been researched recent years. It is found that the non-uniform cross section loss due to pitting corrosion along the bar has an important effect on the force-axial displacement in tensile tests.

Kashani et al. (2013b) adopted the accelerated techniques on bare bar to simulate corrosion process in the laboratory and used 3D optical measurement technique to analyze the patterns of the corroded rebars. Then a series of monotonic and cyclic test on rebar corroded rebars were carried out to study the effects of corrosion on the compressive strain-strain relationship and the cyclic behaviors including inelastic buckling respectively. The corrosion extended Dhakal-Maekawa buckling model was proposed by the authors to simulate the cyclic behavior of corroded rebar. The model could precisely simulate the cyclic behavior of corroded reinforcing bar including inelastic buckling when the slenderness ration $L/D < 8$.

In this section, the effects of corrosion on the yield stress, the critical slenderness and the computational length of the reinforcement are studied.

7.2.1 EFFECT OF CORROSION ON YIELD STRESS

According to the experimental investigation of the corroded rebars, the cross section of the rebar varies along the length of the rebar. The exact position of the pitting corrosion is impossible to be predicted in the real structure. However the corrosion rate of the rebar in existing structures could be detected by non-destructive monitoring system (M. M. Kashani, A. J. Crewe, & N. A. Alexander, 2013). Thus the mean cross section of the corroded rebar D' could be deduced according to the corrosion rate, and shown in Eq. (7.5).

$$D' = D\sqrt{1-\gamma_c} \quad (7.5)$$

Where D is the cross section diameter of the original uncorroded rebar, γ_c represents the corrosion rate and is defined in Eq. (7.6):

$$\gamma_c = \frac{m_0 - m}{m_0} \quad (7.6)$$

Where m_0 is the original mass of the rebar, m is the mass of corroded rebar.

It was found that the non-uniform area of cross section of the corroded rebar due to pitting corrosion has an important effect on the axial bearing capacity of the corroded rebar.

Du et al. (2005) proposed the empirical formula Eq. (7.7) based on extensive tensile force-extension experimental tests to calculate the regressed tensile yield stress of the corroded rebar.

$$f_{yt} = f_y (1 - a\psi) \quad (7.7)$$

Where f_{yt} is the notional yield stress in tension corresponding to the corroded rebar based on the original rebar cross section area, f_y is the yield stress of uncorroded rebar, a is the regression factor considering the effect of non-uniform distribution of pitting corrosion and equals 0.015 according to Du et al. The value of a , obtained by different researchers, ranges from 0.01 to 0.017. And ψ represents the mass loss due to corrosion, and is defined as: $\psi = 100\gamma_c$.

The mean stress and mean strain are adopted to represent the behavior of the reinforcement. The yield stress in tension f'_{yt} corresponding to the

corroded rebar based on the mean cross section area could be deduced as Eq. (7.8):

$$f_{yt}' = f_y (1 - a\psi) / (1 - \gamma_c) \quad (7.8)$$

It was found by Kashani et al. (2014) that the non-uniform pitting corrosion has an obvious effect on the buckling reduction of the rebar in compression. The empirical formula for notional yield stress in compression is given in Eq. (7.9):

$$f_{yc}' = f_y (1 - \beta_c \psi) \quad (7.9)$$

Where f_{yc}' is the notional yield stress in compression corresponding to the corroded rebar based on the mean cross section area, β_c is the regression factor that represents the effect of non-uniform pitting corrosion.

Then define $d_c' = f_{yt}' / f_y = (1 - a\psi) / (1 - \gamma_c)$ to represent the notional yield stress deterioration in tension due to corrosion, and define $d_c^c = f_{yc}' / f_y = (1 - \beta_c \psi)$ to represent the notional yield stress reduction in compression. a and β_c are the parameters in the formula for slenderness ratio and the values given by Kashani et al. (2013) are listed in Table 7.1.

Table 7.1 Parameters to calculate the notional yield stress deterioration

Slenderness ratio L/D	a	β_c
$L/D \leq 5$	0.017	0.005
$5 < L/D \leq 10$	0.017	0.0065
$L/D > 10$	0.017	0.0125

Then the relationships between the notional yield stress deterioration and mass loss rate of rebar with different slenderness are illustrated in Figure 7.8, Figure 7.9 and Figure 7.10.

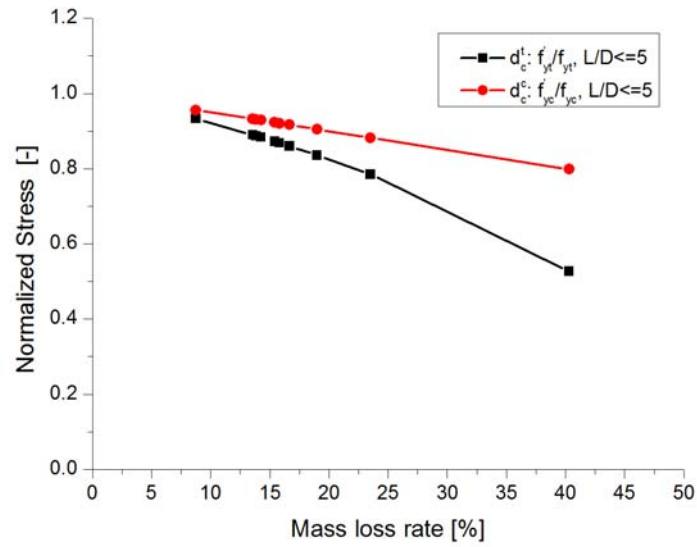


Figure 7.8 Notional yield stress deterioration in tension and compression ($L/D=5$)

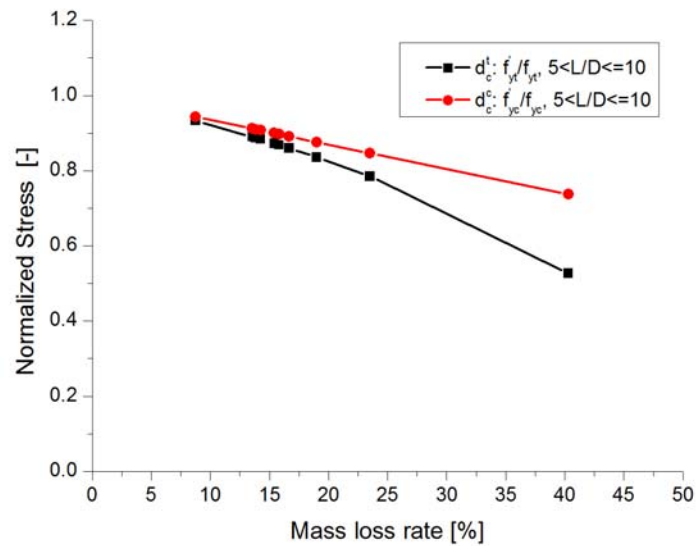


Figure 7.9 Notional yield stress deterioration in tension and compression ($5 < L/D \leq 10$)

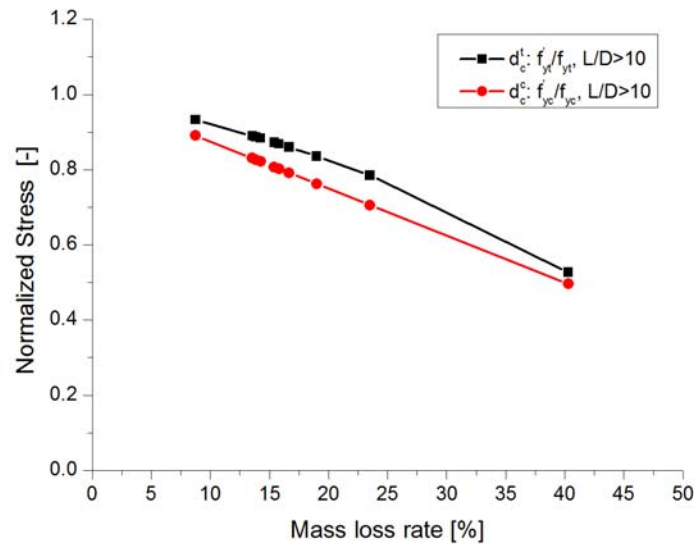


Figure 7.10 Notional yield stress deterioration in tension and compression ($L/D > 10$)

From the above figures, it could be found that the notional yield stress deterioration coefficient in tension is smaller than that in compression when slenderness ratio $L/D < 5$ and $5 \leq L/D < 10$. This means that the notional yield stress corresponding to the corroded rebar based on the mean cross section area in tension is smaller than that in compression, if the yield stresses of the original uncorroded rebar in tension and in compression are the same, which seems unreasonable.

Then the notional yield stress corresponding to the corroded rebar based on the mean cross section, named as mean yield stress, were obtained by Kashani et al. (2013a) in the laboratory. The relationship between the mean yield stress and the mass loss rate are illustrated in Figure 7.11, Figure 7.12 and Figure 7.13, with different slenderness, respectively.

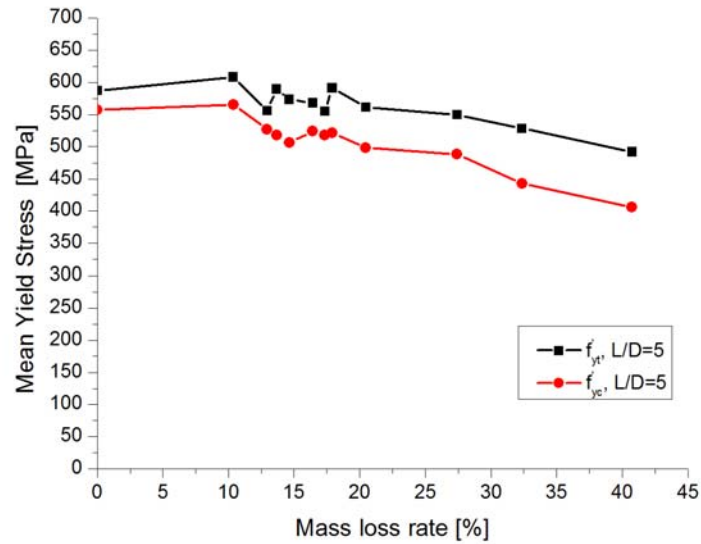


Figure 7.11 Relationship between mean yield stress and mass loss rate $L/D=5$, data from Kashni et al. (2013a)

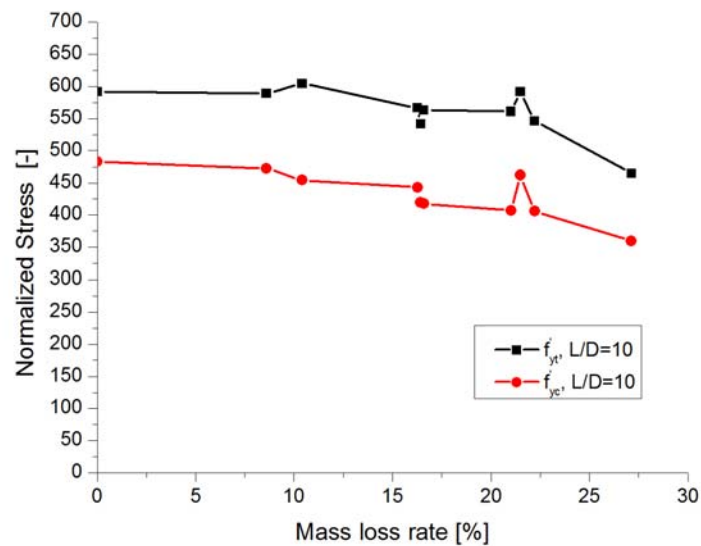
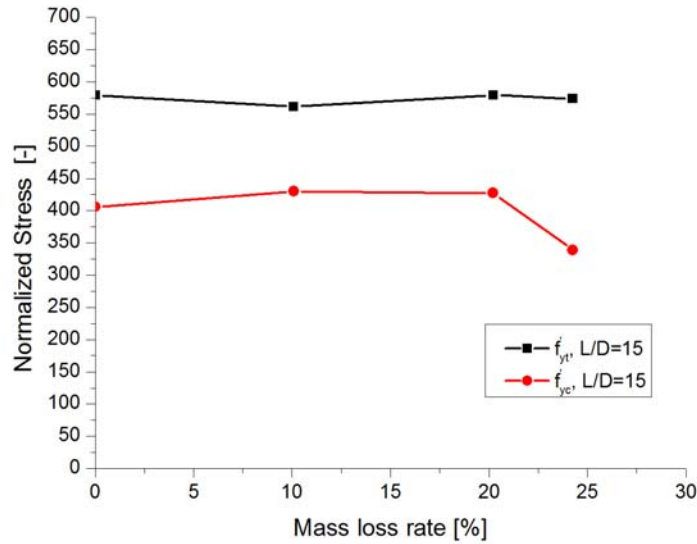


Figure 7.12 Relationship between mean yield stress and mass loss rate $L/D=10$, data from Kashni et al. (2013a)



**Figure 7.13 Relationship between mean yield stress and mass loss rate
L/D=15, data from Kashni et al. (2013a)**

From the above three figures, it is found that the reduced notional yield stress in tension is always larger than that in compression. This phenomenon makes sense because the non-uniform pitting corrosion could increase the effect of load eccentricity and the second order moment on the axial residual capacity in compression. As a result, it is necessary to propose new formula for notional yield stress corresponding to the corroded rebar based on the corroded cross section area.

7.2.2 Effect of Corrosion on Critical Slenderness

As mentioned in chapter 3, the critical slenderness λ_{cr} equals $5/\sqrt{\beta}$, and β equals $f_{yc}/450$. f_{yc} is the yield stress in compression and 450 represents the original yield stress of the carbon steel rebar Feb44 tested by Monti and Nuti (1992).

For the corroded rebar, the mean yield stress in compression $f'_{yc} = f_y(1 - \beta_c \psi)$, thus the critical slenderness λ'_{cr} is expressed in Eq. (7.10):

$$\lambda'_{cr} = 5\sqrt{450/f'_{yc}} = 5\sqrt{450/f_{yc}} \sqrt{f_{yc}/f'_{yc}} = \frac{\lambda_{cr}}{\sqrt{1 - \beta_c \psi}} \quad (7.10)$$

For corroded rebar, as $0 < 1 - \beta_c \psi < 1$, $\lambda'_{cr} > \lambda_{cr}$. The ratios between critical slenderness of corroded rebar and critical slenderness of original rebar with different slenderness are illustrated in Figure 7.14.

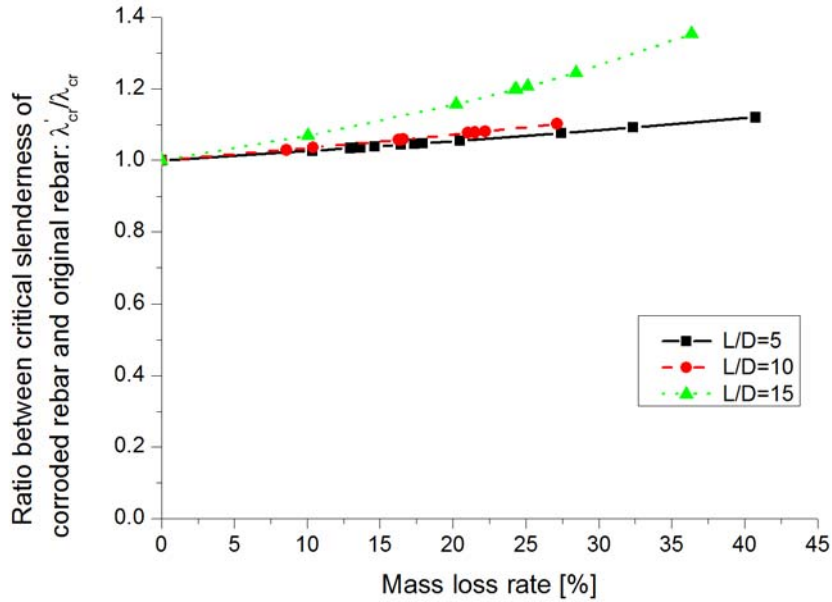


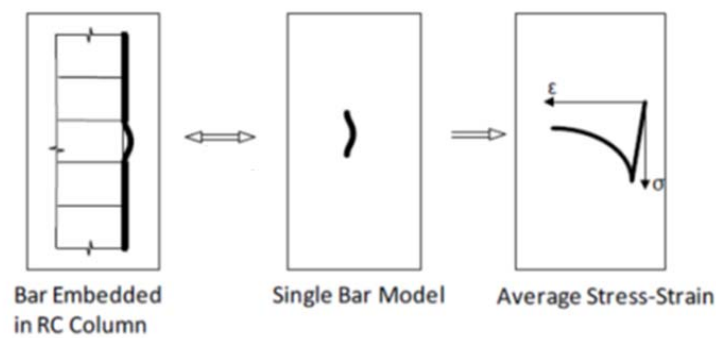
Figure 7.14 Ratio between the critical slenderness of corroded rebar and critical slenderness of original rebar $\lambda'_{cr}/\lambda_{cr}$

This means that the critical slenderness of the corroded rebar increases due to the notional yield stress deterioration. However, it doesn't mean that the rebar corrosion could postpone the occurrence of buckling of the reinforcement. On the contrary, the buckling should occur earlier because the mean diameter of the rebar D' is smaller than the original diameter of the original uncorroded rebar D . Furthermore, the computational length of

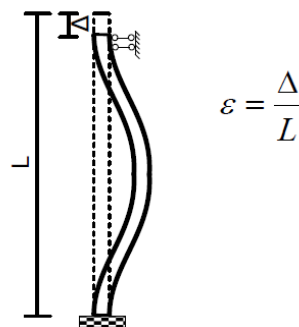
the reinforcing bar L' should increase, because the confinement from the stirrup deteriorates due to the corrosion in the contact point between the longitudinal rebar and the transversal loop. Thus the slenderness of the corroded rebar λ' could grow faster than the increase of the critical slenderness of the corroded rebar λ'_{cr} .

7.2.3 Effect of Corrosion on Computational Length of Rebar

Following the schema shown in Figure 7.15, uncorroded longitudinal rebars usually buckle between two consecutive stirrups, based on the assumption that stirrups constitute a strong rigid link for the longitudinal rebar.



a) buckling of rebar in RC column



b) computational model for rebar

Figure 7.15 Buckling of compressed bar between two consecutive stirrups

In case the transversal loops are not stiff enough, buckling of the longitudinal will buckle beyond the stirrup, as demonstrated in Figure 7.16.

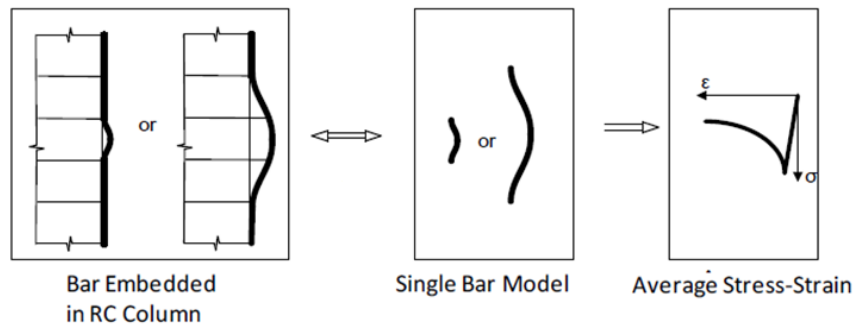


Figure 7.16 Buckling exceeds two consecutive stirrups

As the stiffness of the original uncorroded stirrup is sufficient, the second case can usually be disregarded. However, if corrosion occurs, both longitudinal rebar and stirrups are affected. The contact points between the longitudinal rebar and transversal rebar is vulnerable to corrosion. At the beginning of the corrosion, the product of corrosion remains near the contact points, therefore the link is unchanged and the confinement from the stirrups is sufficient. However, as corrosion continues, both stirrups and longitudinal bars reduce their diameter and the confinement is not sufficient. As a result, a short gap arises around the contact point between the stirrup and the longitudinal rebar. The buckling will occur beyond the two consecutive stirrups.

The computational length of the corroded rebar L' should be defined incorporating the aforementioned effect.

7.3 CORROSION EXTENDED MODEL FOR REBAR

As discussed above, the effect of corrosion on the yield stress, the critical slenderness and the slenderness ratio of the corroded rebar should be considered.

7.3.1 Notional Yield Stresses in Tension and Compression

As discussed in section 7.2.1, the corrosion could cause the notional yield stresses corresponding to corroded rebar based on the mean cross section area different in tension and compression to reduce. The phenomenon that the yield stresses are different in tension and compression is named as anisotropy in chapter 3.

The notional yield stresses corresponding to the corroded rebar based on the mean cross section area are called mean yield stress and are defined in Eq. (7.11) and Eq. (7.12) respectively.

$$f'_{yt} = f_y (1 - \beta_c^t \psi) \quad (7.11)$$

$$f'_{yc} = f_y (1 - \beta_c^c \psi) \quad (7.12)$$

Where f'_{yt} and f'_{yc} are the mean yield stress in tension and in compression respectively, f_y is the yield stress of the original uncorroded rebar, β_c^t and β_c^c are the corrosion deterioration factor incorporating the effect of non-uniform pitting corrosion, ψ represents the mass loss.

Hereby, the anisotropy coefficient α defined in section 3.2 could be expressed in Eq. (7.13):

$$\alpha = \frac{f'_{yt}}{f'_{yc}} = \frac{1 - \beta_c^t \psi}{1 - \beta_c^c \psi} \quad (7.13)$$

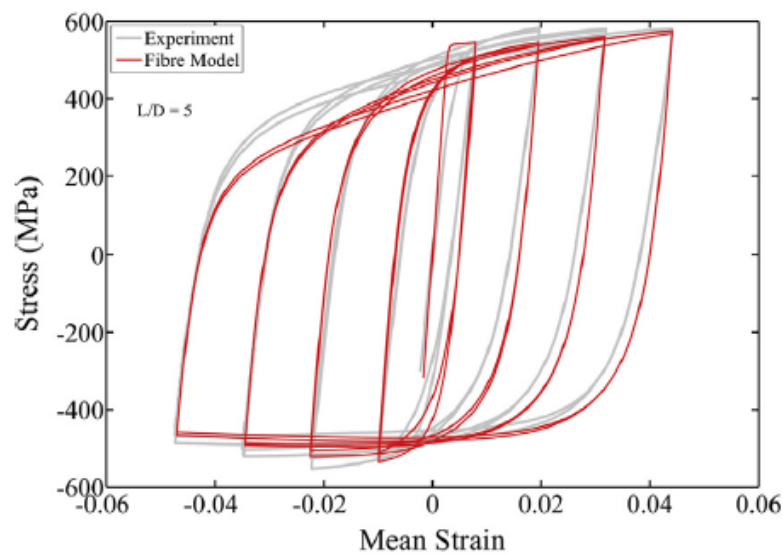
The critical slenderness coefficient β , defined in Eq. 3.1 could be expressed in Eq. (7.14):

$$\beta = \frac{f'_{yc}}{f_Y} = \frac{f_y (1 - \beta_c^c \psi)}{f_Y} \quad (7.14)$$

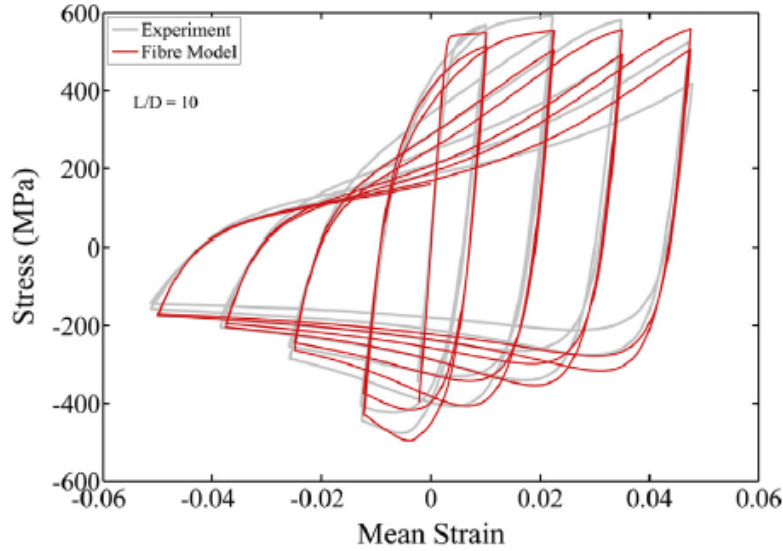
Where f_Y is the constant represent the yield stress of carbon steel Feb44k, and equals 450 MPa.

7.3.2 Slenderness Ratio of Corroded Rebar

Dhakal and Maekawa (2002c) proposed that the buckling length of the longitudinal rebar could be times of the stirrup spacing if the confinement from the transversal rebar is not sufficient and provided the iterative procedure to calculate the buckling length. According to their methods, the computational length of the longitudinal rebar should be at least two times of the stirrup spacing after corrosion generates the gap at the contact point between longitudinal rebar and stirrup and reduce the confinement towards the longitudinal rebar, if the original buckling length equals the stirrup spacing. However this doesn't conform with the experimental result on the bare corroded rebar made by Kashani et al. (2014), as shown in Figure 7.17. From the comparison between Figure 7.17 a) and Figure 7.17 b), it could be found that the stress-strain curves of corroded rebar with $L/D=5$ and $L/D=10$ are quite different. Thus other method should be proposed to predict the computational length of the corroded rebar.



a) $L/D=5$



b) L/D=10

Figure 7.17 Stress-strain relationship of corroded rebar with different slenderness

There are two proposals to calculate the computational length.

For the first proposal, assume that the computational length increment is the function of the gap generated at the contact point between the stirrup and the longitudinal rebar. Considering that the gap could be the sum of radius reduction in stirrup and radius reduction in longitudinal rebar, the gap could be expressed in Eq. (7.15):

$$g = \left[(D - D') + (D_s - D'_s) \right] / 2 = \left[D(1 - \sqrt{1 - \gamma_c}) + D_s(1 - \sqrt{1 - \gamma_c}) \right] / 2 \quad (7.15)$$

Where g is the gap at the contact point, D and D' are diameter of original uncorroded longitudinal rebar and corroded rebar, D_s and D'_s are the diameter of the uncorroded stirrup and corroded stirrup, γ_c is the mass loss rate due to corrosion.

Assuming that the longitudinal rebar and the stirrup at the contact point have the same mass loss rate γ_c , substitute D to D_s to simplify the expression but guarantee the effectiveness of the evaluation, the simplified formula is given in Eq. (7.16):

$$g = [2(D - D')]/2 = D(1 - \sqrt{1 - \gamma_c}) \quad (7.16)$$

Assume that at each contact point the gap could exceed the computational length times of g , define as μg , thus the total computational length L' of the corroded rebar is given in Eq. (7.17):

$$L' = L + 2\mu g = L + 2\mu D(1 - \sqrt{1 - \gamma_c}) \quad (7.17)$$

Thus the computational slenderness of the corroded rebar λ' could be determined, and the relationships between the ratio λ' to the original slenderness of the rebar λ and the mass loss rate are illustrated in Figure 7.14.

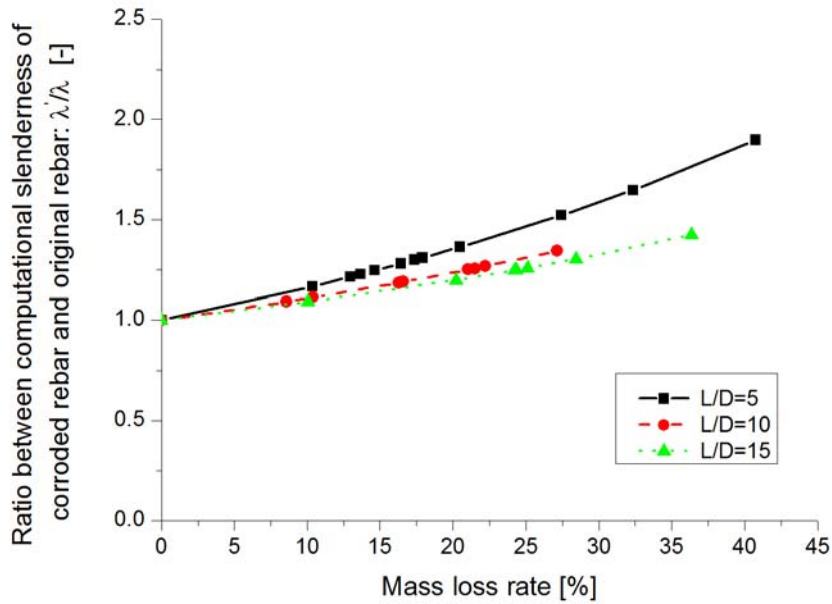


Figure 7.18 Relationship between λ'/λ (ratio computational slenderness of corroded rebar and original rebar) and mass loss rate

Another method is based on the ratio between the slenderness and the critical slenderness of the corroded rebar equal to that of uncorroded rebar. Define the slenderness of the corroded rebar based on the cross section of the original uncorroded rebar λ'' in Eq. (7.18):

$$\lambda'' = \frac{L'}{D} \quad (7.18)$$

Where L' is the computational length of the corroded rebar. The corresponding critical slenderness of the corroded rebar based on the original cross section could be calculated by Eq. (7.19):

$$\lambda_{cr}'' = 5\sqrt{450/f_{yc}} \quad (7.19)$$

Where f_{yc} is the notional yield stress in compression corresponding to the corroded rebar based on the original cross section area, and is defined in Eq. (7.20).

$$f_{yc} = f_y (1 - c\psi) \quad (7.20)$$

In which f_y is the yield stress of original uncorroded rebar, c is the deterioration coefficient incorporating the effect of non-uniform pitting corrosion. The value of c , given by Kashani et al. (2013), depends on the slenderness and is listed in Table 7.2.

Table 7.2 Values of c to calculate the notional stress

Slenderness L/D	c
8-10	0.016
15-20	0.020

Assume that the ratio between the slenderness and the critical slenderness of the original uncorroded rebar and the corroded rebar based on the original rebar is equal, shown in Eq. (7.21).

$$\frac{\lambda''}{\lambda_{cr}''} = \frac{\lambda}{\lambda_{cr}} \quad (7.21)$$

Thus the relationship between L' and L could be defined in Eq. (7.22):

$$L' = L \sqrt{\frac{f_y}{f_{yc}}} = \frac{L}{\sqrt{1 - c\psi}} \quad (7.22)$$

For the corroded rebar with slenderness $L/D=5$, if the mass loss rate $\gamma=0.1$, the computational length L' could be calculated by the above two methods respectively.

Without experimental data, assume that μ equals 5, which means the length increase at each contact point is five times of the gap, in Eq. (7.23), the slenderness is given as:

$$\frac{L'}{D'} = \frac{L + 10D(1 - \sqrt{1 - \gamma_c})}{D\sqrt{1 - \gamma_c}} = 5.81 \quad (7.23)$$

Adopting the second method, the slenderness could be calculated in Eq. (7.24):

$$\frac{L'}{D'} = \frac{L\sqrt{f_y/f_{yc}}}{D\sqrt{1 - \gamma_c}} = \frac{L/\sqrt{1 - c\psi}}{D\sqrt{1 - \gamma_c}} = 5.55 \quad (7.24)$$

8. CONCLUSIONS AND FURTHER WORKS

The cyclic behaviors of the reinforcing bar in the existing reinforced concrete structures are fully studied, and the effects of yield stress on the critical slenderness and the anisotropy of some stainless steel reinforcing bar have been incorporated in the improved Monti-Nuti model proposed to simulate the cyclic behaviors of the reinforcement including buckling. The parameters in the model are identified by Genetic Algorithm and empirical formula is proposed to calculate the values of the parameters in more efficient but still robust way. The criteria to update the model parameters for each half branch at the reversal are proposed. Then the modified model is implemented in OpenSees. The material model is validated with the experimental curves. The material is adopted to do cyclic pushover analysis of piers and the effectiveness of the material could be confirmed from comparisons with the experimental curves.

Then effects of corrosion, which is inevitable in the aged reinforced concrete structures, on the monotonic and cyclic behaviors of the reinforcement are studied and corrosion extended model has been proposed for cyclic behaviors of corroded rebar. Further works about this issue are discussed at the end.

8.1 CONCLUSIONS

The cyclic behaviors of the reinforcing bar depend on both the slenderness of the reinforcement and the yield stress of the reinforcement. The cyclic stress-strain curves of the rebar could be identical if the combined parameters $L/D\sqrt{f_y}$ of different reinforcing bars are equal, even though the slenderness L/D and yield stress f_y of different rebars are different. Based on the experimental observation from Monti and Nuti (Giorgio Monti & Nuti, 1992), the critical slenderness, which determines when the rebar could buckle in compression, is 5 for the carbon steel rebar Feb44k with yield stress 450 MPa. Hereby for the rebar with yield stress equal to f_y in compression, the critical slenderness is modified

as $5\sqrt{450/f_y}$, which means that the larger the yield stress, the earlier buckling will emerge in compressive branch.

Due to better corrosion resistive performance, the stainless steel reinforcement has been applied to build the reinforced concrete structures in corrosive environment or repair the corrosion damaged reinforced structures. The anisotropic phenomenon of the stainless steel rebar which is produced according to the old Italian code before 2008, have been observed in the monotonic experiment tests (Albanesi et al., 2006). The critical slenderness of the anisotropic stainless steel reinforcing bar depends on the slenderness and the yield stress in compression. The original Monti-Nuti model has been improved to consider the effects of different yield stresses in tension and in compression.

In the modified Monti-Nuti model, calibration of the parameters is necessary to obtain accurate simulation of the experimental results. The parameters in the modified model determine in common the stress-strain relationship of the following half branch at each reversal. The Genetic Algorithm Method is effective to identify the proper values of the parameters. The objective of the fitness function is set to minimize the different between the numerical curve and experimental curve at each step of the cyclic loading. The designed framework could calculate the objective function for total difference between the experimental curves and numerical curves of the rebar under different loading cases. Through the Genetic Algorithm, the optimized values are obtained and the empirical formulae are proposed based on the optimized results. Adopting the empirical formulae, it could be easier to determine the parameter values which are determined by experimental test in the original model. The robustness and effectiveness of the formulae are validated by comparing with the experimental data.

When the reinforcing bar is subjected to generalized action, the parameters of the model for each half branch should not be fully updated at the partial unloading or reloading branch reversal. The strategies to update the parameters depend on the status of the previous half branch before the reversal. There are twelve possible conditions of the unloading or reloading half branch before the reversal, and they could be divided into three categories: plastic, elastic and small, and the corresponding judge criteria are proposed. For plastic half branch, the model parameters for the new half branch should be fully updated; for the elastic half branch, only partial parameters in the model for the new half branch need to be

updated; and for the small half branch, all the parameters in the model for the new half branch should be retrieved from the previous unloading or reloading branch in the same direction.

The modified Monti-Nuti steel material model is named “Steel05” and the implementation of this material model in OpenSees has been completed. Then the steel material model is applied in cyclic pushover analysis of piers. Comparisons between the numerical results and the experimental curve of the piers confirm the effectiveness of the material model.

Finally, the corrosion effects of the reinforcing bar, which is inevitable for the aged reinforced concrete structures, are studied base on the experiments on bare corroded rebar. After corrosion, the diameter of the corroded rebar decreases and varies along the length. Even though the non-uniform pitting corrosion has an effect on the monotonic and cyclic behaviors of the rebar, the mean cross section could be used to represent the corroded rebar. The mean yield stress reduces and the critical slenderness could increase according to the previous studies. However, the computational length of the corroded rebar also increases, as gap emerges at the contact point between the longitudinal rebar and transverse loop after the corrosion occurs and thus the confinement from the stirrup is not sufficient. The slenderness of the corroded rebar increase faster than the critical slenderness, thus the buckling will emerge earlier than the original uncorroded rebar. Furthermore, it is observed that the mean yield stresses, corresponding to the corroded rebar based on the mean cross section area, are different in tension and in compression. The anisotropy phenomenon of the corroded rebar should also be considered in the model for cyclic behavior. Finally the corrosion extended Monti-Nuti model is proposed based on aforementioned studies.

8.2 FURTHER WORKS

The modified Monti-Nuti could simulate accurately the cyclic behaviors of reinforcement both in absence of buckling and in presence of buckling when the minimum strain in compression is not smaller than -0.01. If the threshold value is exceeded, the disagreement between the experimental curve and the numerical curve will be obvious. Even though the strain of the reinforcement in the real reinforced concrete could not exceed -0.01 due to the confinement of the concrete, more study could be made on this issue to eliminate this disadvantage of the proposed model.

Corrosion has a significant effect on the seismic behaviors of aged reinforced concrete. In order to consider properly the effects of corrosion, the computational length of the corroded reinforcing bar should be studied. The relationship between the computational length and the gap, which emerged at the contact point between the longitudinal rebar and the stirrup, should be studied based on more experimental observation or investigation of real aged concrete structures. The effect the deterioration of confinement from the traverse loop on the computational length should also be studied. Furthermore, the effects of corrosion on the seismic performance should be studied through numerical analysis and experimental tests.

ACKNOWLEDGEMENTS

This research is partially funded by the CSC (China Scholarship Council) and by Italian Civil Protection Department RELUIS Project 2009-2012 AT-1 TASK1.1.2. The author thanks Acciaierie Valbruna who provided stainless steel reinforcement for the present study.

REFERENCES

- Aktan, A., Karlsson, B., & Sozen, M. A. (1973). *Stress-strain relationships of reinforcing bars subjected to large strain reversals*: University of Illinois Engineering Experiment Station. College of Engineering. University of Illinois at Urbana-Champaign.
- Aktan, A. E., & Ersoy, U. (1980). *Analytical Study of R/C Material Hysteresis*. Paper presented at the AICAP-CEB Symposium on Structural Concrete Under Seismic Actions, Rome.
- Albanesi, T., Lavorato, D., & Nuti, C. (2006). Prove sperimentali monotone e cicliche su barre di acciaio inox. *Sperimentazione su materiali e strutture, Convegno nazionale*, 357-366.
- Associate, N. R. M. C. (1995). Corrosion of steel in concrete.
- Attolico, A., Biondi, S., Nuti, C., & Petrangeli, M. (2000). *Influence of Buckling of Longitudinal Rebars in Finite Element Modelling of Reinforced Concrete Structures Subjected to Cyclic Loading*. Paper presented at the Proc. of Workshop on "Seismic Protection of Existing and New Construction Buildings by means of Unconventional Systems, Prin.
- Bae, S., Miseses, A., & Bayrak, O. (2005). Inelastic Buckling of Reinforcing Bars. *Journal of Structural Engineering*, 131(2), 314-321.
- Chang, G. A., & Mander, J. B. (1994). Seismic energy based fatigue damage analysis of bridge columns: part 1-evaluation of seismic capacity.
- Daily, S. F. (1999). *Understanding corrosion and cathodic protection of reinforced concrete structures*: Corpro Companies, Incorporated.

-
- De Sortis, A., Nuti, C., & Petrangeli, M. (1998). *Seismic response by pseudodynamic tests of RC bridges designed to Eurocode 8 and Italian seismic code*. Paper presented at the 11th European Conference on Earthquake Engineering.
- Dhakal, R. P., & Maekawa, K. (2002a). Modeling for postyield buckling of reinforcement. *Journal of Structural Engineering*, 128(9), 1139-1147.
- Dhakal, R. P., & Maekawa, K. (2002b). Path-dependent cyclic stress-strain relationship of reinforcing bar including buckling. *Engineering Structures*, 24(11), 1383-1396.
- Dhakal, R. P., & Maekawa, K. (2002c). Reinforcement Stability and Fracture of Cover Concrete in Reinforced Concrete Members. *Journal of Structural Engineering*, 128(10), 1253-1262.
- DM14.01.08. (2008). Italian Seismic Code: Ministero dei Lavori Pubblici
- DMLL.PP.24.01.1986. (1986). Italian National Seismic Code: Ministry of Infrastructures.
- Dodd, L., & Restrepo-Posada, J. (1995). Model for Predicting Cyclic Behavior of Reinforcing Steel. *Journal of Structural Engineering*, 121(3), 433-445.
- Du, Y., Clark, L., & Chan, A. (2005). Residual capacity of corroded reinforcing bars. *Magazine of Concrete Research*, 57(3), 135-147.
- EN1998. (2004). Design of structures for earthquake resistance, *Part 2: Bridges*: CEN.
- Filippou, F. C., Popov, E. P., & Bertero, V. V. (1983). Effects of bond deterioration on hysteretic behavior of reinforced concrete joints.
- Fragiadakis, M., Pinho, R., & Antoniou, S. (2007). *Modelling inelastic buckling of reinforcing bars under earthquake loading*. Paper presented at the Computational Structural Dynamics and Earthquake Engineering.

- Gardner, L., & Nethercot, D. (2004). Experiments on stainless steel hollow sections—Part 1: Material and cross-sectional behaviour. *Journal of Constructional Steel Research*, 60(9), 1291-1318.
- Giuffrè, A., & Pinto, P. (1970). Il comportamento del cemento armato per sollecitazioni cicliche di forte intensità. *Giornale del Genio Civile*, 5(1), 391-408.
- Gomes, A., & Appleton, J. (1997). Nonlinear cyclic stress-strain relationship of reinforcing bars including buckling. [Article]. *Engineering Structures*, 19(10), 822-826.
- Hill, H. (1944). *Determination of Stress-Strain Relations from "Offset" Yield Strength Values*: DTIC Document.
- Kashani, M. M., Crewe, A. J., & Alexander, N. A. (2013a). Nonlinear cyclic response of corrosion-damaged reinforcing bars with the effect of buckling. *Construction and Building Materials*, 41(0), 388-400.
- Kashani, M. M., Crewe, A. J., & Alexander, N. A. (2013). Nonlinear stress-strain behaviour of corrosion-damaged reinforcing bars including inelastic buckling. [Article]. *Engineering Structures*, 48, 417-429.
- Kashani, M. M., Crewe, A. J., & Alexander, N. A. (2013b). Use of a 3D optical measurement technique for stochastic corrosion pattern analysis of reinforcing bars subjected to accelerated corrosion. *Corrosion Science*, 73(0), 208-221.
- Kashani, M. M., Lowes, L. N., Crewe, A. J., & Alexander, N. A. (2014). Finite element investigation of the influence of corrosion pattern on inelastic buckling and cyclic response of corroded reinforcing bars. *Engineering Structures*, 75, 113-125.
- Knudsen, A., Jensen, F., Klinghoffer, O., & Skovsgaard, T. (1998). *Cost-effective enhancement of durability of concrete structures by intelligent use of stainless steel reinforcement*. Paper presented at the Conference on Corrosion and rehabilitation of reinforced concrete structures, Florida.

-
- Kumar Mehta, P. (2000). *Durability-critical issues for the future*. Paper presented at the CANMET/ACI. Séminaire international.
- Kunnath, S., Heo, Y., & Mohle, J. (2009). Nonlinear Uniaxial Material Model for Reinforcing Steel Bars. *Journal of Structural Engineering*, 135(4), 335-343.
- Lavorato, D. (2009). *Pseudo-dynamic tests on reinforced concrete bridge piers repaired and/or retrofitted by means of techniques based on innovative materials*. Roma Tre University, Rome.
- Ma, S. Y. M., Bertero, V., & Popov, E. P. (1976). Experimental and analytical studies on the hysteretic behavior of reinforced concrete rectangular and T-beams.
- Marano, G. C., Greco, R., & Sgobba, S. (2010). A comparison between different robust optimum design approaches: application to tuned mass dampers. *Probabilistic Engineering Mechanics*, 25(1), 108-118.
- Marano, G. C., Quaranta, G., & Monti, G. (2011). Modified genetic algorithm for the dynamic identification of structural systems using incomplete measurements. *Computer - Aided Civil and Infrastructure Engineering*, 26(2), 92-110.
- Mau, S., & El - Mabsout, M. (1989). Inelastic Buckling of Reinforcing Bars. *Journal of Engineering Mechanics*, 115(1), 1-17.
- Mckenna, F. T. (1997). *Object-oriented finite element programming: frameworks for analysis, algorithms and parallel computing*. University of California.
- Mehta, P. K., & Burrows, R. W. (2001). Building durable structures in the 21st century. *Concrete International*, 23(3), 57-63.
- MENEGOTTO, M. (1973). *Method of analysis for cyclically loaded RC plane frames including changes in geometry and non-elastic behavior of elements under combined normal force and bending*. Paper presented at the Proc. of IABSE Symposium on Resistance

and Ultimate Deformability of Structures Acted on by Well Defined Repeated Loads.

Monti, G., & Nuti, C. (1989). Modellazione del comportamento ciclico di barre in acciaio per armature di elementi in cemento armato: Department of Structural Engineering Rome,, Italy.

Monti, G., & Nuti, C. (1990). *Numerical model for steel bars under cyclic loading including post-elastic buckling*. Paper presented at the The 9th European Conference on Earthquake Engineering, Moscow.

Monti, G., & Nuti, C. (1992). Nonlinear cyclic behavior of reinforcing bars including buckling. *Journal of Structural Engineering*, 118(12), 3268-3284.

Mullapudi, T. R. S. (2010). *Seismic analysis of reinforced concrete structures subjected to combined axial, flexure, shear and torsional loads* (Vol. 72).

OpenSees. OpenSees. from <http://opensees.berkeley.edu>

PortlandCementAssociation. Corrosion of Embedded Metals. <http://www.cement.org/for-concrete-books-learning/concrete-technology/durability/corrosion-of-embedded-materials>

Quach, W., Teng, J., & Chung, K. (2008). Three-stage full-range stress-strain model for stainless steels. *Journal of Structural Engineering*, 134(9), 1518-1527.

Quaranta, G., Monti, G., & Marano, G. C. (2010). Parameters identification of Van der Pol–Duffing oscillators via particle swarm optimization and differential evolution. *Mechanical Systems and Signal Processing*, 24(7), 2076-2095.

Quimby, T. B. (2008). A Beginner's Guide to the Steel Construction Manual. *University of Alaska Anchorage // August*.

Ramberg, W., & Osgood, W. R. (1943). Description of stress-strain curves by three parameters.

-
- Rasmussen, K. J. R. (2003). Full-range stress–strain curves for stainless steel alloys. *Journal of Constructional Steel Research*, 59(1), 47-61.
- Scott, M. H. (2011). Numerical Integration Options for the Force-Based Beam-Column Element in OpenSees.
- Song, G., & Shayan, A. (1998). *Corrosion of steel in concrete: causes, detection and prediction: a state-of-the-art review*.
- Stanton, J. F., & McNiven, H. D. (1979). *The development of a mathematical model to predict the flexural response of reinforced concrete beams to cyclic loads, using system identification*.
- Thompson, K., & Park, R. (1978). Stress-strain model for grade 275 reinforcing steel with cyclic loading. *Bull. New Zealand Nat. Soc. for Earthquake Engrg., Waikanae, New Zealand*, 11(2), 101.
- Trethewey, K. R., & Chamberlain, J. (1995). Corrosion for science and engineering.
- Tullmin, M. (2010). Corrosion monitoring focused site. from <http://www.corrosion-club.com/>
- Uriz, P. (2008). *Toward earthquake-resistant design of concentrically braced steel-frame structures*: Pacific Earthquake Engineering Research Center.
- Uriz, P., Filippou, F., & Mahin, S. (2008). Model for Cyclic Inelastic Buckling of Steel Braces. *Journal of Structural Engineering*, 134(4), 619-628.
- Verma, S. K., Bhadauria, S. S., & Akhtar, S. (2014). Monitoring corrosion of steel bars in reinforced concrete structures. *The scientific world journal*, 2014.
- Waugh, J. D. P. (2009). *Nonlinear analysis of T-shaped concrete walls subjected to multi-directional displacements*.

- Zhou, Z., Nuti, C., & Lavorato, D. (2014). *Modeling of the mechanical behavior of stainlessreinforcing steel*. Paper presented at the 10th fib International PhD Symposium in Civil Engineering.
- Zhou, Z., Nuti, C., & Lavorato, D. (2015a). *A model for carbon and stainless steel Reinforcing Bars Including Inelastic Buckling for evaluation of capacity of existing structures*. Paper presented at the 5th International Conference on Computational Methods in Structural Dynamics and Earthquake Engineering.
- Zhou, Z., Nuti, C., & Lavorato, D. (2015b). *Modified Monti-Nuti model for different types of reinforcing bars including inelastic buckling*. Paper presented at the The 2nd International Symposium on Advances in Civil and infrastructure Engineering.
- Zong, Z. (2010). *Uniaxial material model incorporating buckling for reinforcing bars in concrete structures subjected to seismic loads* (Vol. 71).